

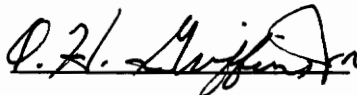
MODELING OF TEXTILE BASED COMPOSITE MATERIALS

by

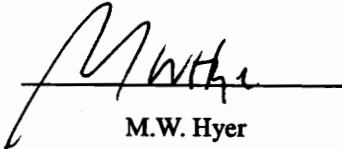
Edward H. Glaessgen

Dissertation submitted to the Faculty of the
Virginia Polytechnic Institute and State University
in partial fulfillment of the requirements for the degree of
DOCTOR OF PHILOSOPHY
in
Engineering Mechanics

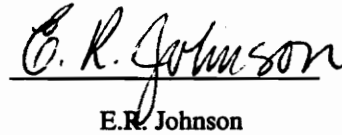
APPROVED:



O.H. Griffin, Jr., Chairman



M.W. Hyer



E.R. Johnson



D.H. Morris



S.A. Ragab

June, 1996

Blacksburg, Virginia

Key Words: Composite Material, Textiles, Failure, Finite Element Analysis

c. 2

LD
5655
V856
1996
G584
c. 2

MODELING OF TEXTILE BASED COMPOSITE MATERIALS

by

Edward H. Glaessgen

Dr. O.H. Griffin, Jr., Chairman

Engineering Mechanics

(ABSTRACT)

A finite element based model for interrogation of the elastic and progressive failure response of textile based composite materials has been developed and implemented. The geometrically thorough textile geometry model is used as the basis for creation of the geometry used for the finite element analysis. A detailed assessment is made for the linear elastic response of a plain weave textile composite subjected to various boundary conditions and loadings. Hashin's failure criterion and a maximum stress criterion are employed to predict the failure of the yarn and matrix material, respectively. A material degradation scheme is implemented to account for the decrease in the elastic constants of the material. The initiation and progression of failure within a plain weave textile composite has been predicted.

Dedication

To my parents, Ed and Judy Glaessgen, whose belief in me has never faltered.

Acknowledgments

The author wishes to express his gratitude for the advice, guidance, and steadfast support of his major professor, Dr. O.H. Griffin, Jr. In addition, he wishes to thank Drs. M.W. Hyer, E.R. Johnson, D.H. Morris, and S.A. Ragab for providing assistance and advice through their capacity as members of his committee.

This work was funded through the NASA-Virginia Tech Composites Program (NVTCP) at Virginia Tech and supported as part of the Mechanics of Textile Composites Working Group (TMWG) of the Mechanics of Materials Branch (MeMB) at NASA Langley Research Center (NASA Grant NAG-1-343). The author gratefully acknowledges the support of Dr. M.W. Hyer, the Director of the NVTCP, and Drs. C.E. Harris and I.S. Raju, former and current Head's of the MeMB. The author had the opportunity to work with many talented engineers as part of the TMWG, in particular, the assistance of Dr. C.M. Pastore is greatly acknowledged. Finally, the author would like to thank his grant monitor, Mr. C.C. Poe, Jr., for his continued support, advice, and patience through the course of this research..

Through the course of a graduate program, one encounters many students, staff, and faculty who provide assistance, support, and insight. The author would like to thank all of these fine people. In particular, he is grateful to Dr. S.T. Burr for his many helpful discussions regarding the experimentally determined behavior of the textile material systems discussed in this document. Thanks also to Mr. S.A. Ragon and Dr. D.E. Hutchins for their helpful suggestions regarding the composition of this text. Special thanks to Mr. D.S. Taylor (root) for his assistance with the departmental computing systems. Thanks are also due to Dr. R.D. Kriz and Mr. J.D. MacRae for their helpful discussions concerning the vizualization of the results discussed in this text and to Dr. F. Ahmad and the National Center for Supercomputing Applications for the use of their computer facilities.

Table of Contents

1.0 Introduction	1
1.1 General Background on Textile Composites	1
1.1.1 Textile Preform Composites, their Role as Structural Materials	1
1.1.2 Micromechanics and Textile Structural Composites	5
1.1.2.1 Fundamental Assumptions in Micromechanics	5
1.1.2.2 The Concept of a Representative Volume Element	6
1.2 Motivations and Objectives	6
2.0 Literature Review on Modeling of Textile Composites	9
2.1 Geometry, Micromechanics, and Elastic Properties Papers	9
2.1.1 Outline	9
2.1.2 Textile Geometry Models	9
2.1.3 Laminate Models	11
2.1.4 Mosaic Models	12
2.1.5 Fiber Undulation (Crimp) Models	12
2.1.6 Bridging Models	13
2.1.7 Spatially Inclined Fiber Models	14
2.1.8 Simplified Finite Element Models	14
2.1.9 Detailed Finite Element Models	16
2.2 Failure and Progressive Failure Papers	18
2.2.1 Outline	18
2.2.2 Failure Criteria	18
2.2.3 Failure and Damage Predictions	20
2.2.4 Progressive Failure	21
3.0 Finite Element Model Development and Verification	27
3.1 The Textile Geometry Model	27
3.1.1 Theory and Discussion of the Textile Geometry Model	27
3.1.2 Analytical Basis	28
3.2 The Solid and Finite Element Models	29
3.2.1 Conversion of TGM Data to a Solid Model for FEA	29
3.2.2 Considerations in Finite Element Modeling	32
3.2.3 Constituent Properties	37
3.3 Model Verification	40
3.3.1 Effects of Model Geometry	40
3.3.2 Comparison to the Mosaic Model	41

3.3.3 Satisfaction of Global Equilibrium	46
3.3.4 Verification Using Results Obtained by Experimentation	46
4.0 Finite Element Results for a Plain Weave	49
4.1 Thermal Loading	51
4.1.1 Displacement Results	52
4.1.1.1 Periodic Boundary Conditions	52
4.1.1.2 Out-of-Plane Boundary Conditions	53
4.1.1.3 In-Plane Boundary Conditions	54
4.1.2 Strain Energy Density Results	55
4.2. Mechanical Loading	57
4.2.1 Displacement Results	57
4.2.1.1 Periodic Boundary Conditions	57
4.2.1.2 Out-of-Plane Boundary Conditions	58
4.2.1.3 In-Plane Boundary Conditions	59
4.2.2 Strain Energy Density Results	60
4.3 Summary of Results and Discussion for a Plain Weave	60
5.0 Progressive Failure Model Development and Verification	64
5.1 Failure Criteria	64
5.1.1 Failure Criteria for Isotropic Materials	64
5.1.1.1 Maximum Stress Criterion	65
5.1.1.2 Maximum Strain Criterion	66
5.1.1.3 Maximum Shear Stress (Tresca) Criterion	67
5.1.1.4 Maximum Distortion Energy (von Mises) Criterion	67
5.1.2 Failure Criteria for Transversely Isotropic (or Orthotropic) Materials	67
5.1.2.1 Maximum Stress Criterion	68
5.1.2.2 Maximum Strain Criterion	68
5.1.2.3 Tsai-Hill Criterion	69
5.1.2.4 Tsai-Wu Criterion	69
5.1.2.5 Hashin's Criterion	70
5.2 Progressive Failure Model	71
5.2.1 Selection of Failure Criteria	71
5.2.2 Damaged Material Formulation	72
5.2.2.1 Damaged Material Formulation - Matrix	72
5.2.2.2 Damaged Material Formulation - Yarns	73
5.2.3 Assumed Stress-Strain Relationship	76
5.2.4 Computational Procedures	78
5.3 Verification of the Progressive Failure Model	81
5.3.1 Development of a Verification Procedure	81
5.3.2 Results of the Verification Procedure	85
6.0 Failure Model Results for a Plain Weave	87
6.1 Cases Considered: Material Properties, Loading, and Boundary Conditions	87
6.1.1 Material Properties	87
6.1.2 Loading	90
6.1.3 Boundary Conditions	92
6.2 Analysis of a Fiberglass/Epoxy Material	92

7.0 Contributions and Recommendations	96
7.1 Contributions	96
7.2 Conclusions	97
7.3 Recommendations	98
References	99
Appendix A: Glossary of Terms for Textiles	106
Appendix B: Figures from Chapter 4	108
Appendix C: Figures from Chapter 6	138
Vita	144

List of Illustrations

Figure 3.1.2a.	Solid model representation of yarns in a plain weave textile.	30
Figure 3.2.1a.	Flowchart of the model generation proceedure.	31
Figure 3.2.1b.	Edge view of the representative volume element (RVE).....	33
Figure 3.2.1c.	Isometric view of the representative volume element (RVE).....	34
Figure 3.2.1d.	Isometric view of the bulk matrix material within a RVE.....	35
Figure 3.2.2a.	Isometric view of a typical finite element discretization.	39
Figure 3.3.2a.	Geometrical idealization of the mosaic model.....	44
Figure 3.3.2b.	Modified geometrical idealization of the mosaic model.....	45
Figure 4.0a.	Example for the interpretation of isosurfaces.	50
Figure 5.2.3a.	Assumed stress-strain behavior for the constituent materials.....	77
Figure 5.2.4a.	Flowchart of the progressive failure algorithm.....	79
Figure 5.2.4b.	Newton-Raphson routine.	82
Figure 5.3.1a.	Geometry and boundary conditions of verification model.	83
Figure 5.2.3b.	Load history for verification model.	84
Figure 5.3.2a.	Loading direction stress-strain behavior for verification model.....	86
Figure 4.1.1.1a.	Axial displacement, U_x . Periodic boundary conditions.	109
Figure 4.1.1.1b.	Out-of-plane displacement, U_y . Periodic boundary conditions.....	110
Figure 4.1.1.1c.	Transverse displacement, U_z . Periodic boundary conditions.	111
Figure 4.1.1.2a.	Axial displacement, U_x . Free top surface.	112
Figure 4.1.1.2b.	Out-of-plane displacement, U_y . Free top surface.	113
Figure 4.1.1.2c.	Axial displacement, U_x . Free top/bottom surface.	114
Figure 4.1.1.2d.	Out-of-plane displacement, U_y . Free top/bottom surface.	115
Figure 4.1.1.3a.	Axial displacement, U_x . Free front surface.	116
Figure 4.1.1.3b.	Transverse displacement, U_z . Free front surface.	117
Figure 4.1.1.3c.	Axial displacement, U_x . Free front/back surface.	118
Figure 4.1.1.3d.	Transverse displacement, U_z . Free front/back surface.	119
Figure 4.1.2a.	Strain energy density, SED. Periodic boundary conditions.	120
Figure 4.1.2b.	Strain energy density, SED. Free top/bottom surface.....	121
Figure 4.1.2c.	Strain energy density, SED. Free front/back surface.....	122
Figure 4.1.2d.	Strain energy density, SED. Periodic boundary conditions. Glass/epoxy yarns.....	123
Figure 4.2.1.1a.	Axial displacement, U_x . Periodic boundary conditions.	124
Figure 4.2.1.1b.	Out-of-plane displacement, U_y . Periodic boundary conditions.....	125
Figure 4.2.1.1c.	Transverse displacement, U_z . Periodic boundary conditions.	126
Figure 4.2.1.2a.	Axial displacement, U_x . Free top surface.....	127
Figure 4.2.1.2b.	Out-of-plane displacement, U_y . Free top surface.	128
Figure 4.2.1.2c.	Axial displacement, U_x . Free top/bottom surface.	129

Figure 4.2.1.2d.	Out-of-plane displacement, U_y . Free top/bottom surface.....	130
Figure 4.2.1.3a.	Axial displacement, U_x . Free front surface.	131
Figure 4.2.1.3b.	Transverse displacement, U_z . Free front surface.....	132
Figure 4.2.1.3c.	Axial displacement, U_x . Free front/back surface.....	133
Figure 4.2.1.3d.	Transverse displacement, U_z . Free front/back surface.	134
Figure 4.2.2a.	Strain energy density, SED. Periodic boundary conditions.	135
Figure 4.2.2b.	Strain energy density, SED. Free top/bottom surface.	136
Figure 4.2.2c.	Strain energy density, SED. Free front/back surface.....	137
Figure 6.2.1a.	Axial response of a glass/epoxy material with periodic boundary conditions.....	139
Figure 6.2.1b.	Onset of tensile matrix mode damage in a glass/epoxy material with periodic boundary conditions.....	140
Figure 6.2.1c.	Progression-1 of tensile matrix mode damage in a glass/epoxy material with periodic boundary conditions.....	141
Figure 6.2.1d.	Progression-2 of tensile matrix mode damage in a glass/epoxy material with periodic boundary conditions.....	142
Figure 6.2.1e.	Progression-3 of tensile matrix mode damage in a glass/epoxy material with periodic boundary conditions.....	143

List of Tables

Table 3.2.3a. Geometry of the representative volume element36

Table 3.2.3b. Elastic properties of the materials considered..38

Table 3.3.2a. Stiffness comparison between the mosaic and finite element models.....42

Table 3.3.3a. Stiffness comparison between experimentation and the finite element model.....48

Table 4.3a. Maximum values for quantities from thermal loading..62

Table 4.3b. Maximum values for quantities from mechanical loading..63

Table 3.2.3b. Elastic properties of the materials considered..88

Table 6.1.1a. Failure stresses of the idealized materials considered..89

Table 6.1.1b. Elastic properties of the materials.....91

Table 6.2.1a. Load history for a glass/epoxy material with periodic boundary conditions.....93

1.0 Introduction

This chapter is divided into two primary sections. The first is background on forms of textile composites, their applications and the basic assumptions of the micromechanical analyses used to model them. The second is a discussion of the motivations and objectives of the present work.

1.1 General Background on Textile Composites

1.1.1 Textile Preform Composites, their Role as Structural Materials

Although laminated composites have gained wide acceptance in aerospace and other industries, they do have disadvantages. Among these is a significant lack of damage tolerance. Because design allowables necessarily account for the performance of a damaged component, aircraft components made of laminated composites must be designed for maximum stresses or strains that are much lower than the undamaged strength of the materials. Textile composites offer significantly improved damage tolerance compared with traditional laminated materials though they do have decreased in-plane properties. However, since the residual strength of the damaged textile composite is typically higher than that of a corresponding laminate, the design allowables for the parts may actually be higher [1.,2.].

The broad classification of textile preform composites includes nonwoven, knitted, woven and braided forms of reinforcement impregnated with a matrix material [3.,4.]. Perhaps the most common of the material systems is glass, aramid, or carbon yarns in a polymer matrix. Although each architecture and material sys-

tem possesses unique advantages and disadvantages for structural applications, the class of materials has several key advantages over laminated unidirectional materials. Among these are the following:

- Enhanced / versatile manufacturability
- Delamination / impact resistance
- Reduced weight

Technologies for manufacturing textile based composite preforms are a direct result of the technologies developed for manufacturing textiles for clothing and related consumer goods [5.]. This basic technology has been built through centuries of development and may be considered one of the most mature developed by man. Until recently, however, textile technology had not been used for structural applications. Currently, textile preform composites are being used or are being considered for use in the aerospace, automotive, marine, and other industries. The structural textile preform architecture may vary from a simple nonwoven material to a complex three-dimensional weave or braid. However, no single textile or other material form is ideal for all applications on a cost / performance / availability / processibility / machineability / joinability / maintainability basis [4.].

The development of nonwoven fabrics is a direct result of the need to reduce manufacturing costs associated with woven and other more complex material forms [6.]. Some of these nonwoven materials are similar to unidirectional preregs and typically consist of closely packed collections of fibers assembled in a somewhat regular, though unimpregnated, geometry, while others consist of fibers with random in-plane orientations. In either case, entanglement or friction between neighboring fibers maintains the integrity of the material before impregnation. A subset of nonwoven materials is the unidirectional yarn used as an intermediate component for more complex textile material forms.

More complex in architecture than nonwoven fabrics are knitted fabrics wherein the knitting loops are produced by introducing the knitting yarn either in the cross-machine direction (weft knit) or in the machine direction (warp knit) forming an integral structure [7.]. Although this material form has a lower maximum fiber volume fraction than woven materials, it does allow the introduction of directional reinforcement similar to braided preforms [8.].

Woven fabric prepregs are one of the most widely used of the fiber reinforced resin forms [9.]. Yarns or tows typically contain from 1000 to 12000 filaments and can be woven into many different weave patterns including plain weaves, twill weaves, and a number of satin weaves. The plain weave interlaces one warp yarn over one filling yarn, whereas the twill weave interlaces one or more warp yarns over and under two or more filling yarns. The satin weave consists of one warp yarn interlacing over a number of filling yarns. Uncured woven textile composites offer considerable drapeability allowing them to form simple contours such as those found in aircraft skins [7.]. Although not as impact resistant as braided materials, woven materials are simpler and more economical to manufacture.

Among the most complex of the textile preforms are braided materials. In the braiding process, two or more systems of yarns are interlaced in the bias¹ direction to form an integrated structure. Braided material differs from woven and knitted fabrics in the method of yarn introduction into the fabric and in the manner by which the yarns are interlaced [10.,11.]. Processes for braiding materials include two-dimensional and three-dimensional braiding with and without the introduction of longitudinal, or axial, yarns. It is the addition of these axial yarns that allows increased axial load bearing ability of the composite. Among the advantages of braiding is the ability to conform to complicated contours including cylinders, T-sections, C-sections, and the like, while maintaining a significantly higher specific strength and specific modulus than is found in metals.

The energy required for delamination or crack growth is a function of the specific in-plane and through-thickness architecture of the material. When a laminated material is impacted, damage occurs by many mechanisms including delamination and is facilitated by the poor interlaminar shear strength that is typical of laminates. Unlike laminates, textile composites do not have uniformly flat planes for delaminations to grow. Yurgartis and Maurer [12.] determined that weave parameters such as harness number, counter number, lacing number, relative stacking translation and stacking sequence can effect delamination resistance of woven textiles. For example, weaves with larger lacing numbers, such as plain weaves, may have a greater delamination resistance than weaves with smaller lacing numbers such as 8-harness satin weaves.

1. See Appendix A: Glossary of Terms for Textiles

In addition to the near-net shape formability, the most outstanding properties noted for two-dimensional and three-dimensional woven or braided composites are their damage tolerance and their ability to limit impact damage area [13.]. In general, the damage tolerance of the material is directly related to the level of interlacing or integration within the textile structure. In a study of 1x1 braids by Camponeschi, et.al. [14., 15.], it was noted that three distinct modes of damage are evident during the impact event including intertow cracking, intratow cracking, and intertow delamination. The braids retained approximately 50% greater stiffness than the control laminates, laminates with a similar material orientation, at the same impact level.

A study by Brookstein and Tsiang [16.] showed some of the versatility of braided materials, that is, the ability to form the braid around fastener holes rather than needing to drill through the material. In that study, braided $\pm 45^\circ$ graphite/epoxy cylinders with both integrally-formed and machined pin-loaded holes were studied. The composites with integrally-formed holes supported more than twice the load before initial failure than the composites with machined holes. The authors note that the integrally-formed holes effectively reduce the effect of the strain concentration because the load-bearing yarns are continuous and provide local stiffness in the loading direction.

Although manufacturability and impact/delamination resistance are two of the attractive features of textile composites they exist at the expense of the in-plane properties of the material. Textile composites have lower in-plane fiber volume fractions than laminated composites for two reasons. First, depending on the particular class of material and architecture considered, a considerable percentage of the total fiber volume fraction is aligned in the out-of-plane direction. Second, the architectures themselves do not allow for as large an overall fiber volume fraction as standard laminated materials. Typically, the result is a material with decreased in-plane modulus and strength.

A more complete discussion of the interaction between textile technology and composites engineering is provided by Hearle and Du [17.]. In this discussion, an overview of developments in fibers, matrices, and composites manufacturing is given with particular emphasis to the areas of composite shells and integrated three-dimensional structures such as winding, stitching, and weaving.

1.1.2 Micromechanics and Textile Structural Composites

Jones [18.] defines micromechanics as “the study of composite material behavior wherein the interaction of the constituent materials is examined in detail as part of the definition of the behavior of their heterogeneous composite material.” This definition was developed for laminated composites whereby the use of micromechanical analysis allows for prediction of the macromechanical behavior of an equivalent homogeneous lamina, or single ply of a laminated composite, from a knowledge of the geometry and constituent material properties. Thus, if the elastic constants of the matrix material and reinforcing fiber are known in addition to the fiber volume fraction and type of fiber packing array (geometry), the homogenized lamina elastic constants may be approximated.

1.1.2.1 Fundamental Assumptions in Micromechanics

The underlying philosophy of micromechanics that has been developed for laminated composites may be applied to the micromechanical analysis of textile preform composites albeit in a somewhat modified form. The basic assumptions associated with classical micromechanical analyses of a textile composite can be summarized as follows:

The equivalent textile composite is

- macroscopically homogeneous
- linearly elastic (or of predictable behavior)
- macroscopically orthotropic
- initially stress-free
- void free
- internally perfectly bonded

The yarns are

- homogeneous
- linearly elastic (or of known constitutive behavior)
- isotropic or transversely isotropic
- of a known and repeating geometry

The matrix is

- homogeneous
- linearly elastic (or of known constitutive behavior)
- isotropic

1.1.2.2 The Concept of a Representative Volume Element

Traditionally, a representative volume element (RVE) is defined as the smallest unit of repeating geometry within a material - for textile as well as laminated composites. Thus, the assumption is made that once the geometry and response of the RVE are determined, the geometry and response of the entire material is known if the internal actions are spatially homogeneous in some average sense. This imposes profound consequences on the analysis. If for example, one of the constituents within the RVE is determined to have failed, then all like constituents throughout the material have also failed. Although it is based on the geometric representation of a representative volume element, the finite element based approach developed for the present analysis allows boundary conditions other than the simple periodic boundary conditions to be studied. Thus, the definition of an RVE must be modified to allow the effects of applied load and/or imposed boundary condition to be included. Therefore, in the present study, the RVE is considered to be the smallest unit within the material that is representative of a particular geometry under an applied load and/or set of imposed boundary conditions producing a given material response.

The physical dimensions of the RVE must be much smaller than those of the overall textile structure. Simultaneously, the RVE must be much larger than the individual fibers within a yarn. This allows the details of the fiber matrix interaction within the yarn to be neglected, and the yarns to be considered as fundamental homogeneous constituents of the textile. Similarly, the bulk matrix material, that is, the matrix material located within the interstices between yarns, is also a fundamental constituent of the textile composite.

1.2 Motivations and Objectives

The modeling of these materials is considerably more complicated than modeling of laminated composites. These additional complexities result from the very reasons for the development of the materials, that is,

from the through-the-thickness yarns or fibers required to contain damage and/or prevent delamination growth. The work that has resulted from a multitude of researchers, including those affiliated with NASA Langley Research Center's Mechanics of Textile Composites Work Group [19.], has spanned many analytical techniques. These range from proven methods for the analysis of laminated composites to more complex analyses developed or modified specifically for the analysis of textiles. Each of these analyses has its relative advantages and disadvantages. For example, an analysis based on a classical lamination theory type of approach may provide adequate estimates for material stiffness at a very small computational expense, while being wholly inadequate for estimates of the stress states within individual components of the textile. The most serious obstacle to the more complex analyses is the relatively demanding computational effort required. However, with the advent of increasingly more powerful computers, even this problem may be overcome.

The advantages of a multifaceted approach to the analysis of textile based composites, such as the one undertaken by the Textile Mechanics Work Group, are readily apparent. Development of many tools for analysis, each with unique strengths and weaknesses, allows for one approach to complement another. As an example, a more detailed analysis might provide insights that allow a user of a more simplistic analysis to more fully understand material behavior and therefore better interpret the results of the simplified analysis. The present work is one facet of this multifaceted approach, that of a detailed analysis capable of predicting details of the material response under quasi-static mechanical and thermal loads.

For a detailed analysis such as the present one to be useful, it is desirable that it meet the following requirements:

- The analysis must provide information that is not available from more simplified and less expensive analyses such as those described in Section 2.1.3 through Section 2.1.7. If the only information that can be obtained is, say, in-plane elastic constants, then the overall effort of the analysis would be better served by referencing the classical lamination theory type of analyses, and
- The analysis should lend itself to the interrogation of a variety of material architectures, material properties, and loadings, and
- Results of the analysis should be interpretable by persons with little or no knowledge of the tools used to compute those results.

Regarding the first of these requirements, the vast majority of the work in the literature is based on a variety of techniques for reducing the three-dimensional nature of these materials to a two-dimensional form. None of these techniques is capable of interrogating the complex interactions found within the three dimensional structure. Those techniques that are geometrically three-dimensional, including many of those described in Section 2.1.9, rely on a simplistic geometry that is not based on a verifiable fabric architecture. The prediction of a first failure region and failure mechanism is only viable with the introduction of these complex analyses. The more accurate the geometry, the more reliable the results.

Difficulties with the second of these requirements is most often found in an inability to obtain information about the out-of-plane behavior of materials from two-dimensional analyses.

Finally, the third requirement is, in addition to the computational effort required, the most serious of the limitations of complex three dimensional analyses. Rather than a single “result” such as a modulus, or a mean stress, these analyses tend to produce an overwhelming quantity of information. Methods must be developed or instituted to deal with these data.

The work that follows addresses the three concerns mentioned previously. First among these, the analysis provides an interrogation of the details of the behavior of a woven textile composite through the elastic regime and well beyond the initial failure of the material. The second concern, flexibility of the method, is addressed since the analysis is based on the textile geometry model and the finite element method, thus little restriction is placed on the type of textile that may be modeled. Finally, the presentation of the results in a simple graphical format allows persons with little knowledge of either the textile geometry model, finite element model, or progressive failure model to comprehend the results of this analysis.

2.0 Literature Review on Modeling of Textile Composites

A literature review on techniques for and results of modeling composites based on textile preforms is presented in this chapter. The first section is a discussion of literature dealing with the geometrical and analytical modeling of textile based composite materials. The second section is comprised of literature on failure and progressive failure analyses including, but not limited to, those dealing with composite materials.

2.1 Geometry, Micromechanics, and Elastic Properties Papers

2.1.1 Outline

The work presented in this section is divided into the areas of: textile geometry models (2.1.2), laminate models (2.1.3), mosaic models (2.1.4), fiber undulation models (2.1.5), bridging models (2.1.6), spatially inclined fiber models (2.1.7), simplified finite element models (2.1.8), and detailed finite element models (2.1.9). The treatments considered here (or portions therein) are primarily concerned with the prediction of geometrical architecture, the elastic material constants, and the linear elastic behavior of the materials up to first failure.

2.1.2 Textile Geometry Models

Masters et. al. [20.] note that textile reinforced composites must be analyzed and evaluated as a structure and not a material and further, that the fiber architecture plays a more dominant role in these materials than

in unidirectional tape materials. The process science model developed by Pastore [21., 22.] used in conjunction with knowledge of the braid process used to fabricate the preforms, was implemented to successfully predict the braid architecture and the significant braid parameters such as average braid angle, fiber content, unit cell dimensions, tow spacing, and longitudinal/braider yarn ratio.

The approach of Pastore et. al. [21., 22.] to modeling the geometry of textile based composites consisted of three principal steps: (1) construction of mean centerline points for each yarn, (2) smoothing the centerlines with a B-spline interpolation to construct a smooth and minimum strain energy curve, and (3) constructing a three-dimensional object by sweeping a cross section along the centerline and forming a surface. Since the processing science model does not account for all secondary manufacturing effects, measured values of braid angle, thickness, distribution of longitudinal yarns, and yarn cross-sectional geometry were used to validate and modify the predicted values. Pastore and Ko [22.] determined that the maximum fiber volume fraction for a 3-D braid before the onset of distortion of the geometry is 68 percent.

Masters et. al. [20.] used the techniques developed by Pastore [21., 22.] to discuss the concept of the unit cell (also termed representative volume element, RVE) as a repeating unit of fabric geometry. This smallest repeating unit is representative of the complete yarn or tow intertwinement pattern. The authors note that to simplify the analysis, rectangular unit cells are preferable, though other geometries are possible.

Du et. al. [23.] reported a unit cell geometry of 2-step three-dimensional braids. In this analysis of the structural geometry of unit cell, diamond and ribbon shapes were assumed for the axial and braider yarns, respectively. Relationships between key process variables and the final fabric geometry were discussed, including the range of possible parameter combinations resulting from the bounds of yarn jamming and maximum fiber packing. These parameter combinations define the bounds on manufacturable material architectures (the process window) and, more importantly, material response. Both the analysis and a related experimental program showed that fiber volume fractions in excess of 75% (corresponding to the jamming point) are possible for these materials.

In contrast, the analyses for 4-step and 2-step three-dimensional braided structures by Li et. al. [24., 24.] assume a cylindrical cross-section for the yarns in the unit cell. In these analyses, a maximum yarn orienta-

tion angle of 55° and resulting 0.685 yarn volume fraction correspond to the yarn jamming point. Although the assumption of circular cross-sections is quite restrictive, the authors showed good correlation with experimentally determined values for preform surface angle, preform dimensions, and yarn volume fraction.

Du and Ko [26.] noted that the braiding angle is determined by the ratio of braid pitch length to yarn diameter, and that the braiding angle can approach 0° without yarn interlacing and can reach almost 90° if yarn slipping at the braid convergence point can be overcome. The maximum fiber volume fraction is achieved under yarn jamming conditions. At low braiding angles (less than 30°) the maximum fiber volume fraction is about 0.6, with an assumed fiber packing fraction of 0.785. It was noted that the maximum fiber volume fraction decreases with the increase in braiding angle. In addition, the fiber volume fraction of three-dimensional track-and-column braids has a wide range depending on the combination of braiding angle and braid tightness factor used. Also, the authors experimentally determined that the actual fiber volume fraction is close to its theoretical maximum value under jamming conditions due to the high yarn tension applied during braid formation.

The unit cell model presented by Armstrong-Carroll et. al. [27.] involves several simplifying yarn geometry assumptions including incompressibility, similitude of yarns, and circular cross-section. For a braid with these simplifying assumptions, the authors showed that a maximum overall fiber volume fraction of 0.79 and a maximum out-of-plane fiber volume fraction of 0.17 are possible for a maximum braid angle of 52° .

2.1.3 Laminate Models

Perhaps the simplest models that have been developed for the analysis of textile based composites are extensions of the classical lamination theory (CLT) developed for laminated composites. The $(0^\circ/\pm\theta)$ model [20.] can not be used to account for the out-of-plane undulations of woven or braided tows and includes the assumption that each set of like tows can be treated as a unidirectional ply in a $(0^\circ/\pm\theta)$ laminate. This analysis can be enhanced with the addition of a correction factor that accounts for braid undulation. The modification is made by determining the average of the absolute values of out-of-plane angle of the tows from photomicrographs of a cured material. Every textile based composite will have a nonzero average out-of-plane angle, and a corresponding decrease in in-plane stiffness. The authors showed this angle to be less than

$\pm 10^\circ$ for the braids studied. Correlation with experimentally determined values of elastic properties was fairly good for such a simple model. Differences of 7.5%, 27.4%, and 22.5% were noted for E_x , E_y , and ν_{xy} , respectively.

Additional CLT-based analyses for woven composites have been developed that account for yarn undulations [28., 29., 30.]. Although the analyses proved to be reasonably accurate, the analytical description of the yarn cross-sectional shapes and yarn paths make these analyses cumbersome to use.

2.1.4 Mosaic Models

Ishikawa and Chou [31.,32.,33.] discuss the development of the CLT-based mosaic models. In the mosaic model, crimp of the yarns is neglected resulting in discontinuity of the reinforcements, thus a fabric reinforced composite is idealized as an assemblage of pieces of two-ply cross-ply laminates. Thus, the repeating unit of the composite is considered as two-dimensional and all out-of-plane effects are neglected.

In the bounding approach discussed by Ishikawa and Chou [34.], the two-dimensional extent of the plate is simplified by considering two one-dimensional models where the pieces of cross-ply laminates are either in parallel or in series. In the parallel, or iso-strain model, uniform states of strain and curvature are assumed at the mid-plane. In contrast, the series, or iso-stress model, assumes an in-plane stress resultant at the mid-plane and ignores stress variations near the interface regions. From these models, the elastic moduli, Poisson's ratios, and shear moduli can be estimated. The predictions for in-plane axial compliance from the mosaic model and a simple two-dimensional finite element analyses are shown to converge for large values of fiber undulation where the crimp angle changes rapidly. These large fiber undulations minimize the effect of the angular portion of the yarns. The mosaic model has been adapted by Ishikawa and Chou [35.] to provide a simple estimate for the thermal expansion and thermal bending coefficients of simple weaves.

2.1.5 Fiber Undulation (Crimp) Models

Ishikawa and Chou [32.,33.] also discuss the development of fiber undulation models. The fiber undulation model takes into account the effect of fiber continuity and provides what is essentially a one-dimen-

sional analysis that may be suitable for estimating the behavior of plain weave composites. This model is similar to the model used for the upper bound in the bounding approach, however, the compliance matrices depend on a continuous x -coordinate. For plain weaves, the fiber undulation model predicts a softening of in-plane stiffness as compared to the mosaic model, but does not predict an undulation effect on the coupling constants [34.]. In a related study on in-plane thermal expansion and thermal bending, Ishikawa and Chou [35.] showed that under thermal loading, fiber undulation has no effect on either the thermal bending coefficients or the bending-stretching coupling constant.

This model has been extended and adapted by Yang and Chou [33.] to analyze triaxially woven composites and by Yang, et. al. [37.] for three-dimensionally braided composites. In these models, the authors consider an idealized unit cell whereby all yarns are composed of straight segments oriented at the yarn's mean orientation angle. In addition, the yarn interactions among the several yarns in the unit cell are not considered. A comparison with a limited quantity of experimental data showed that the model predicted the axial elastic modulus and Poisson's ratio reasonably well.

2.1.6 Bridging Models

Ishikawa and Chou [32.,33.] discuss the development of bridging models as a better approximation of the two-dimensional load transferring behavior of satin composites. In this model, the interactions between an undulated region and the surrounding regions having straight yarns is considered. As with the mosaic and fiber undulation models, Ishikawa and Chou [35.] adapted their bridging model to analyze thermally induced behavior of simple weaves. They showed that the bridging model better accounts for the load transfer mechanism in these materials because it separately models the straight portions of the yarns. Uniform strain and curvature are assumed in the bridging regions. For the thermal bending coefficients, there is considerable discrepancy between the results from the one-dimensional models and the bridging models. The bridging model was shown to be better suited for the prediction of thermal expansion coefficients of satin weave composites than either the mosaic or fiber undulation models.

2.1.7 Spatially Inclined Fiber Models

Spatially inclined fiber models are an extension of the fabric geometry models [38.]. The version of the fabric geometry model used for this analysis neglected the crimp in the yarns by allowing yarns to intersect at the center of the volume. The models developed by Ma et. al. [39.] consisted of a brick-shaped element of bulk resin enclosing four parallel bar (beam or spar) elements along the four longitudinal edges and four diagonal bar elements intersecting at the center of the brick. These bar elements are representative of longitudinal and braiding yarns, respectively.

Masters et. al. [20.] adapted the model developed by Ma to their material system, a triaxially braided carbon/epoxy textile composite. As with their laminate model, they showed a favorable comparison between this simple model and experimental data. Differences between experimentally determined and computed values of E_x , E_y , and ν_{xy} were shown to be 3.6%, 24.9%, and 23.8%, respectively.

Additional work discussed in Gowayed [40.] and Pastore and Gowayed [41.] involved the development of a self-consistent fabric geometry model (FGM) method to predict the elastic response of textile based composites. The work focused on the development of the transformation tensor, based on the FGM, that could transform the local stiffness matrix to the global stiffness matrix. Both stiffness and compliance averaging approaches were discussed. The upper boundary of the computed elastic constants was estimated by the stiffness averaging whereas the lower boundary was estimated by compliance averaging. In all cases, the stiffness averaging technique gave better estimates to the elastic constants than the compliance averaging.

2.1.8 Simplified Finite Element Models

Several types of simplified finite element models have also been used to analyze textile composites. The method discussed by Masters et. al. [20.] involves the analysis of a detailed unit cell of the reinforcing architectures in terms of sub-cells. The size of the subcells can be reduced to be as small as practical to improve the approximation of mechanical properties. The sub-cells may be homogeneous or inhomogeneous and may contain only yarn, only bulk resin, or both yarn and bulk resin. The material properties of each sub-cell were computed using the inhomogeneous finite element initially developed by Foye [42.]. The elastic prop-

erties of the material were then computed by formulating a stiffness matrix for the unit cell and solving unit displacement problems with appropriate boundary conditions. Differences between experimentally determined and computed values of E_x , E_y , and ν_{xy} were shown to be 2.9%, 25.1%, and 19.6%, respectively.

Yurgartis and Maurer [12.] present a somewhat vague description of a model developed to analyze “inter-laminar” shear stresses in fabric composites. In that study, the authors attempted to determine the effect of various stacking configurations on the shear stress distribution. In another study, Kriz and Muster [43.] and Kriz [44.] defined and analyzed a unit cell for a plain weave assuming generalized plane strain.

Lei et. al. [45.] discuss the concept of finite cell modeling (FCM) of unit cells of textile composites. The geometry used in this analysis was from the computer aided geometric model (CAGM) developed by Pastore [46.]. In this analysis, similar to the other unit cell based techniques, the composite is considered as an assemblage of a finite number of individual brick shaped repeating unit cells. Internally the unit cell is treated as a pin-joined space truss having degrees of freedom associated with axial, flexural, and torsional deformation (6 degrees of freedom per node). Although all yarn-matrix interaction is ignored, this analysis was shown to provide a reasonable estimate of the elastic stress-strain behavior for the three-dimensional braid considered. A similar analysis by Carter [47.] uses a type of spar in a matrix approach that, while being computationally efficient, also does not consider many important geometric details.

Naik [48., 49.] discusses the development of a general purpose micromechanics analysis that discretely models the yarn architecture within the repeating unit of the textile and is implemented in a code called Textile Composite Analysis for Design (TEXCAD). Geometric parameters considered in an analysis of plain weaves, satin weaves, and two-dimensional braids were the yarn cross-sectional area, yarn thickness, and yarn paths. The yarn cross-sectional shapes were considered to be composed of two flat portions defining the thickness of the yarn connected by two sinusoidal lenticular end portions at the edges. Yarn paths for each yarn were simplified as well. Here, the yarn was assumed to follow a path described by two straight segments and three sinusoidally undulating segments. Further, when contact between the yarns was determined to exist, the warp and weft yarns were assumed to contact completely along their flat portions.

The yarns were discretized by dividing them into piecewise linear segments, where the straight portions of

the yarn were considered as being composed of a single segment while the undulating portions were divided into n equal segments. Once segmentation was completed, the three-dimensional effective stiffness of the yarns was computed by treating the textile as a spatially oriented fiber composite composed of individual yarn segments with transversely isotropic material properties at a known orientation. A stress averaging technique was used to compute the material's elastic constants. As with many other numerical techniques for computing properties of textile composites, the nesting of the layers in a multi-layer assembly was not considered in this analysis.

Naik performed a parametric study to determine the effect of geometric parameters on computed stiffnesses for a plain weave textile composite. From this study, it was determined that the in-plane moduli was inversely proportional to yarn size, while out-of-plane modulus was proportional to yarn size. Further, for two-dimensionally braided textiles, the author showed that in-plane properties were very sensitive to braid angle, while out-of-plane properties were not.

2.1.9 Detailed Finite Element Models

Perhaps the first fully three-dimensional finite element models of textile composites were developed by Dasgupta et.al. [50.]. The authors used photomicrographs of a cross-section of a plain weave of glass/epoxy to determine geometric parameters used for their modeling effort. They observed the yarn cross-sections to be lenticular, of an approximately similar geometry in both the warp and fill directions (although a 5 percent difference in warp versus fill yarn undulation was noted, it was ignored), and to have a 63 percent fiber volume fraction. The RVE was determined to have a 28-29 percent overall fiber volume fraction. Dasgupta's model was constructed from geometric values taken from these experimental observations.

This model was expanded by Dasgupta et. al. [51.] to study the response of the representative volume element of a glass/epoxy plain weave textile used for electronic packaging. The focus of this work was to parametrically determine the effect of fiber volume fraction on constitutive properties. The authors determined that while the stiffness increases with increasing fiber volume fraction, the values of coefficient of thermal expansion and Poisson's ratio decrease.

In another work by Dasgupta et. al. [52.], a three-dimensional series-parallel thermal resistance network was developed and coupled with the finite element model to solve a steady-state heat transfer boundary value problem for a unit cell of a plain weave. The effective orthotropic material conductivities were obtained analytically and numerically as functions of (1) thermal conductivity of the constituent materials, (2) fiber volume fraction, and (3) weave geometry. The authors showed good agreement between their analysis and experimentally determined values for thermal conductivity as a function of overall fiber volume fraction.

Additional three-dimensional finite element analyses were performed by Whitcomb [53., 54., 55.]. In those analyses, the author studied the effect of tow waviness on the effective moduli and Poisson's ratios in addition to strain concentrations in the regions of yarn cross-overs. Whitcomb concluded that the in-plane moduli were inversely proportional to the tow waviness. Further, it was noted that the tow waviness causes large normal and shear strain concentrations at the yarn cross over regions in the weave.

Lene and Paumelle [56.] discuss the use of the Von Mises stress and a slipping parameter as a means of quantifying the behavior of their finite element model of a glass/epoxy plain weave woven composite. Included in another finite element study by Blacketter et.al. [57.] is a discussion of modeling of a simplified plain weave and correlation of gross axial and shear stress-strain behavior with simple tension and shear test data.

The development of an improved inhomogeneous finite element for the analysis of fabric reinforced composite materials is discussed by Foye [42.,58.,59.]. In these works, the author has attempted to deal with the problem of the ever increasing model size that is required to investigate the response of textile composites. The analysis uses a basic unit cell concept wherein the unit cell is divided into regular subcells independent of local material system. In this particular analysis, three types of material properties are considered: yarn, matrix, and yarn-matrix. Although this approach greatly simplifies the discretization process by allowing a regular mesh of hexahedral elements to discretize a three-dimensional domain, several added complexities are incurred that are not found in conventional finite element analyses. Convergence with diminishing element size becomes less certain, and stress computation for each material within the inhomogeneous elements becomes more complex. Foye showed that for the simplified case of a laminated material,

convergence for inhomogeneous elements is slower than for homogeneous elements. However, the author notes that as the size of the inhomogeneous elements decreases, both the accuracy and convergence rate improve.

Additionally, contributions to the field of textile mechanics have been made by the present author and his coworkers [1.,2.,60.,61.,62.]. The details of this work is presented in it's entirety in the chapters that follow. A detailed review of the work that has been published in the field of prediction of the elastic response of textile based composites is presented by Raju et. al. [63.].

2.2 Failure and Progressive Failure Papers

2.2.1 Outline

The work presented in this section is divided into the areas of: failure criteria (2.2.2), failure predictions (2.2.3), and progressive failure (2.2.4). The treatments considered here (or portions therein) are concerned with the modeling of the behavior of the materials at the point of initial failure and beyond. Since little work has been published on the failure modeling of textile based composite materials, research on the failure of other materials has been cited where appropriate. Specifically, work dealing with laminate composite materials and, in a few instances, work concerning the failure of isotropic materials has been included.

2.2.2 Failure Criteria

In the work by Batdorf [64.], a unidirectional composite is considered to contain damage in the form of breaks in the fibers. "There will be single isolated breaks that [shall be designated] as singlets, pairs of brakes [called] doublets, as well as triplets, quadruplets, or in general "i-plets." This work includes several key assumptions. Among these, that the overstress extends over a distance d_1 , but diminishes with distance from the cross-section containing the break. This is a point neglected in almost all prior treatments of this type. A doublet is considered to have n_2 nearest neighbors each subjected locally to a stress concentration factor c_2 , with the varying overstress applied over a length d_2 . Also, fiber failure is assumed to conform to a Weibull 2-parameter representation. If the cumulative probability of failure, P_f is much less than one, the

relation can be given in a simplified form. This form of solution is presented in the text [64.]. Batdorf defines the failure stress as the lowest stress at which any unstable i-plet is present. While the accumulation of damage in the composite is worked out in a manner close to the Weibull theory (based on a cumulative probability of failure at a given stress), the failure criterion is analogous to Griffith's crack instability theory.

In a follow on work, Batdorf and Ghaffarian [65.] continue the discussion of the implementation of the work presented in [64.]. The conventional theoretical interpretation of failure data is to assume that the composite is a simple Weibull material, that is, it has a fixed value of Weibull modulus, m . Accordingly, the different measured values of m are due to statistical fluctuations. Actually, the prediction and measured values may differ by 33% with this assumption. Conversely, Batdorf's analysis assumes that a multiplet always has the form most nearly resembling a penny shaped crack in a square array of fibers. Batdorf's analysis for the corresponding effective values of predicted Weibull shape modulus for the coupon in tension are 63, 66, and 66 respectively, as compared with the measured value of 24. The predicted coupon tensile strengths are about 5% above the experimental value. Batdorf gives two explanations for the discrepancy in Weibull's shape parameter: first, scatter in experimental data, and second, large differences in m may not be statistically significant.

The authors [65.] note that the Weibull modulus for a composite can be many times the modulus of the component fibers and that the composite modulus increases with composite size. Stress transfer actually occurs from one fiber to its nearest-neighbors and next-nearest-neighbors, etc. Thus, actual stress concentration factors are overpredicted by previous analyses. Finally, based on these analyses, the authors predicted that the strength of a large composite constructed of tows will be greater than that of a composite composed of the same number of equally spaced fibers.

According to Hashin, the microstructural aspects of failure are of such complexity that there is little hope of resolution of this problem on the basis of micromechanics methods [66.]. Such methods would require analytical detection of successive microfailures in terms of microstress analysis and microfailure criteria and prediction of the coalescence of some of them to form microfailures "...an intractable task." Hashin's failure is quadratic in stresses - the choice of quadratic is based on curve fitting considerations and not on physical reasoning.

Since the material is transversely isotropic, the failure criterion must be invariant under any rotation of the x_2 , x_3 axes around x_1 . Therefore, the failure criterion can be at most a function of the stress invariants under such rotations. According to Hashin, a general failure criterion for unidirectional fiber composites should distinguish among the various different failure modes of the composite and model each separately. A general failure criterion cannot be smooth but rather piecewise smooth, consisting of smooth branches each of which models a distinct failure mode. It is essential to know how the elements have failed; by fiber rupture, matrix crack, or delamination from adjacent laminae.

The second Piola-Kirchhoff stress has been used in conjunction with the Tsai-Wu criterion for biaxial strength predictions for plain weave glass composites [67.]. In this nonlinear analysis, Fujii et.al. concluded that the combination of PK2 stress and Tsai-Wu failure prediction had a better correlation with experimentally determined failure loads than did the prediction made with the nominal stress and the Tsai-Wu failure criterion.

Yamada and Sun [68.] present a failure criterion that incorporates the probabilistic nature of failure of composite materials. The criterion “employs a laminar shear strength that accounts for the lamination effect.” This “in situ shear strength” is noted by the authors to be of significant consequence in determining the strength of the laminate. A limitation of the author’s formulation is that it cannot be used for the prediction of failure when the transverse strength of the laminate governs failure.

2.2.3 Failure and Damage Predictions

Zang and Gudmundson [69.] discuss the prediction of the evolution of microcracks in composite laminates in addition to the response of laminates once they contain microcracks. The author’s theory for thermoelastic properties is exact, except for the solution for average crack opening displacement (COD). The authors make two additional points. First, energy release rate curves for the same material are different for different transverse ply thicknesses, and second, a single G criterion cannot govern the initiation and growth of micro cracks in transverse plies.

A damage mechanics based finite element analysis of general anisotropic problems is presented by Valiappan et.al. [70.]. This analysis involves the development of an orthotropic damage space and a damage state tensor. Both of which are used in the development of the stiffness matrix for the damage model in the finite element formulation. Shen et.al. [71.] present the concept of damage energy release rate. Similar to strain energy release rate in fracture mechanics, the damage energy release rate is used to characterize the mechanical response of an elastic material with anisotropic damage.

Lagoudas and Saleh [73.] present an approach to compressive strength modeling of fibrous composites subject to failure under kink band formation and propagation. The work bridges the micromechanics relevant to compressive failure due to fiber kinking with the global characteristics of a composite structure.

2.2.4 Progressive Failure

Petit and Waddoups [72.] present a method for predicting the nonlinear behavior of laminated composites by the incremental application of the average laminate stresses and utilization of a simple Euler-type integration procedure. A significant assumption of this method is that the laminate behaves linearly over the applied stress increment, that is, the previously converged state of the stiffness matrix is used for the current stress increment. The authors used their technique to solve a series of linear problems using a maximum strain criterion for failure of each of the lamina. Ultimate failure of the laminate was assumed when the laminate stiffness matrix became singular or when a negative sign appeared along its diagonal.

Kim and Hong [74.] discuss the development of a model for progressive failure of laminated composites with circular holes, but include little discussion of the actual implementation of the method. A more complete discussion of failure mechanisms, particularly implementation of the failure theory proposed by Hashin [66.] is given in Hwang and Sun [75.]. This later work also discusses the authors implementation of a progressive failure routine for laminates based on a modified Newton-Raphson method.

Development of a seven degree of freedom per node element for shear deformation and the implementation of the element in a progressive failure scheme is presented in Tolson and Zabaras [76.]. The system of failure modes determines the magnitude of stiffness reduction and decrease in the strength of a failed lami-

nate. Discussion of several different failure criteria is included.

Tan [77.] presents an item by item list of a computational procedure for progressive failure of composite laminates containing openings under tensile loading. In this analysis, the damaged state is accounted for by a system of degradation factors. Simple fiber and matrix failure are considered. In addition, the effect of mesh refinement and corresponding finite element sizes on the computational accuracy of the analysis are discussed, as is the effect of load increment size on the convergence of the analysis.

In a continuation of the work presented in [77.], Tan and Perez [78.] discuss a failure algorithm for the prediction of failure progression in laminates under compressive loading. In an analysis of a $[0_2/\pm 45]_{2s}$ AS4/3502 laminate, the authors determined that the micro-damage initiates at the hole boundary and grows as the load increases. The observed damage includes matrix cracking, fiber matrix splitting, delamination, fiber kinking, and microbuckling. This analysis is dependent on the use of what the authors define as internal state variables, or stiffness degradation factors D_1 , D_2 and D_6 . Here, D_1 is the stiffness degradation factor associated with fiber breakage; D_2 and D_6 are the degradation factors for transverse stiffness and shear stiffness respectively.

Swanson and Christoforou [79.] provide a brief discussion of a simple progressive failure analysis based on classical lamination theory. Included in their discussion is a softening rule which accounts for the effects of combined stresses on initial cracking and is used to degrade the material properties as failure progresses. The authors determined that 1) the progressive failure analysis involving the maximum stress or maximum strain criterion worked well, 2) the use of the original material stiffnesses in conjunction with the maximum stress or maximum strain criterion was somewhat less accurate, and 3) that the Tsai-Wu failure criterion gave extremely poor correlation with the experimental data.

A damage vector approach is presented by Singh and Digby for the analysis of anisotropic damage in brittle solids [80., 81.]. Specifically, it is discussed in the context of the analysis of brittle rocks. The damage in the material is defined to be irreversible in the sense that the initial, undamaged state cannot be recovered during unloading. The damage surface is assumed to be symmetric with respect to the sign of the transverse strain (ϵ_T), that is, the damage can grow in shear for “negative” as well as “positive” values of the in-plane

components of the strain traction vector. However, if ϵ_T is zero, the damage can grow only when the normal strain, ϵ_N , has a positive value, that is, in the absence of shear, cracks can grow in tension only. Analogous to the behavior of a yield surface in the theory of hardening in plasticity, the authors show that as the effective damage D^* increases, the corresponding damage surface expands in strain space. This approach is implemented in a finite element computer code.

A methodology for predicting crack growth and crack path in laminated composites is presented by Bakuckas, et.al. [82.]. In this work, node splitting mechanisms based on either the maximum normal stress or maximum shear stress failure criteria are discussed. Accordingly, crack growth is predicted node by node for both interior and fiber-matrix interface nodes. Each of four possible crack growth scenarios for crack growth at an interface node are considered including: fiber breakage, matrix crack blunting, matrix splitting, and interface crack growth.

Vaziri et.al. [83.] discuss a plasticity based constitutive model for laminated composites. As with other progressive failure routines seen in the literature, their routine uses a failure identification criterion followed by a progressive failure routine. In this case, a mixed incremental and Newton-Raphson iterative procedure is used to handle the nonlinearities in the equilibrium equations. At every load increment, all stress and strain components are checked against a failure criterion at the Gauss points in each layer of every element discretizing the laminate. Reasonable agreement with experimental data was shown.

In yet another study of progressive failure, an analytical model was developed by Fujita et.al. [84., 85.] to model flat braided composite bars with and without circular holes. The braided flat bar is divided into three distinct regions, the left, center and right, and two distinct phases, the “fiber bundles” and resin. The fiber bundles appear to be either spar or beam elements, thus continuity of displacements is observed only at nodal locations common to both the fiber bundle elements and the large hexahedral matrix elements. A non-linear incremental displacement method was used to discount the failed elements from the model.

Jones and coworkers [86.-90.] expressed the nonlinear orthotropic mechanical properties of composite materials as functions of both the linear and nonlinear response of the body. The strain energy density of an equivalent linear elastic body is used in addition to the initial slope, initial curvature, and change of curva-

ture of the stress-strain curve of the same body up to and beyond the material yield point. The material constants are determined by solution of a system of three equations using three points on experimentally determined stress strain curves.

In an extension of the work by Jones, Abu-Farsakh [91.] developed two material models for the nonlinear stress-strain behavior of composites. In the first model, the elastic strain energy density used in the Jones formulation is replaced by the plastic strain energy density of the system whereby the secant value is determined. In the second model, the elastic strain energy density of unloading is allowed to vary by modifying the initial elastic compliances at every stress or strain level to compensate for extension-shear coupling and for fiber reorientation effects. The authors give some details of the computational procedure in addition to comparison with experimentally determined values for the response of several materials. Reasonable correlation with experimental data was shown for both models.

A three-dimensional finite strain constitutive model was developed by a Fritzson [92.] for elastomer composites (primarily machine drive belts). Included in this formulation is the anisotropic elastic formulation separated into its volumetric and deviatoric components, the anisotropic rate independent dynamic elasticity, and the anisotropic viscoelastic response. Also included is damage due to mechanical and thermal degradation and the inclusion of damage mechanisms. This formulation was implemented into the ABAQUS finite element code as a user defined material subroutine.

Hwang and Sun [93.] have developed an iterative procedure using the finite element method to predict failure of laminated composites containing openings. The work includes a discussion of pertinent failure mechanisms and models, particularly implementation of the Hashin [66.] failure criterion. The nonlinear failure behavior was accounted for with several methods including the Newton-Raphson and the modified Newton-Raphson techniques. Both methods were shown to provide reasonable results. A method proposed by Gajer and Dux [94.] to work with nonlinear algorithms such as the Newton-Raphson and the modified Newton-Raphson controls load step size selection. This is done in an effort to reduce the amount of material nonlinearity at each load step within the computational algorithm to prevent divergence and spurious damage patterns.

Details of an algorithm for predicting failure progression in solid (three-dimensional) isotropic structures has been presented by Kukreti et. al. [95.]. Uniaxial stress-strain data is used as a basis for this material model.

Several contributions have been made by Chang and coworkers [96.-98.] to the literature on progressive failure of composite materials and structures. In each of these studies, the authors had three primary goals for their analysis: 1) to determine both the damage accumulated and reduction of mechanical properties within the laminate, 2) to determine the residual strength of the laminate, and 3) to determine the load at failure. The authors use the work of Yamada and Sun [68.] as their primary failure criterion. A property degradation model that considers fiber failure and matrix failure as the two distinct failure modes. For fiber failure, the authors use a Weibull distribution for residual stiffness of the longitudinal and shear moduli, however, the transverse modulus and Poisson's ratio are reduced to zero. For the case of matrix failure, the transverse modulus and Poisson's ratio are reduced to zero and the longitudinal and shear moduli remain unchanged.

Lee [99.] performed a three dimensional finite element study of damage accumulation in a composite laminate. The author used a simple eight node linear hexahedral element to model a rectangular laminated plate under biaxial loading. To produce a non-uniform stress state and focus the location of failure, the author included a geometric discontinuity in the form a circular cut out at the center of the plate. Three failure modes were considered in the study: fiber breakage, matrix failure, and delamination, all of which were analyzed using a maximum stress failure criterion. As with many similar analyses, a stiffness reduction corresponding to the particular failure mode was incorporated in this analysis. In particular, the entire element stiffness matrix was zeroed for a fiber failure, while only the terms corresponding to the direction of failure were zeroed for matrix failure and delamination.

Tsai [100.] argues that depending on initial failure mode, a laminate may retain a significant fraction of its original modulus up to final failure. The author reduces the properties of the damaged ply corresponding to the damage mode. For example, the transverse modulus of a cracked ply is not set to zero since it will still contribute to the stiffness of the laminate as long as it remains embedded in the laminate. Further, the author makes the assumption that, in the absence of a micromechanics model, the major Poisson's ratio is reduced by the same percentage as that of the matrix modulus.

Additional work in the area of progressive failure analysis of composite materials has been performed by Reddy and coworkers [101.-104.]. Included in each of these studies is a discussion of the plausibility of several failure theories for composite materials, including: maximum stress, maximum strain, Hoffman, Tsai-Wu, and Tsai-Hill. The authors showed that for in-plane loading of the composite plates, all failure criteria gave similar results. Several techniques for reducing the laminate stiffness beyond initial failure are also presented. This nonlinear analysis was used to predict a failure load that was much higher than the linear analysis failure load. As with the value of the failure load, the nonlinear analysis predicted failure locations (around a central hole) that were different than those predicted by a linear analysis [103.].

3.0 Finite Element Model Development and Verification

Included in this chapter is a discussion of the fundamentals of the textile geometry model developed by Chris Pastore [1.,21.,22.] that is used as a geometric basis for the finite element modeling. Also discussed is pertinent information on the development of the related solid and finite element models used in this study. Included in the final section of this chapter is a discussion of the several methods for validating the overall integrity of the finite element models.

3.1 The Textile Geometry Model

It is clear that the mechanical response of a reinforced material is dependent upon the type of reinforcement, constituent material properties, and the physical location and orientation of the reinforcing members. In the case of a textile reinforced composite, quantification of the geometrical properties of the reinforcement is rather complex. Thus, the first step in a detailed modeling approach is the development of methodologies for predicting and reporting the positions and orientation of the yarns contained within the representative volume element (RVE).

3.1.1 Theory and Discussion of the Textile Geometry Model

Considering that a yarn typically contains 12,000 or more filaments, it is computationally necessary to consider the yarn as a continuum. The physical and mechanical properties of this yarn can be determined

and predicted on the basis of the thousands of filaments, but the analyses will be based on yarns as fundamental elements.

Thus, the textile reinforcement can be considered as a collection of prismatic elements which bend, twist and undulate throughout the RVE. Ideally, the yarn can also vary its cross-sectional shape (although not area) depending on transverse pressure, twist level, fabric structure, etc.

The analytical solution to this problem meets serious difficulties because of the large number of mechanisms involved in the deformation of a fabric, such as crimp exchange; thread shear; extension, bending, twisting and flattening of yarns; friction between yarns and others. Another obstacle is a large number of required parameters. For example, in Pierce [105.], eleven parameters are needed in order to describe the geometry of a plain weave fabric and four to define the orthogonal components of stress and strain. Thus, the complete analysis of the fabric when considering all the parameters and mechanisms is an extremely difficult task. In order to predict mechanical behavior, varying degrees of simplification have been introduced including the assumption that the yarns are circular [105.].

In the present research, the geometrical and mechanical modeling is carried out on the structural level of the representative volume element (RVE), also termed the unit cell. The RVE can be built from segments of multiple yarns, where the number of yarn segments, their relative location, and the applied forces are determined entirely by fabric design.

3.1.2 Analytical Basis

The yarns forming a unit cell are considered to be elastic bodies interacting with one another and subject to external loads. The center line of every yarn is represented as a Bezier curve interpolating a set of discrete support points. In this study, a continuous Bezier with degree $n-1$ (over n support points per yarn) was used. The location of the support points fully determines the current mechanical state of the RVE and the yarns are assumed to have elliptical cross-sectional shapes.

Lagrange's principle of minimum work is used to determine the mechanical equilibrium of the system and

produce an analytical approximation to the material geometry. A discussion of the verification of this theoretical geometry along with additional details of the textile geometry model (TGM) is given in the contribution from Chris Pastore in Glaessgen et al. [1.]. A representation of a typical solid model of a four yarn RVE of a plain weave textile composite as determined from the textile geometry model is given as Figure 3.1.2a.

3.2 The Solid and Finite Element Models

For the present analysis, a plain weave fabric structure was chosen as the reinforcement scheme. Both a glass/epoxy and a carbon/epoxy material system were considered. The yarns were assumed to maintain a constant cross-sectional aspect ratio with elliptic shape throughout. Although the present technique allows for changes in yarn cross-section, the ability to account for changes in yarn cross-section has not yet been included in the textile geometry model. The fabric structure was a plain weave as shown in Figure 3.1.2a and discussed in this section.

3.2.1 Conversion of TGM Data to a Solid Model for FEA

Once the yarn cross-section and Bezier spline data are obtained from the TGM, they are directly converted to a format suitable for use in SDRC I-DEAS¹. First, the cross-section of the yarn is input as a series of discrete points on the yarn surface as determined with the textile geometry model. These points are fit to a B-spline representing the yarn perimeter as discussed by Tiller [106.]. Second, the yarn center line points are input and fit to a B-spline in a similar manner. The I-DEAS skin group for the yarns is developed by first creating a profile from the B-spline fit yarn cross-section. This profile is dragged along the cross-sectional spline to develop the yarn skin group. The logical flow of this process is illustrated in Figure 3.2.1a.

The solid modeling feature in I-DEAS is used to translate the yarn skin group to a yarn solid object. Creation of additional yarns proceeds in one of two ways. If an additional yarn is merely a translated or rotated version of the original, the appropriate I-DEAS commands are executed to preform the translation/rotation operation. If the yarn is unique (not a translated or rotated version of a previous yarn), the original yarn cre-

1. Available from Structural Dynamics Research Corporation, Milford, OH.

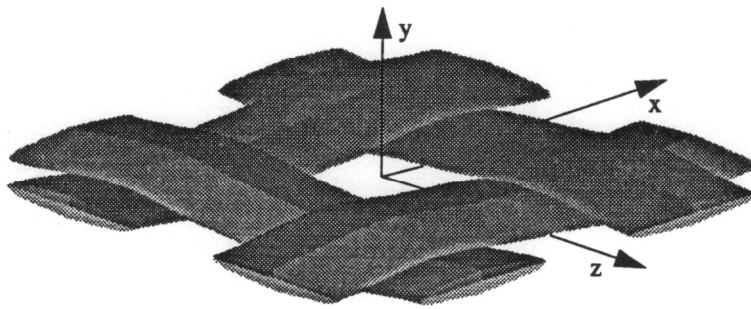


Figure 3.1.2a. Solid model representation of yarns in a plain weave textile.

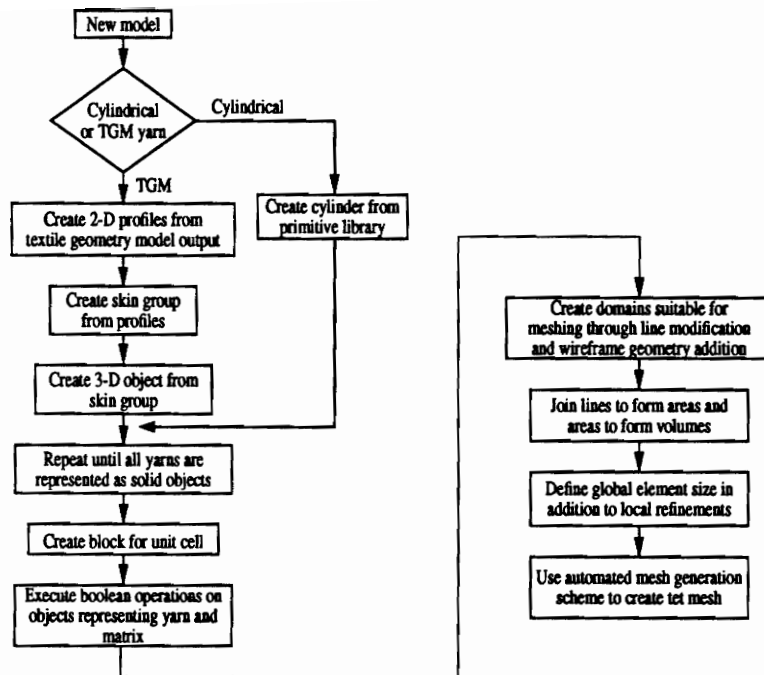


Figure 3.2.1a. Flowchart of the model generation procedure.

ation process is repeated beginning with the surface and/or spline points. Once created, all of the yarn solid objects are oriented in three-dimensional space to correspond to their locations within the textile geometry model.

The outer boundaries of the representative volume element are represented as a hexahedral shaped solid object oriented with its centroid at the centroid of the RVE. The boolean capabilities within I-DEAS are used to subtract the yarns from the outer block. The object that remains corresponds to the surrounding matrix contained within the RVE.

Once the RVE solid containing the details of the interior boundaries of the textile has been developed, the mesh area and mesh volumes are created. The original volume is considered matrix material, while the yarn volumes become yarn finite element volumes. The solid model representations of this woven textile are given as Figures 3.2.1b, 3.2.1c., and 3.2.1d. Note that Figure 3.2.1d is provided to show the domain of the bulk matrix material, that is, the RVE without the yarn material.

3.2.2 Considerations in Finite Element Modeling

Because of their three-dimensional structure, textiles tend to be computationally expensive to model with finite elements. Thus, it is desirable to model the RVE with as few elements as required for convergence. This leads to consideration of hexahedral elements, in particular to the quadratic hexahedra. Models composed of this element tend to converge quickly for a given number of degrees of freedom. However, current mesh generators can use this element only in conjunction with five- and six-faced volumes. Since the RVE may contain dozens or even hundreds of faces, the process of further subdividing the original single volume into an appropriate number of five- and six-sided subvolumes becomes prohibitively time consuming. Conversely, a mesh composed of quadratic tetrahedral elements can be used to discretize the complete matrix volume into finite elements. The yarn volumes are also discretized as complete volumes. The main disadvantage of tetrahedra-based meshes is the size of the resulting finite element models. Tetrahedra-based meshes are generally much larger than comparable hexahedra meshes.

Convergence of a finite element mesh can be determined through several methods. The method used here

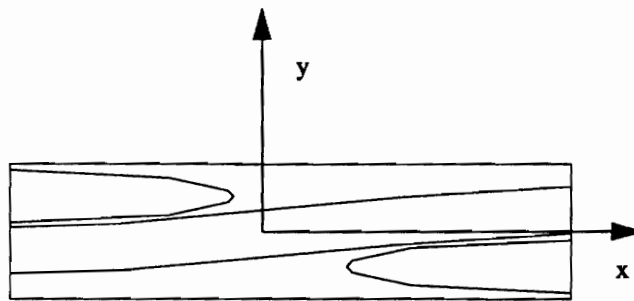


Figure 3.2.1b. Edge view of the representative volume element (RVE).

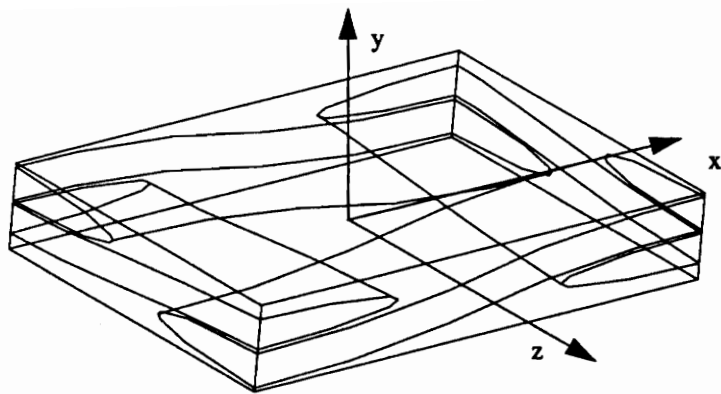


Figure 3.2.1c. Isometric view of the representative volume element (RVE).

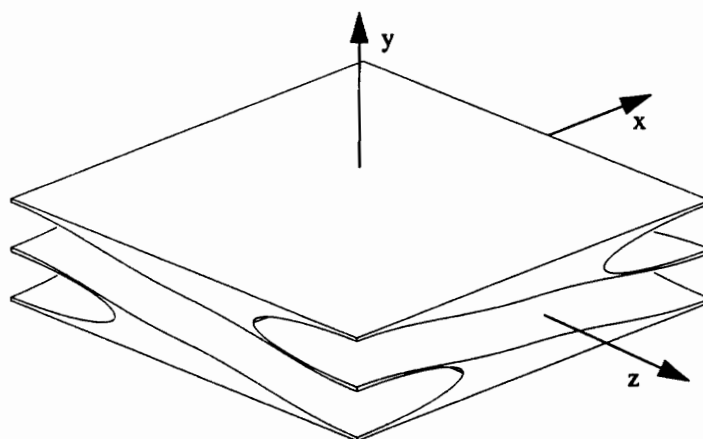


Figure 3.2.1d. Isometric view of the bulk matrix material within a RVE.

Table 3.2.3a. Geometry of the representative volume element.

RVE size (in)	a / b, axial yarn (in/in)	a / b, transverse yarn (in/in)
0.275 x 0.050 x 0.1960	0.0787 / 0.0098	0.0866 / 0.00866

is perhaps the most straightforward albeit most computationally expensive method. Here, the domain is meshed with an ever increasing level of refinement. Analyses of the plain weave with periodic boundary conditions and a uniform axial displacement that were based on models containing 23000, 35000, and 50000 degrees of freedom (DOF) were performed. The percent difference between the maximum values of strain energy density (SED) computed for each refinement was used as a convergence criterion. A comparison of the results of both the 23000 DOF and the 35000 DOF models with those obtained from the 50000 DOF model showed a 10 and 3% difference in computed maximum SED, respectively. From this information it was determined that both the 35000 DOF and 50000 DOF models would yield acceptable results. The results that are discussed in the upcoming chapters are from the 50000 DOF models.

Choice of proper discretization for volumes as complicated as those found in textiles leads to a trade-off between mesh convergence and model size. A typical global element size is approximately 1/20 of the model characteristic dimension, while local refinements are made to ensure convergence in known regions of high stress gradient. Once the finite element discretization of both the matrix volumes and the yarn volumes (shown as Figure 3.2.2a) has been completed and checked for element distortion, a concern considering the complex shape of the mesh volumes, the element coordinate systems of the yarn elements are aligned with the B-spline defining the orientation of the yarn volume. This alignment insures that the yarn finite elements will behave as subdomains within a homogeneous piecewise transversely isotropic material. Both materials were modeled with 10-node tetrahedron (ABAQUS¹ C3D10) elements.

3.2.3 Constituent Properties

The constituent properties of textile composites are best approximated as transversely isotropic yarns in an isotropic matrix. It is desirable to model the materials to match those approximations. Each tetrahedron has an internal coordinate system that defines its material orientation in space. By aligning the element principal material direction to be tangent to the yarn axis, the stiffness of the yarn becomes piecewise transversely isotropic. That is, the material orientation of the entire element is determined by the orientation at the centroid. Since the individual elements span small curvatures, this is a reasonable approximation to the continuous

1. Available from Hibbitt, Karlsson and Sorensen, Inc., Pawtucket, RI.

Table 3.2.3b. Elastic properties of the materials considered.

Material Properties	Epoxy Matrix	Glass / Epoxy Yarn	Carbon / Epoxy Yarn
E_x (E6 psi)	0.5	5.5	23.0
E_y (E6 psi)	0.5	1.43	1.58
E_z (E6 psi)	0.5	1.43	1.58
G_{xy} (E6 psi)	0.1875	0.59	1.00
G_{xz} (E6 psi)	0.1875	0.59	1.00
G_{yz} (E6 psi)	0.1875	0.55	0.60
ν_{xy}	0.33	0.27	0.27
ν_{xz}	0.33	0.27	0.27
ν_{yz}	0.33	0.30	0.30
α_x (E-6 in/in °F)	25.0	4.83	0.010
α_y (E-6 in/in °F)	25.0	19.6	11.50
α_z (E-6 in/in °F)	25.0	19.6	11.50

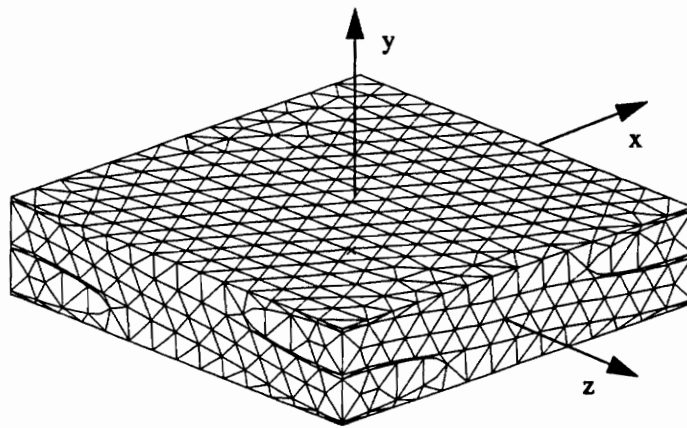


Figure 3.2.2a. Isometric view of a typical finite element discretization.

transversely isotropic properties of the actual yarn material.

Details of the RVE size and yarn dimensions corresponding to the results given in Chapter 4 are given in Table 3.2.3a. As shown in Figures 3.2.1b and 3.2.1c, the geometric renderings of the RVE, the x and z directions are the in-plane directions, while y is the out-of-plane direction. The material properties of yarn and matrix are given in Table 3.2.3b. It is important to note that these properties are considered to be generic properties for typical materials.

3.3 Model Verification

Included in this section is a discussion of a three-step verification procedure that uses an accepted analytical procedure [31., 34., 35.], a check on global equilibrium[107.], and data obtained from an experimental program [108.] to verify the ability of the present models to predict the simplest of material parameters, the elastic constants.

3.3.1 Effects of Model Geometry

It is appropriate to reiterate that material variability is not accounted for with any of the deterministic methods discussed in either the literature review (Chapter 2) or in the present modeling effort. As a result, the methods use a representative geometry, or representative volume element (RVE) that is assumed to repeat throughout the structure or throughout some portion of the overall structure. In this later case where the geometry or loading varies with location in the structure, it is assumed that the overall structure can be represented by a series of representative volume elements each describing all like portions of the material. If, however, the material variability is very large or the details of the material response is required at many locations within the structure, then the number of representative volume elements required to effectively model the structure may become prohibitive.

One of the factors contributing to the variability of cured textile composites is nesting. All textiles including the plain weave discussed here may nest to some degree. The extreme cases are adjacent layers of a weave that are unnested and those that are completely nested. Among other parameters, the degree to which

a textile is nested will effect the fiber volume fraction of the material that is included within a representative volume element. Fiber volume fraction, in turn, effects the elastic constants that are determined either through experimentation or analysis and will be a factor in the verification process that is described herein.

3.3.2 Comparison to the Mosaic Model

The well known mosaic models developed by Chou and his coworkers [31., 34., 35.] are used as a means of verifying the basic integrity of the finite element models that were developed in Chapter 3. As discussed in Chapter 2, the mosaic model is the simplest of the group of models that have been applied to study the response of textile based composites. Essentially, the mosaic model can be thought of as classical lamination theory applied to a textile composite. However, the simplistic nature of this model necessarily omits many of the geometric differences between the architecture of textiles and those of laminated composites.

Briefly, some of the important assumptions and simplifications that are found in the mosaic model include:

- approximating the material with a one-dimensional model neglecting shear deformations
- neglecting the continuity of the fibers in the thread direction
- regarding the fabric as an assemblage of pieces of asymmetrical cross-ply laminates
- analyzing the “laminates” using classical lamination theory where the asymmetry of the material may be accounted for with a simple correction factor on the “B” matrix
- computing the elastic stiffness constants A_{ij} , B_{ij} , and D_{ij} based upon the basic laminate where the top layer is the fill threads
- assuming either an iso-strain or iso-stress state for the textile

Each of the assumptions or simplifications can be examined for its general accuracy and validity. The analysis of a fully three-dimensional material such as a textile composite with a one-dimensional model necessarily neglects all of the interactions between the several components composing the material. Neglecting fiber continuity and the several assumptions related to the simplification of the geometry to allow a classical lamination theory analysis artificially stiffens the material and further neglects the interactions which produce three-dimensional response characteristics seen in the actual materials. This last shortfall is further compounded by the iso-strain or iso-stress assumption, as the response of the material is three-dimensional.

Since the mosaic model approximates the system of woven yarns and resin rich regions as a assemblage of homogeneous unidirectional layers, it provides an upper bound for the stiffness constants for a textile. Thus,

Table 3.3.2a. Stiffness comparison between the mosaic and finite element models.

Property	Mosaic	Modified Mosaic	FEA
E_x (E6 psi)	2.536	2.131	1.411
E_z (E6 psi)	2.536	2.131	1.239
ν_{xz}	0.1147	0.1185	0.1712
G_{xz} (E6 psi)	0.5900	0.4865	x

a fabric composed of a given percentage of axial yarns, transverse yarns, and resin volume is approximated by a material containing neither the out-of-plane contribution of the yarn, nor the contribution from the bulk resin. Rather, both the 90° and 0° unidirectional layers have the same material properties as the respective transverse or axial yarns (Figure 3.3.2a). The values for the upper bounds of the stiffness constants are given by Chou as

$$\overline{A}_{ij} = A_{ij}^{\alpha\alpha}, \overline{B}_{ij} = \left(1 - \frac{2}{n_g}\right) B_{ij}^{\alpha\alpha}, \overline{D}_{ij} = D_{ij}^{\alpha\alpha} \quad (3.3.2-1)$$

where the overbar denotes the average material or fabric values for the extensional, bending/stretching coupling, and bending stiffness, respectively. These values are based on the superscripted $\alpha\alpha$ values computed for the equivalent cross-ply laminate. The correction factor $[1-(2/n_g)]$ is included because the bending/stretching coupling terms for the warp and fill direction laminae have opposite signs. N_g is the number of geometrical repeats in the fabric structure, and is unity for the plain weave considered in this analysis.

A comparison may be made between the finite element model and the mosaic model for the prediction of the elastic constants for a plain weave textile composite. For purposes of comparison, the material is considered to be E-glass/epoxy (see Table 3.2.3b) with the geometry described in Table 3.2.3a. The values for the elastic constants computed from the mosaic model are given in the first column of Table 3.3.2a.

However, the finite element geometry discussed in Sections 3.1 and 3.2 contains large, but artificial, pockets of resin located above and below the yarns. These resin pockets are a consequence of the technique used to model the fabric geometry and do not necessarily appear in the actual material. Thus, to provide a valid comparison with the finite element results, the input geometry for the mosaic model is modified as in Figure 3.3.2b. This new geometry accounts for the resin rich zones directly by dividing each of the 0.025 in. layers into a two layer group containing a 0.0065 in. layer of resin and a 0.0185 in. layer of glass/epoxy. The location at which each of the two layers has been divided corresponds to the upper (1) and lower (2) surfaces of the yarns in Figure 3.3.2b. The results for this modified material system are given in the second column of Table 3.3.2a.

Rather than applying a displacement to the finite element model and computing the load, a unit load is applied and displacements are computed. These displacements and the pertinent geometric parameters are

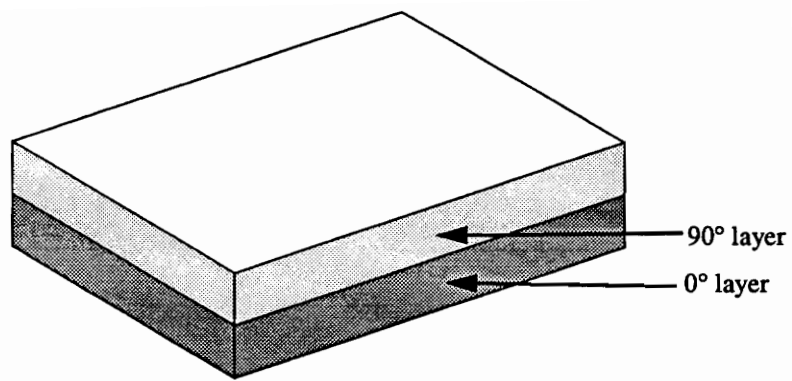


Figure 3.3.2a. Geometrical idealization of the mosaic model.

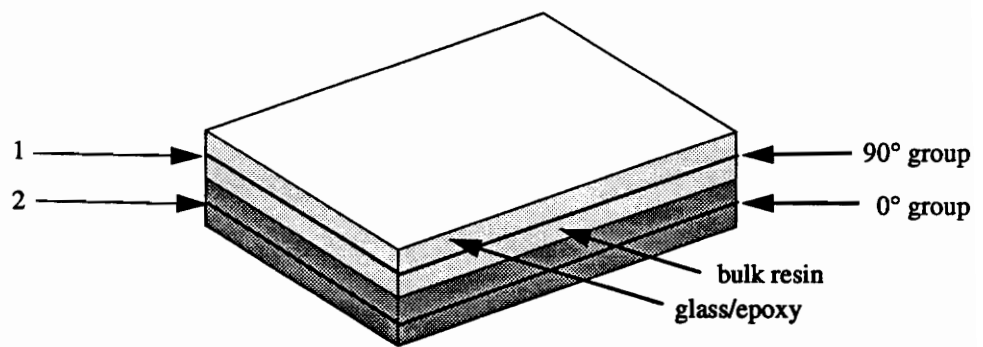


Figure 3.3.2b. Modified geometrical idealization of the mosaic model.

used to compute a nominal strain and the resulting elastic constants. The values obtained for the equivalent material elastic constants are given in the third column of Table 3.3.2a. Again, 1 and 3 are the in-plane axial and in-plane transverse directions, respectively. It should be noted that a value for ν_{31} of 0.1504 was obtained from the same boundary conditions that produced the reported value of E_3 and further that this value of ν_{31} is exactly the value obtained from the reciprocal relation for an orthotropic material

$$\frac{\nu_{ij}}{E_i} = \frac{\nu_{ji}}{E_j} \quad (3.3.2-2)$$

As mentioned previously, Table 3.3.2a contains the predicted moduli obtained from the mosaic model with and without a correction for the additional resin rich region and that of the corresponding finite element model. Note that even the stiffness values obtained from the mosaic model for a modified material are considerably larger than those predicted by the finite element model for a similar material. As described previously, this discrepancy is accounted for by noting that the mosaic model reduces the textile to the limiting case of a 90°/0° laminate.

3.3.3 Satisfaction of Global Equilibrium

Another check on the validity of the finite element model is to verify that global equilibrium has been satisfied. One approach is to manually integrate the component of the normal stress on the face of the model's exterior elements that corresponds to the loading direction over the area of the face and compare it to the applied load. For global equilibrium to be satisfied, their magnitudes must be equal. A somewhat simpler approach is to allow ABAQUS to perform the integration, i.e. examine the reaction forces at the nodes corresponding to the face opposite the application of the load. By summing the contributions in the direction of the applied load from each of the nodes on the face, it is possible to verify that equilibrium has been satisfied. This latter approach has been used to verify that global force equilibrium is satisfied.

3.3.4 Verification Using Results Obtained by Experimentation

Since experimental data is available for a similar glass/epoxy plain weave [108.], the predicted elastic moduli from the finite element analysis and the known elastic moduli obtained through experimentation may

be compared. As with the comparison with the mosaic models discussed in Section 3.3.2, a modification must be made to the quantities being compared. In this case, the fiber volume fraction of the material that was tested and the fiber volume fraction of the material in the finite element model are not the same. Again, the limitations on finite element model size necessitated that an artificially low fiber volume fraction be used.

The fiber volume fraction of the tested plain weave fabric composite material is known to be 30.5% as determined by acid digestion of the fabric composite, while the fiber volume fraction that was modeled was 15.0% (29.85% yarn volume fraction * 50% fiber volume fraction within the yarn). Thus, the tested material contained 2.033 times more fiber than the modeled material.

The finite element model was used to predict axial modulus by noting that the nominal axial strain is given by

$$\epsilon = \frac{\Delta L}{L} \quad (3.3.4-1)$$

where ΔL is simply the total axial displacement over the model of length L , and that the nominal axial stress is given by

$$\sigma = \frac{F}{A} \quad (3.3.4-2)$$

where F is the applied force acting on an area normal to the direction of its application, A . Thus, the axial modulus is given by

$$E = \frac{FL}{A\Delta L} \quad (3.3.4-3)$$

with the resultant of all other forces being zero.

Using this simple calculation, the values in column two of Table 3.3.3a are generated for the computed axial modulus. When these values are normalized for the difference in fiber volume fraction, a very good agreement with the experimentally determined values is observed.

Table 3.3.3a. Stiffness comparison between experimentation and the finite element model.

Property	Experiment	FEA	FEA Adjusted
E _x (E6 psi)	2.77	1.411	2.869

4.0 Finite Element Results for a Plain Weave

Included in this chapter is a discussion of some of the results obtained from the models discussed in Chapter 3. For both thermal and mechanical loading, a discussion of the specific details of the modeling of the plain weave is given followed by displacement and strain energy results for a variety of displacement boundary conditions. Except where noted, all results are given for a carbon/epoxy material system.

Because of the complexity of the isosurfaces [109.] that are presented throughout this chapter, it is useful to discuss a contrived example wherein many of the complexities in geometry and response may be eliminated. Although Figure 4.0a is without physical basis, it may be used as an aid to understand the isosurfaces that are the basis for the discussion throughout this chapter.

In Figure 4.0a sections 1 through 11 are the surfaces (sections in this simplified 2D case) of constant axial displacement within the domain. In this case, every successive isosurface corresponds to an increase in axial displacement of 10% of the total displacement. Thus, isosurface (1) is used to represent U_x at a restrained end, i.e. 0% of the total displacement, while isosurface (11) is used to represent U_x at the end being displaced, i.e. 100% of the displacement. Isosurface (6) corresponds to U_x at the center of this geometry. Since the axial strain in a particular region of the model can be considered as $\Delta L/L$, it is possible to make inferences as to the gross strain distribution within the representative volume element (RVE). This discussion will proceed by way of comparison of the “response” of several sections within the model. For example, through the section between isosurface (1) and (2), the change in displacement corresponds to 10% of full scale. The section between isosurface (5) and (6) is also subjected to a displacement corresponding to 10% of full scale,

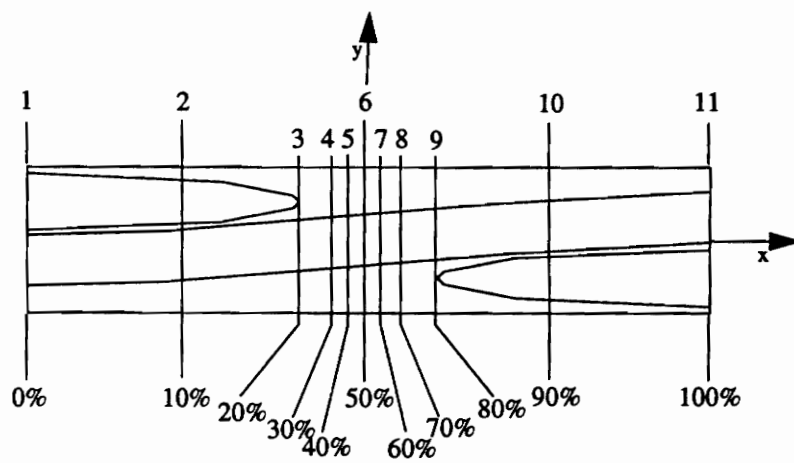


Figure 4.0a. Example for the interpretation of isosurfaces.

however, in this section the corresponding axial strain is much larger since the increased displacement is developed through a much shorter distance.

4.1 Thermal Loading

In addition to mechanical loading (to be discussed later), complete analysis of any structural material requires that thermal loading be considered. Textile composites may be subjected to thermal loads both during the curing process and during in-service temperature changes.

A uniform temperature change is considered because it is a fundamental case when considering the structural behavior of a material under thermal loading. Typically, textile preforms are layered and are many RVEs wide, thus it is appropriate to consider that a randomly selected RVE may be subjected to virtually any degree of constraint. This becomes important when accounting for the relative position of a RVE within a textile preform. To bound the limits of constraint, five boundary conditions are considered. These are: 1) periodic, 2) out-of-plane symmetry, 3) out-of-plane free, 4) in-plane symmetry, and 5) in-plane free boundary conditions.

The first of these boundary conditions, periodic, represents the upper bound of constraint, a RVE far from any boundary. To simulate this situation, the opposing faces are restrained with multi-point constraints (MPC) to remain uniformly straight and parallel to one another. The second, out-of-plane symmetry, is an intermediate case similar to the behavior of a two layer un-nested textile. Out-of-plane free boundary conditions are representative of the least constrained RVE, that is, a composite that is one RVE thick. While the out-of-plane symmetry case has one free face, the out-of-plane free case has both top and bottom surfaces free to deform from their original planar state.

Of the two in-plane variations, the in-plane symmetry case is an intermediate degree of constraint representing a narrow composite two RVEs wide. The final case, in-plane free, is the lower bound of restraint, a composite one RVE wide. In this last case, the material is assumed to have two edges that are allowed to deform freely.

In all cases, a uniform temperature change of one degree Fahrenheit is applied to each element within the

finite element model. Although this represents the steady state loading condition, geometric complexities and material dissimilarities are sufficient to induce the complex behavior shown in the upcoming sections of this chapter.

The results that follow are based upon the finite element models discussed in the preceding chapter. The results are divided into two main sections: 1) displacements, and 2) strain energy density. The later quantity is discussed because it is the basis of many energy based failure criteria and also provides a useful scalar quantity for visualization independent of material coordinate system. This invariance to rotation into a particular coordinate system is the primary advantage of visualizing strain energy rather than presenting the individual strain or stress components. Similarly, in an upcoming chapter, Chapter 6, the discussion is focused on a scalar failure surface for a given failure mode rather than the stress components that contribute to the failure.

Note that familiar terms are used in describing the geometry of the RVE. For example, “lower” and “upper” refer to the surface having most negative y coordinate ($y = -0.025$ in.) and the most positive y coordinate ($y = +0.025$ in.), respectively. Also, numbers in parenthesis correspond to a specific detail on the figure being discussed.

The models have been checked for convergence, and for the idealized geometries considered, are converged to within a few percent. However, in the figures that follow, it may be more beneficial to consider the qualitative nature of the isosurfaces than it is to compare exact numbers represented by the isosurfaces.

4.1.1 Displacement Results

4.1.1.1 Periodic Boundary Conditions

The isosurfaces illustrated in Figure 4.1.1.1a¹ represent the computed internal axial displacements of a well restrained region within plain weave textile composite under a uniform temperature change. As prescribed by the boundary conditions, the exterior boundaries remain planar and parallel. Displacements within this RVE are, as expected, the most uniform. Although not planar, every point on the surface (1) is

1. See Appendix B: Figures from Chapter 4

12.5% of the maximum value. It can be thought of as representing the average axial strain in that part of the model. Thus, the axial yarn is seen to strain more than the transverse yarn that is just above it in the RVE. Further, recalling elementary elasticity, the angular change in the displacement isosurface (1) can be compared directly to a local shear strain. The sharper the angle, the greater the shear strain. This “shear strain” is seen in both the x - y and x - z planes.

Figure 4.1.1.1b represents the out-of-plane deformation associated with periodic boundary conditions. Note that the maximum value of out-of-plane displacement is 83% larger than the corresponding in-plane displacement for these boundary conditions. This occurs for two reasons: 1) the coefficient of thermal expansion (CTE) of the yarn’s transverse direction is much greater than the CTE in the yarn axial direction, and 2) the in-plane stiffness of the axial and transverse yarns restrains the in-plane deformation.

As with the in-plane deformation for this fully restrained case, the top and bottom boundaries are forced to remain straight and parallel from the applied boundary conditions. However, internally, the deformations are as shown (1).

Figure 4.1.1.1c is the baseline of transverse displacement (fully constrained) for the RVE models. Again, the outer boundaries are allowed to deform in a planar fashion only. Although the temperature change is uniform in the x and z directions, as indicated in Table 3.2.3a, the RVE geometry is not uniform. Thus it is reasonable to expect that the internal deformation behavior is not uniform in the two in-plane directions.

4.1.1.2 Out-of-Plane Boundary Conditions

When the upper surface of the RVE is released to deform out-of-plane, the reduced constraint results in the axial deformation shown in Figure 4.1.1.2a. This case is representative of a layer of a two layer un-nested composite and provides an intermediate condition to the fully restrained case shown in Figures 4.1.1.1, and the unconstrained case that will be seen as Figures 4.1.1.3. Note here that the lower portion of isosurface (1) shows a similar deformation as the lower portion of isosurface (1) in Figure 4.1.1.1a, whereas the free condition on the top surface localizes the axial deformation to the region between the transverse yarns. As before, the local strains associated with isosurface (1) can be visualized as the ratio of the value of displacement represented by the isosurface (12.5% of $U_{x,max}$) to the distance from the isosurface to the left side boundary.

Thus, a disproportionate percentage of the axial deformation occurs in the most axially compliant region of the RVE (2).

Out-of-plane deformations, Figure 4.1.1.2b, are “dish” shaped. Now, the restraint on out-of-plane deformation is relaxed, and the upper surface is allowed to deform freely. Note the isosurface shown is at 50% (1), while the bottom surface is the fixed, or 0%, surface. This surface is concave, and the maximum displacement occurs above the point of maximum concavity. For clarity, isosurfaces other than the one at 50% have been omitted from the plot; however, it is important to note that the maximum value of displacement occurs along a surface that is a function of the local weave geometry.

By further decreasing the constraint on the model to allow for both top and bottom surfaces to freely deform, a situation as shown in Figure 4.1.1.2c results. In the regions of maximum constraint (those regions near the yarns), the axial displacement isosurfaces (1) are similar to those in the fully restrained case (Figure 4.1.1.1a). However, differences are greatest in the more compliant regions away from the yarns. Here, the angular change in isosurface and resulting shear strains are reduced because of the absence of the planar constraint.

An interesting artifact in Figure 4.1.1.2d is (1), the isosurface of 50% of the maximum out-of-plane displacement. Because of the angle from which this image was taken, it appears that considerable out-of-plane deformation occurs at (1), while little occurs at (2). Actually, because of the anti-symmetric geometry, the two regions of the displacement are anti-symmetric. Because of the absence of in-plane constraint, the maximum deformation is 47% larger than for a similar layer embedded within the composite (Figure 4.1.1.1b). Thus, it is possible to conclude that there is a non-uniform displacement gradient not only within the individual RVEs (Figure 4.1.1.2d), but among the several RVEs through the thickness of a typical textile composite, and that it is a function of their position from the center-line of the composite.

4.1.1.3 In-Plane Boundary Conditions

To simulate a free edge, the front boundary of the RVE has been un-constrained in Figure 4.1.1.3a to allow free deformation. Note that the axial deformation along the back, or constrained, surface (1) is similar to the axial deformation in the same region for the fully constrained case. However, a very different condition

exists at the free edge. A disproportionately large percentage of the total axial deformation occurs near the compliant center of the front edge (2). Further, increased shear strains develop. For example, the x - y component of shear strain, shown as an angular change in the isosurface, is prominent along the front edge (3).

Figure 4.1.1.3b illustrates the transverse deformation, in particular, the transverse deformation along the free edge. Nominally, only slightly more than 25% of the total deformation in the RVE occurs in the back half (1) of the RVE. Also, the greatest transverse deformation occurs near the center of the RVE. This is the least constrained (transverse) region of the model both because of the domination of the region by axial yarns and by its distance from the stiffening effects of the restraints along the transverse edges (2).

When both the front and back edges of the RVE are released, simulating a composite one RVE wide, the axial deformation is as shown in Figure 4.1.1.3c. The internal deformation is redistributed such that the axial strain varies greatly with position from the x -axis (1). Further, the center of the RVE, the matrix dominated region, is found to be in a state of near constant displacement (2).

Corresponding transverse displacements are shown in Figure 4.1.1.3d. Similar to the transverse displacements shown in Figure 4.1.1.3b, the compliant region away from the front/back edge boundary conditions and the transverse yarns, has the greatest transverse displacement. The combined constraining effect of planar edges and transverse yarns is similar to the thermal expansion case for a plate with cantilevered edges. The center is allowed to displace from the nominal centerline of the edge, however, the displacement is not as large as if the edges were allowed to rotate freely.

The largest transverse displacement is 50% larger than for the case of one free edge and over 400% larger than for the fully constrained case. A comparison can be made with the free edge case for laminated composites where the edge displacements are seen to vary as a function of through thickness (y) coordinate along the edge. In contrast to the laminate, the transverse displacements for the textile are also greatly dependent on axial coordinate (1).

4.1.2 Strain Energy Density Results

Strain energy density (SED) results for the case of periodic boundary conditions are shown in Figure 4.1.2a. The SED distributions in this model correspond to the displacement distributions shown in Figures

4.1.1.1 discussed previously. The left and right hand regions shown in (1) are similar. In the figure, the two regions of the isosurface are anti-symmetric as a function of the yarn geometry.

Note that the yarns contain much of the SED in the model (1), while the largest values of SED are found in the regions of the matrix immediately above and below the axial/transverse yarn crossovers (2). Because this architecture is not quite balanced, the maximum values occur at the alternate corners on the top and bottom of the model (3). Checking the stresses and strains in the several regions of interest indicates that a matrix failure primarily due to through-thickness tension at region (3) is the likely first failure.

The centerline paths of the axial yarns are not fully antisymmetric for this geometry. An important result of this geometric artifact is that the distance from the axial yarn outer surface to the horizontal boundary of the RVE is different for adjacent pairs of interstices. Thus, of the eight corner locations in the RVE, there are two pair of four distinct values of SED. A typical pair is shown in (4).

Since SED is a scalar product of strain and stress components in the model, it is always zero or positive for conservative systems. As shown in Figure 4.1.2a, it is greater than zero for all locations within the model and reaches a maximum of $6.68\text{E-}4$ in-lb/in³ in regions (3).

When the out-of-plane restraints are removed from the top and bottom surfaces, the strain energy distribution is shown in Figure 4.1.2b. This figure corresponds to the displacements shown in Figures 4.1.1.2 that have been discussed previously. Large values of SED are found in the corners of the matrix similar to the fully restrained case (1). However, the largest values of SED in the model are found in alternate inboard locations (2) and (3) and result primarily from the combined effect of through-thickness and axial tension. Thus, while the material exhibiting the maximum SED has not changed, the location has been altered significantly.

When the in-plane restraints are removed from the front and back surfaces, the strain energy distribution is similar to that in Figure 4.1.2c and corresponds to the displacements in Figures 4.1.1.3. The largest values of SED are very localized such that the interior major elliptic axis regions of the transverse yarns contain all the SED above 30% of the maximum (1). The maximum value of SED is increased by 165% over the fully restrained case. The likely mode initial failure is transverse tension in the transverse and axial yarns.

In contrast to the mode and location shown in Figure 4.1.2a for a carbon/epoxy system, if the material parameters are changed to simulate glass/epoxy, strain energy density values such as those in Figure 4.1.2d result. The yarns contain all of the SED above 40% of the maximum value. However, in the glass/epoxy material system, the thermal and mechanical mismatches are not as severe as with carbon/epoxy. The largest values of SED are found near the centerline of the yarns (2) and are primarily the result of axial loads in the local coordinate systems.

4.2. Mechanical Loading

A uniform axial extension is the fundamental case when studying the behavior of a material under mechanical loading and will be discussed here. For this load case, the positive x -face is displaced uniformly by a displacement producing a nominal strain of 1000 micro-strain (0.00275 in. applied axial displacement through 0.275 in.), the negative x -face is restrained from displacement in the axial direction, and the other faces are subjected to restraints simulating extremes of position within the overall structure. As with the case of thermal loading, the following limiting cases are considered: 1) periodic, 2) out-of-plane symmetry, 3) out-of-plane free, 4) in-plane symmetry, and 5) in-plane free boundary conditions.

4.2.1 Displacement Results

4.2.1.1 Periodic Boundary Conditions

The isosurfaces shown in Figure 4.2.1.1a represent the computed internal axial displacement of a well constrained region within the plain weave textile composite under uniform axial extension. As with Figure 4.1.1.1a (uniform temperature change), the exterior boundaries remain planar and parallel. Unlike the case of uniform temperature change, the isosurfaces are representative of a near uniform axial displacement gradient (1). Since the axial yarns dominate the axial stiffness of the material, it is evident that, for this case, a state of near planar axial deformation exists.

Out-of-plane deformation of the textile is illustrated in Figure 4.2.1.1b. The magnitude of the maximum value of this displacement component is approximately 1% of the applied axial value. The length to thick-

ness ratio of the model is 5.5:1, producing an average through-thickness Poisson's ratio of $\nu=0.05$. The isosurface shown is at 50%, and once again, the internal displacements are a function of the local yarn geometry (1). In particular, note that since every point on the isosurface has the same displacement, the regions dominated by the transverse yarns show a greater through-thickness contraction than the regions dominated by axial yarns. This, however, is a local effect, and due to the periodic boundary conditions, must sum to the same through-thickness (y) contraction at every x - z location in the model.

The large non-planar character of the transverse displacements shown in Figure 4.2.1.1c indicates that the transverse strain in the yarns' fiber direction (near the edges of the RVE) is much less than the strain in the yarn transverse direction (1). Once again, the summation of all of these local phenomenon must equal a common value along the restrained edges for this particular set of boundary conditions.

4.2.1.2 Out-of-Plane Boundary Conditions

When the upper surface of the RVE is released to deform out of plane, the axial deformation shown in Figure 4.2.1.2a results. Unlike what is seen in Figure 4.1.1.2a, there is little effect of lack of out-of-plane constraint on the distribution of axial displacement in the model under axial loading (Figure 4.2.1.2a). The only differences are minor and are located near the matrix rich center of the RVE (1).

Out-of-plane deformations are, once again, "dish" shaped and localized (1) as seen in Figure 4.2.1.2b. The maximum U_y displacement occurs at (2). This maximum U_y is 69% larger than the corresponding displacement for the fully restrained case. Unlike the corresponding thermal load case, where thermal load is induced in all directions resulting in a somewhat uniform concave surface (Figure 4.1.1.2b), the isosurface in Figure 4.2.1.2b is preferential to the axial direction.

When the planar constraint is eliminated completely from the model to simulate a material one RVE thick, the axial displacement isosurfaces appear as in Figure 4.2.1.2c. Unlike the more restrained cases, the free-free case has very non-planar isosurfaces of axial displacement indicating that the strain distribution within the model has been significantly altered as a function of weave geometry. Further greatly increased shear strains (1) result. These isosurfaces are somewhat similar to those shown for ΔT in Figure 4.1.1.2c.

The corresponding isosurfaces of out-of-plane displacement are given in Figure 4.2.1.2d. The maximum U_y is 2400% larger than for the fully restrained case and is very irregular. Here, (1) is at the maximum U_y while (2) is the minimum for the entire model. The shape of (3), the 50% surface, further illustrates the extreme gradient of displacements in this model. If, for example, this surface is considered the neutral surface, then displacements on either side can be considered to be of opposite sense. While the in-plane requirement for the top and/or bottom surface prevented the large U_y in the constrained models with axial loading, and the force in the transverse yarn counterbalanced much of the force in the axial yarns in the case of thermal loading, no such situation exists in this particular case.

4.2.1.3 In-Plane Boundary Conditions

Unlike the case of uniform temperature change, a free edge in an axially loaded RVE has little effect on the axial displacement. This is seen in Figure 4.2.1.3a.

The transverse deformation for the one edge free case is illustrated in Figure 4.2.1.3b. The isosurface (1) is the region of maximum transverse displacement (dimpling at the edge). Unlike a laminated material, this dimpling is a function of both the local x - and y -coordinate. Of course, the details are a function of the location of the free edge within the RVE. If, for example, the bounding surface were at the midplane of this RVE ($z=0$) the local deformation and strain energy states would likely be very different.

The axial displacement for the limiting case of a structure one RVE wide (both front and back edges released) is shown in Figure 4.2.1.3c. Even with no transverse constraint beyond the boundaries of the representative volume element, and unlike the thermally loaded case, there is little dependence on the transverse (z) coordinate.

The isosurfaces of transverse displacement are shown in Figure 4.2.1.3d. Similar to what is shown in Figure 4.2.1.3b, the transversely compliant region near the center of the RVE has the greatest transverse displacement. The maximum transverse displacement is 500% larger than in the fully restrained case. Once again the x - y dependence is seen, as are angular changes representative of large shear strains (1).

4.2.2 Strain Energy Density Results

Strain energy density (SED) results for the case of periodic boundary conditions and axial loading are shown in Figure 4.2.2a. The yarns contain all of the SED in the model above 2.5 in-lb/in^3 . Unlike the case of uniform thermal expansion, the product of axial stress and axial strain dominates the strain energy behavior of the material. The maximum value of SED is 11.2 in-lb/in^3 and occurs at the axial yarn centerline between the two constraining transverse yarns. Also, since the transverse yarns are considerably stiffer and take more load than the matrix, the SED in the axial yarns is slightly reduced at the regions of transverse yarn cross-over. Although the strain energy is largest in the axial yarns due to the product of the axial components of stress and strain, a comparison of the magnitudes of the several components of stress with their respective allowables indicates that transverse tension in the transverse yarns is the likely mode for first failure and that the failure of fibers in the axial yarns is a secondary event.

Removal of the out-of-plane constraints produces a SED distribution as shown in Figure 4.2.2b. Again the axial yarns dominate the energy distribution in the model; however, both the magnitude and location of the maximum values have changed (1). The maximum value is now 7.2 in-lb/in^3 and is a combined result of axial tension and, recalling the displacements in Figure 4.2.1.2d, local bending.

If both in-plane restraints are removed, a strain energy density distribution similar to that in Figure 4.2.2c results. The yarns are once again seen to contain most of the SED. Now the distribution of the maximum values of SED is uniform along the centerline of the axial yarns and little effect of the transverse yarns is noted. The maximum value is 10.6 in-lb/in^3 . Comparing this value to that for the fully restrained case (11.2 in-lb/in^3) indicates that transverse constraint contributes only slightly to the maximum value of SED in this material under axial load.

4.3 Summary of Results and Discussion for a Plain Weave

Included in Table 4.3a and Table 4.3b are the maximum values of the three displacement components and the strain energy density that are shown in the figures corresponding to this chapter. It is useful at this point, to summarize the various results that have been discussed in the analysis of this plain weave. The two paragraphs that follow are brief summaries of the observations made from the finite element results for both thermal and mechanical loading.

Several noteworthy items have been discussed concerning the response of the plain weave under thermal loading, including:

- The response of even simple textile composites such as plain weaves is fully three-dimensional as shown in the figures in this chapter,
- Stacking of layers restrains in-plane deformation of the weave,
- Severe dimpling is characteristic of an (unrestrained) single layer,
- Free edge localizes axial/transverse displacement between the transverse yarns,
- Low levels of strain energy for ΔT show similar distribution as for a mechanical load,
- Maximum strain energy for fully restrained carbon/epoxy is located in the corners and is dependent on the corner geometry,
- Decreased mechanical mismatch in glass/epoxy changes the location of the maximum strain energy to the transverse yarns (fully restrained case),
- Removing the out-of-plane restraint induces the greatest strain energy away from the corners, and
- The free edge condition redistributes strain energy into transverse yarns.

Additional noteworthy items have been discussed concerning the response of the plain weave under mechanical (axial) loading, including:

- Although axial deformation can be reasonably approximated as two-dimensional, transverse and through-thickness deformation can not,
- Unlike the case of thermal loading, axial deformation is not significantly altered by width effects,
- The effect of the absence of an out-of-plane constraint is very significant in both deformation and strain energy response,
- The free edge effect is very significant and is a function of both x - and y -coordinate,
- Maximum strain energy is always found in the axial yarns and is altered as a function of the RVE's location within the overall material, and
- RVE's with little through-thickness constraint are subject to considerable local bending.

Table 4.3a. Maximum values for quantities from thermal loading.

Boundary Condition	U_x (in/F)	U_y (in/F)	U_z (in/F)	SED (in-lb/in ³ /F)
Periodic	8.89E-7	16.3E-7	9.19E-7	6.68E-4
Free Top	9.08E-7	21.2E-7	x	x
Free Top / Bottom	9.92E-7	23.9E-7	x	5.06E-4
Free Front	11.5E-7	x	31.6E-7	x
Free Front / Back	10.2E-7	x	47.3E-7	17.9E-4

x- not discussed

Table 4.3b. Maximum values for quantities from mechanical loading.

Boundary Condition	U_x (in)	U_y (in)	U_z (in)	SED (in-lb/in ³)
Periodic	0.00275	-2.56E-5	-1.31E-5	11.2
Free Top	0.00275	-4.33E-5	x	x
Free Top / Bottom	0.00275	-61.2E-5	x	7.2
Free Front	0.00275	x	-4.40E-5	x
Free Front / Back	0.00275	x	-6.60E-5	10.6

x- not discussed

5.0 Progressive Failure Model Development and Verification

Included in the first section of this chapter is a discussion of several of the failure theories used for both isotropic and orthotropic materials and the selection and justification of the failure theories chosen for the present study. In the second section is a discussion of the details of a progressive failure model suitable for the study of the failure of textile based composites. Included in the final section is a discussion of the procedure used to verify the failure algorithm.

5.1 Failure Criteria

The model that has been developed for the interrogation of textile based composite materials divides the domain of the textile into two distinct subdomains or phases, that of a homogeneous isotropic resin and that of a homogeneous transversely isotropic impregnated yarn. Since the composite is considered to be composed of two materials, each with different degrees of anisotropy, it follows that a different failure criterion may be appropriate for each phase.

5.1.1 Failure Criteria for Isotropic Materials

Isotropic materials such as iron, steel, and aluminum have been used for structural applications for centuries. For example, malleable iron was commonly used in bridge construction by the early 1840's [110.]. The mechanics of failure of these materials has been studied for most of the 20th century and as such, many fail-

ure criteria for isotropic materials exist in the literature. Several of the more commonly used criteria are discussed throughout Section 5.1.1.

5.1.1.1 Maximum Stress Criterion

There are two forms of the maximum stress criterion, the first is in terms of the stress components, while the second is in terms of the principal stresses. The first of these forms is postulated such that failure occurs once any of the stress components reaches the corresponding failure stress for the material. For materials with different failure stresses in tension and compression, the criterion is [18.]:

$$\begin{aligned}
 &\sigma_x < X_t & |\tau_{xy}| < S \\
 &\sigma_y < X_t & |\tau_{xz}| < S & , \sigma_i > 0 \\
 &\sigma_z < X_t & |\tau_{yz}| < S \\
 \text{and} & & & (5.1.1.1-1) \\
 &\sigma_x > X_c \\
 &\sigma_y > X_c & , \sigma_i < 0. \\
 &\sigma_z > X_c
 \end{aligned}$$

Note that there is no interaction between the components of stress so that for a three-dimensional state of stress in a material with different allowables in tension and compression, there are actually nine separate conditions that must be checked. An obvious advantage of this criterion is that the particular mode corresponding to failure is readily identifiable. However, since the criterion does not allow for interaction of the components of the stress tensor, predictions made with the maximum stress criterion can be in considerable error.

The second form of the maximum stress criterion is postulated such that failure occurs when one of the principal stresses reaches the failure stress in uniaxial tension [111.]. For materials with different strengths in tension and compression, the criterion is:

$$\begin{aligned}
 \max\{\sigma_i\} &= X_t, i=1,2,3 & , \sigma_i > 0 \\
 \min\{\sigma_i\} &= X_c, i=1,2,3 & , \sigma_i < 0
 \end{aligned}
 \tag{5.1.1.1-2}$$

where the subscripts 1, 2, 3 refer to the principal stresses. These criteria are somewhat applicable to materials that exhibit little plastic deformation before failure.

5.1.1.2 Maximum Strain Criterion

The maximum strain criterion is analogous to the maximum stress criterion, except that the strains corresponding to strain at failure are the limiting case. Again there are two forms that are given in terms of the strain components and the principal strains. The material is said to have failed once any of the strain components reaches the corresponding failure strain for the material. For materials with different failure strains in tension and compression, the criterion is [18.]:

$$\begin{aligned}
 &\epsilon_x < X_{et} & |\gamma_{xy}| < S_e \\
 &\epsilon_y < X_{et} & |\gamma_{xz}| < S_e & , \epsilon_i > 0 \\
 &\epsilon_z < X_{et} & |\gamma_{yz}| < S_e \\
 \text{and} & & & (5.1.1.2-1) \\
 &\epsilon_x > X_{ec} \\
 &\epsilon_y > X_{ec} & , \epsilon_i < 0. \\
 &\epsilon_z > X_{ec}
 \end{aligned}$$

As with the stress components, that there is no interaction between the components of strain so that for a three-dimensional state of strain in a material with different allowables in tension and compression, again there are nine separate conditions that must be considered.

The second form of the maximum strain criterion is postulated such that failure occurs when one of the principal strains reaches the failure strain in uniaxial tension. For materials with different allowables in tension and compression, the criterion is:

$$\begin{aligned}
 \max\{\epsilon_i\} &= X_{et}, i=1,2,3 & , \epsilon_i > 0 \\
 \min\{\epsilon_i\} &= X_{ec}, i=1,2,3 & , \epsilon_i < 0
 \end{aligned}
 \tag{5.1.1.2-2}$$

where the subscripts 1, 2, 3 refer to the principal strains. As with the maximum stress criterion, the maximum strain criterion is most applicable to brittle materials.

5.1.1.3 Maximum Shear Stress (Tresca) Criterion

The maximum shear stress criterion is postulated so that failure occurs in a material subjected to combined stresses when the maximum shear stress equals the shear stress at failure of the same material subjected to uniaxial tension [111.]. Failure is noted when any of the following equalities is reached:

$$\begin{aligned} |\sigma_1 - \sigma_2| &= S \\ |\sigma_2 - \sigma_3| &= S \\ |\sigma_3 - \sigma_1| &= S \end{aligned} \tag{5.1.1.3-1}$$

where σ_i are the principal stresses, and S is the shear allowable stress in uniaxial tension. This criterion is commonly used to predict yielding in ductile materials.

5.1.1.4 Maximum Distortion Energy (von Mises) Criterion

Failure is predicted from the maximum distortion energy criterion when the component of the strain energy from distortion (shear) reaches the energy corresponding to failure in uniaxial tension. Thus, in terms of the principal stresses, the criterion takes the form:

$$\sqrt{\frac{1}{2} \{ (\sigma_1 - \sigma_2)^2 + (\sigma_2 - \sigma_3)^2 + (\sigma_3 - \sigma_1)^2 \}} = X \tag{5.1.1.4-1}$$

where X is the failure stress of the material as determined by uniaxial tension tests. The maximum distortion energy criterion is commonly used to predict the onset of yielding in ductile materials.

5.1.2 Failure Criteria for Transversely Isotropic (or Orthotropic) Materials

As with the failure criteria for isotropic materials, many criteria exist for the failure of orthotropic materials. Several of the more prominent theories are discussed in the following section.

5.1.2.1 Maximum Stress Criterion

The maximum stress criterion for orthotropic materials is essentially the same as the first form of the criterion for isotropic materials discussed in section 5.1.1.1 and is restated here for convenience. From [18.]:

$$\begin{aligned}
 &\sigma_x < X_t & |\tau_{xy}| < S_{xy} \\
 &\sigma_y < Y_t & |\tau_{xz}| < S_{xz} & , \sigma_i > 0 \\
 &\sigma_z < Z_t & |\tau_{yz}| < S_{yz} \\
 \text{and} & & & (5.1.2.1-1) \\
 &\sigma_x > X_c \\
 &\sigma_y > Y_c & , \sigma_i < 0. \\
 &\sigma_z > Z_c
 \end{aligned}$$

If any of these conditions is violated, then the material is assumed to have failed. Note, however, that in the form for orthotropic materials, there may be a different failure stress for each of the tensile, compressive, and shear failure modes.

5.1.2.2 Maximum Strain Criterion

As with the maximum stress criterion, the maximum strain criterion for orthotropic materials is essentially the same as the first form of the criterion for isotropic materials discussed in Section 5.1.1.2 and is restated here for convenience. From [18.]:

$$\begin{aligned}
 &\epsilon_x < X_{\epsilon t} & |\gamma_{xy}| < S_{xy\epsilon} \\
 &\epsilon_y < Y_{\epsilon t} & |\gamma_{xz}| < S_{xz\epsilon} & , \epsilon_i > 0 \\
 &\epsilon_z < Z_{\epsilon t} & |\gamma_{yz}| < S_{yz\epsilon} \\
 \text{and} & & & (5.1.2.2-1) \\
 &\epsilon_x > X_{\epsilon c} \\
 &\epsilon_y > Y_{\epsilon c} & , \epsilon_i < 0. \\
 &\epsilon_z > Z_{\epsilon c}
 \end{aligned}$$

Again, the failure strain may be different, not only in tension and compression, but also for each of the material directions. Since there is coupling between the components of normal stress as a function of the material Poisson's ratio, it is possible that, depending on the particular stress components involved, different failure loads and modes will be predicted by the maximum stress and maximum strain criteria [100.].

5.1.2.3 Tsai-Hill Criterion

Unlike the independent modes of the maximum stress criterion, the Tsai-Hill failure criterion is a smooth surface in terms of the in-plane failure stresses:

$$\frac{(\cos \theta)^4}{X^2} + \left(\frac{1}{S^2} - \frac{1}{X^2} \right) (\cos \theta)^2 (\sin \theta)^2 + \frac{(\sin \theta)^4}{Y^2} = \frac{1}{\sigma_x^2} \quad (5.1.2.3-1)$$

where θ is the orientation of the lamina to the loading direction, X , Y , and S are the normal and shear failure stresses, and σ_x is the applied stress. This criterion was shown to give considerably better results than the maximum stress or maximum strain criteria for orthotropic materials since it accounts for interaction between the failure stresses X , Y , and S , whereas the maximum stress and maximum strain criteria do not [18.].

5.1.2.4 Tsai-Wu Criterion

An improvement on the Tsai-Hill criterion, the Tsai-Wu criterion includes additional terms to provide a better curve fit of the experimental data. For an orthotropic lamina in the principal material directions under plane stress, the Tsai-Wu criterion is given as [18.]:

$$F_1 \sigma_1 + F_2 \sigma_2 + F_6 \sigma_6 + F_{11} \sigma_1^2 + F_{22} \sigma_2^2 + F_{66} \sigma_6^2 + 2F_{12} \sigma_1 \sigma_2 = 1 \quad (5.1.2.4-1)$$

where σ_i are the components of the stress tensor and F_i and F_{ij} are the components of the "strength" tensor. The linear terms represent the strengths in tension and compression, the quadratic terms represent an ellipsoid in stress space, and the mixed 1-2 term allows for interaction between the in-plane normal stresses. The determination of F_{12} must be made through biaxial testing of the material and is both expensive and difficult

to measure. As with the Tsai-Hill criterion, this criterion is primarily a result of curve fitting experimental data. Further, it can not be used to distinguish between the different failure modes such as tensile failure of the fibers or transverse cracking of the matrix.

5.1.2.5 Hashin's Criterion

Hashin [66.] formulated a criterion that could be used to distinguish between fiber tensile and compressive modes in addition to the tensile and compressive modes in the matrix transverse to the fiber direction. This criterion is in the form of a piecewise smooth quadratic in terms of the stresses. The four separate modes are characterized as:

Tensile Fiber Mode, $\sigma_{11} > 0$

$$\left(\left(\frac{\sigma_{11}}{\sigma_A^P} \right)^2 + \frac{1}{\tau_A^2} (\sigma_{12}^2 + \sigma_{13}^2) \right) = 1 \quad (5.1.2.5-1)$$

Compressive Fiber Mode, $\sigma_{11} < 0$

$$\sigma_{11} = -\sigma_A^N \quad (5.1.2.5-2)$$

Tensile Matrix Mode, $\sigma_{22} + \sigma_{33} > 0$

$$\frac{1}{\sigma_T^{P2}} (\sigma_{22} + \sigma_{33})^2 + \frac{1}{\tau_T^2} (\sigma_{23}^2 - \sigma_{22}\sigma_{33}) + \frac{1}{\tau_A^2} (\sigma_{12}^2 + \sigma_{13}^2) = 1 \quad (5.1.2.5-3)$$

Compressive Matrix Mode, $\sigma_{22} + \sigma_{33} < 0$

$$\frac{1}{\sigma_T^N} \left[\left(\frac{\sigma_T^N}{2\tau_T} \right)^2 - 1 \right] (\sigma_{22} + \sigma_{33}) + \frac{1}{4\tau_T^2} (\sigma_{22} + \sigma_{33})^2 + \quad (5.1.2.5-4)$$

$$\frac{1}{\tau_T^2} (\sigma_{23}^2 - \sigma_{22}\sigma_{33}) + \frac{1}{\tau_A^2} (\sigma_{12}^2 + \sigma_{13}^2) = 1$$

where:

σ_A^P = tensile failure stress in fiber direction,

σ_A^N = absolute value of compressive failure stress in fiber direction,

σ_T^P = tensile failure stress transverse to fiber direction,

σ_T^N = absolute value of compressive failure stress transverse to fiber direction,

τ_T = transverse failure stress in shear, and

τ_A = axial failure stress in shear.

5.2 Progressive Failure Model

Textile based composites have been shown to exhibit considerable damage progression between the onset of failure and final failure when the material can no longer carry load [108.]. Thus, a model that predicts final failure at the onset of damage may be in considerable error. Typically, in the context of progressive failure modeling, this damage is modeled as a loss of stiffness at the offending locations in the model. Thus, the appropriate material properties are degraded locally while the assumption of linear elastic behavior is maintained. Although many methodologies for progressive failure of composite materials have been published in the literature [72.-104.], the progressive failure model that is discussed as part of the present study is patterned after the work of Tan [77.,78.].

5.2.1 Selection of Failure Criteria

Of the several failure criteria discussed in Section 5.1, the maximum stress criterion and Hashin's criterion have been chosen to model the isotropic matrix and the transversely isotropic yarns, respectively.

Although a yield criterion such as the maximum distortion energy criterion in conjunction with a plasticity model such as isotropic hardening or kinematic hardening are viable candidates for the analysis of the matrix material, the maximum stress criterion was chosen for three reasons. First, the matrix is assumed to be brittle and as such undergo negligible plastic deformation during failure. Second, the maximum strain criterion is much simpler and in conjunction with a simple material degradation model (to be discussed in an upcoming section) requires much less computer time than the plasticity models. This is a concern considering that the routine is accessed for every Gauss point in the model. Third, for the mechanical loading cases

that will be discussed in this text, it was found that failure occurs in the yarns rather than the matrix, so the choice of constitutive behavior for the matrix beyond initial failure is of little consequence.

Since mechanical loading tests of a glass/epoxy plain weave material [108.] have been used to show that the primary failure occurs within the yarns, it is of great importance that the failure model for the yarn material be as realistic as possible. Hashin's criterion was chosen because of the ability to predict not only the failure loads, but also the modes of failure within a composite material. Specific advantages of using this criterion in conjunction with the present analysis include:

- The criterion was developed for transversely isotropic laminae - a material that is very similar to the transversely isotropic yarns in a textile,
- The criterion was developed to allow for discrimination between tensile and compressive fiber and matrix failure modes,
- The criterion can be used to model these four primary failure modes separately - this allows for degradation of individual stiffness components as failure progresses,
- The criterion allows for both tensile and shear stresses to contribute to failure,
- The criterion is quadratic in stresses and provides a reasonable fit to failure data, and
- All of the failure parameters that are used in the criterion are easily obtainable from standard tests (except the ultimate transverse shear stress).

5.2.2 Damaged Material Formulation

The commonly used assumption that the elastic constants of the material are the same in tension and compression is made in this analysis. However, recognizing that the failure stress in tension and compression may differ significantly, the algorithm has been coded to include separate values of the tensile and compressive allowables.

5.2.2.1 Damaged Material Formulation - Matrix

The internal state variables that represent the damaged state of the material are given by D_{ij} , where a unique value of this stiffness degradation may be assigned for each constituent material and each component of stiffness. The D_{ij} can be thought of as the fraction of the original stiffness that is retained after damage has occurred. $D_{ij}=1$ represent an undamaged material, while $D_{ij}=0$ represent a completely degraded material. Thus, at a Gauss point of an element in the matrix that has been determined to contain damaged stiffness components, the potentially degraded constants are given as:

$$\begin{aligned}
E_{11}^m &= D_{11}^m E_{11}^{m0} & G_{12}^m &= D_{12}^m G_{12}^{m0} \\
E_{22}^m &= D_{22}^m E_{22}^{m0} & G_{13}^m &= D_{13}^m G_{13}^{m0} \\
E_{33}^m &= D_{33}^m E_{33}^{m0} & G_{23}^m &= D_{23}^m G_{23}^{m0}
\end{aligned} \tag{5.2.2.1-1}$$

where E_{11}^m , E_{22}^m , E_{33}^m , G_{12}^m , G_{13}^m , G_{23}^m and E_{11}^{m0} , E_{22}^{m0} , E_{33}^{m0} , G_{12}^{m0} , G_{13}^{m0} , G_{23}^{m0} are the damaged and undamaged elastic constants for the matrix, respectively. Note that rather than a single damage parameter for the initially isotropic matrix, there are six independent parameters that, in conjunction with the maximum strain formulation, are used to degrade components corresponding to each of the three principal directions in the elements used to model the domain of the matrix.

This formulation is justified for brittle materials such as brittle resins since the material is likely to fail through transverse cracking perpendicular to the load rather than through ductile yielding. In this formulation, unlike a formulation wherein all elastic constants of the material are failed equally once any one failure condition is reached, the stiffness components parallel to the failed surface are retained. As an example, if a tensile failure in the 11-direction is detected, the following damaged and undamaged elastic constants result:

$$\begin{aligned}
E_{11}^m &= D_{11}^m E_{11}^{m0} & G_{12}^m &= D_{12}^m G_{12}^{m0} \\
E_{22}^m &= E_{22}^{m0} & G_{13}^m &= D_{13}^m G_{13}^{m0} \\
E_{33}^m &= E_{33}^{m0} & G_{23}^m &= G_{23}^{m0}
\end{aligned} \tag{5.2.2.1-2}$$

where only the 11 components are degraded. Analogous situations for shear failures or failures in one of the other normal directions exist. Thus, the nominally isotropic matrix material must be considered as an orthotropic material once any of the “components” of the elasticity matrix has been degraded. Also, the shear moduli that were originally computed by the relationship for isotropic materials, can now be degraded independent of the elastic constants from which they were originally computed.

5.2.2.2 Damaged Material Formulation - Yarns

The formulation for the transversely isotropic yarns is analogous to the formulation for the matrix:

$$\begin{aligned}
E^y_{11} &= D^y_{11} E^{y0}_{11} & G^y_{12} &= D^y_{12} G^{y0}_{12} \\
E^y_{22} &= D^y_{22} E^{y0}_{22} & G^y_{13} &= D^y_{13} G^{y0}_{13} \\
E^y_{33} &= D^y_{33} E^{y0}_{33} & G^y_{23} &= D^y_{23} G^{y0}_{23}
\end{aligned} \tag{5.2.2.2-1}$$

where E^y_{11} , E^y_{22} , E^y_{33} , G^y_{12} , G^y_{13} , G^y_{23} and E^{y0}_{11} , E^{y0}_{22} , E^{y0}_{33} , G^{y0}_{12} , G^{y0}_{13} , G^{y0}_{23} are the damaged and undamaged elastic constants for the yarns, respectively.

Although four distinct failure modes are readily identifiable through the use of Hashin's criterion, the damaged material formulation falls into two classifications, damage resulting from the fiber modes and damage resulting from matrix modes:

fiber mode

$$\begin{aligned}
E^y_{11} &= D^y_{11} E^{y0}_{11} & G^y_{12} &= D^y_{12} G^{y0}_{12} \\
E^y_{22} &= E^{y0}_{22} & G^y_{13} &= D^y_{13} G^{y0}_{13} \\
E^y_{33} &= E^{y0}_{33} & G^y_{23} &= G^{y0}_{23}
\end{aligned} \tag{5.2.2.2-2}$$

matrix mode

$$\begin{aligned}
E^y_{11} &= E^{y0}_{11} & G^y_{12} &= D^y_{12} G^{y0}_{12} \\
E^y_{22} &= D^y_{22} E^{y0}_{22} & G^y_{13} &= D^y_{13} G^{y0}_{13} \\
E^y_{33} &= D^y_{33} E^{y0}_{33} & G^y_{23} &= D^y_{23} G^{y0}_{23}
\end{aligned} \tag{5.2.2.2-3}$$

where the 11-components are degraded for the fiber mode and all components except for the 11-component are degraded for the matrix mode. Also, it is important to reiterate that the conditions for matrix mode failure are dependent on both the 22- and 33-direction stresses.

This work is essentially an extension of the formulation for laminates that was presented by S.C. Tan [77.] and differs from the work of many of the other authors on progressive damage since in the present formulation, a considerable portion of the material stiffness may be retained after the initial failure. For example, in Lee [99.] and Chang [96.-98.], all transverse properties are set to zero in modes corresponding to matrix failure, and all properties are set to zero in modes corresponding to fiber failure. Although several components

of the stiffness of the matrix remain undamaged due to the fiber failure, they too are completely degraded. In the present work, Tan's system of state variables was modified to a form appropriate for a three-dimensional state, however, these state variables are determined as a fit to data from graphite/epoxy laminates and may not be entirely suitable for the glass/epoxy material system that is included in the results. In lieu of data for the material systems that are discussed in Chapters 4 and 6, the assumption must be made that the degradation values for the AS4/3502 and T300/1034 discussed by Tan are reasonable for the materials considered here. In any case, the system of degradation based on components of the elasticity matrix is more reasonable than the blanket degradation proposed by several other authors.

A possible consequence of degrading the material properties in this manner is that the elasticity matrix may become ill-conditioned. Lempriere [113.] notes that from thermodynamic considerations, the sum of the work done by all of the stress components must be positive to prevent the creation of energy. Thus, both the stiffness and compliance matrices must be positive definite. The conditions on the elements of the stiffness or compliance matrices place the following conditions on the elastic constants:

$$E_1, E_2, E_3, G_{12}, G_{13}, G_{23} > 0 \quad (5.2.2.2-4)$$

The resulting conditions on the Poisson's ratios are

$$|v_{ij}| < \left(\frac{E_j}{E_i} \right)^{1/2} \quad (5.2.2.2-5)$$

with $i, j=1,2,3$ and $i \neq j$ and

$$v_{12}v_{23}v_{31} < \frac{1}{2} \left[1 - v_{12}^2 \left(\frac{E_1}{E_2} \right) - v_{23}^2 \left(\frac{E_2}{E_3} \right) - v_{31}^2 \left(\frac{E_3}{E_1} \right) \right] < \frac{1}{2} . \quad (5.2.2.2-6)$$

These conditions place a restriction on both the magnitude of the Poisson's ratios relative to the corresponding elastic constants and on the product of $v_{12}v_{23}v_{31}$. Note that this latter condition is sign dependent, so if one Poisson's ratio is negative, this condition places no restrictions on the other two.

5.2.3 Assumed Stress-Strain Relationship

The assumed stress-strain relationship for the constituent materials is of the form given by Dougill [114.] and implemented in the work of Averill [101.]. Dougill notes that for an “ideal progressively fracturing solid,” the following statements are true. The solid:

- Loses stiffness due to stable progressive fracture during loading,
- Unloads in a linear-elastic manner, the stiffness depending on the extent of progressive fracture prior to unloading, and
- Has the property that the material may always be returned to a state of zero stress and strain by linear-elastic unloading.

The material is assumed to be brittle and as such undergo insignificant permanent deformation as damage occurs. According to Dougill “if the detailed structure of the material can be ignored in describing [the fracture] process, the discontinuities introduced into the displacement field can also be ignored. This suggests a way in which a continuum theory may be devised to describe the effects of stable progressive fracture in a heterogeneous solid.” In the present analysis, this approach is assumed to be valid for the brittle homogeneous matrix material in addition to the brittle heterogeneous yarn material. A typical stress-strain curve for a material such as the one described by Dougill is given as Figure 5.2.3a.

This stress-strain behavior is assumed to be valid at every Gauss point in the model for both the yarn and bulk matrix materials. In Figure 5.2.3a, E^0 and E^{damaged} represent each of the components of the original and degraded moduli, respectively. The post-failure stress is not zero, but rather the stress that is computed based on the newly degraded material properties and the value of the strain corresponding to the failure stress. Thus, the newly computed stress depends on the strain history, but not the stress history. Further, the stress can be thought of as though the material were unloaded to zero stress and strain immediately after failure and reloaded along the slope represented by E^{damaged} . The strain after failure never reaches another critical value in this model, thus for any Gauss point the material may be loaded until final failure is determined for the entire model. The means for determining the point at which the analysis is to be terminated will be discussed in an upcoming section.

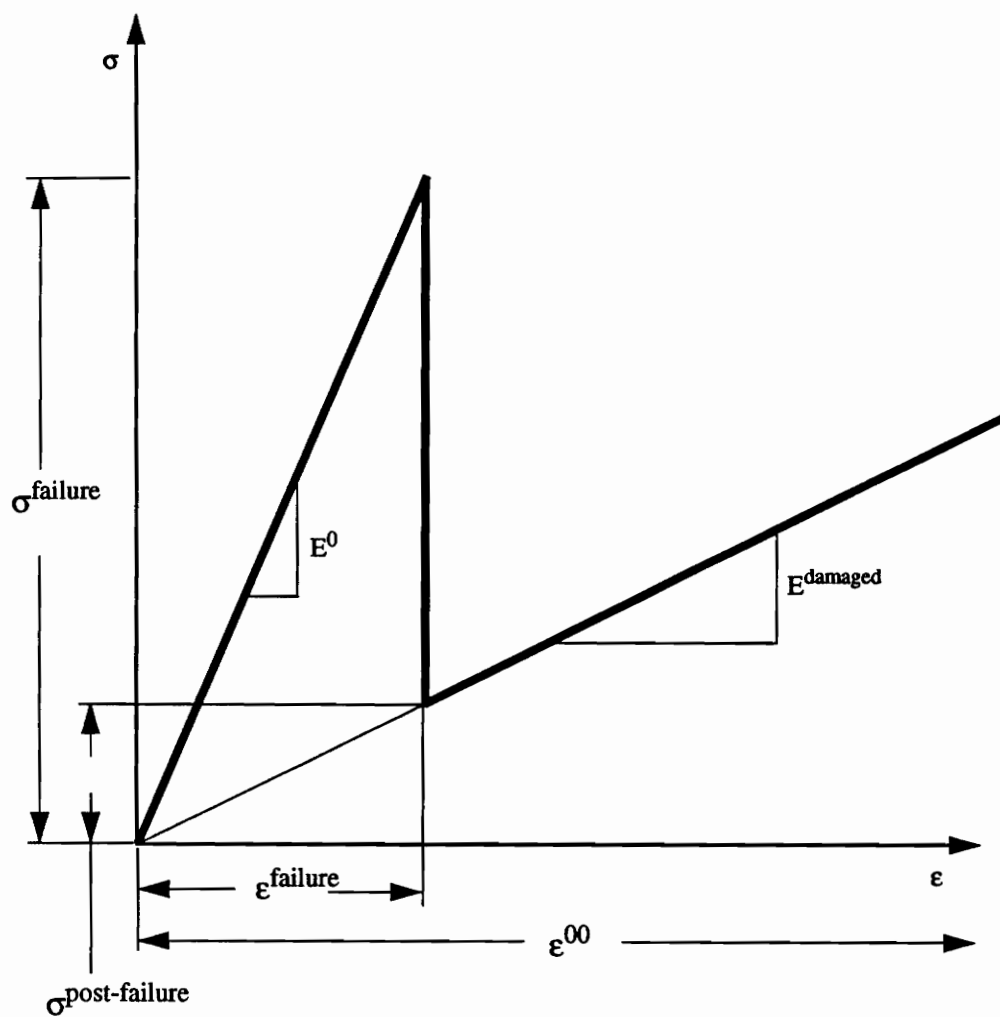


Figure 5.2.3a. Assumed stress-strain behavior for the constituent materials.

5.2.4 Computational Procedures

This material degradation model is implemented as an ABAQUS user defined material (UMAT) [115.-117.]. The fundamental components of the computational algorithm for the progressive failure analysis are given as follows:

1. Pass the current total strain vector, current (active) strain increment vector, array of material constants, and the array of the state variables representing the permanent damage state into the routine
2. Determine whether the Gauss point to be interrogated corresponds to matrix or yarn material
3. Guess at the current stress state based on the increment (permanently) degraded properties
4. Using the appropriate failure criterion (max stress for the matrix or Hashin for the yarns) determine if any additional damage has occurred for the current iteration of the increment
 - 4.1 If no additional damage is detected, return from the routine back to ABAQUS and continue with the current iteration
 - 4.2 If additional damage is found, degrade the appropriate components of the stiffness and recompute the stress state based on both the increment and iteration degraded properties and return to ABAQUS
5. Once a converged state is achieved, all state variables that correspond to a damaged state are stored permanently at the value that they last attained during the iterative procedure and the load is increased. Thus, once an elastic constant has been damaged at a converged state it will be permanently maintained in its damaged state.

A flowchart of this material degradation algorithm is given as Figure 5.2.4a.

At a particular Gauss point any or all of the components of the elasticity matrix may be degraded. The tracking of the damaged components is executed with a system of flags and is manifested within ABAQUS as a set of state variables (Step 5 of Figure 5.2.4a). The flags are set every time that the conditions for damage are met independent of whether the load increment has converged or not, however, only those flags corresponding to the converged state are retained by ABAQUS. The extent of the damaged state may actually change as the stress and strain fluctuate during the several iterations of a particular load step, but all flags that are set at the completion of the increment are retained for the duration of the analysis. Thus, the new state will always contain the previous damaged state as a subset.

Once any of three conditions is satisfied, program control is returned from the subroutine back to

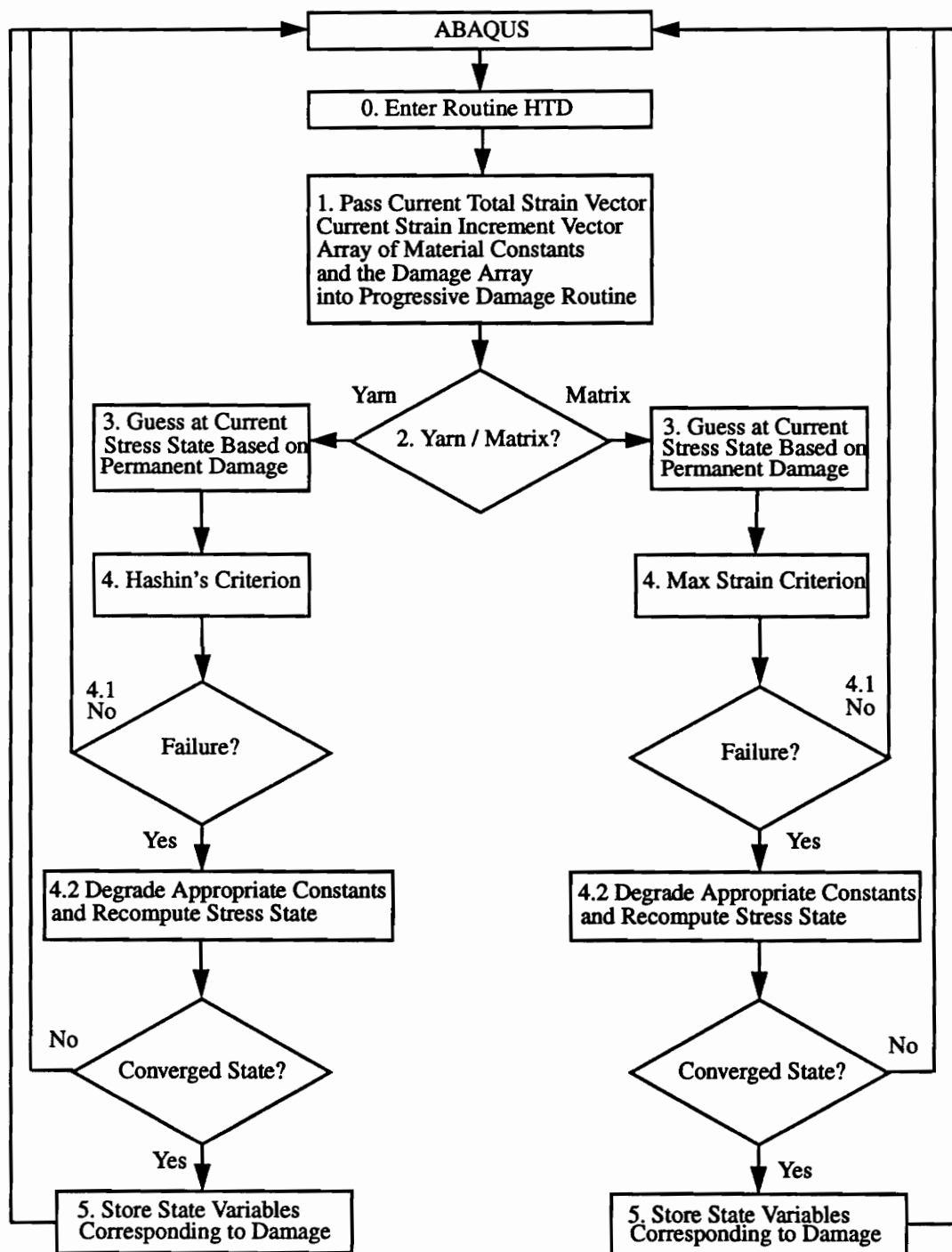


Figure 5.2.4a. Flowchart of the progressive failure algorithm.

ABAQUS. These three conditions are: 1) no failure detected, 2) failure detected, material properties degraded, but not currently at a converged state, and 3) failure detected, material properties degraded and state variables updated and stored. Note that these three conditions are mutually exclusive. Once an iteration has converged, ABAQUS increments the load and a new set of iterations begins.

The largest magnitude of the residual force as measured at the nodes is the criterion for convergence of the nonlinear Newton-Raphson routine within ABAQUS. The details of the Newton-Raphson method are discussed in the ABAQUS Theory Manual [116.] and in many texts on the finite element method [107.,118.,119.]. The Newton-Raphson technique is posed for a single degree of freedom problem by assuming that the current load, P_a , and displacement, u_a , are known [107.]. So

$$(k_0 + k_{na}) u_a = P_a \quad (5.2.4-1)$$

where k_0 is the portion of the stiffness corresponding to linear elastic deformation and k_{na} is the portion corresponding to the a^{th} nonlinear increment of deformation, i.e. $k_{na} = f(u_a)$. Next, the load is increased to a value P_b and the corresponding displacement is sought. Expanding $P=f(u)$ about u_a in a Taylor series expansion and noting that if u_a is a close approximation to the solution that the series can be truncated after the second term

$$f(u_a + \Delta u_1) = f(u_a) + \left(\frac{dP}{du}\right)_a \Delta u_1 \quad (5.2.4-2)$$

where

$$\frac{dP}{du} = \frac{d}{du} (k_0 u + k_n u) = k_t \quad (5.2.4-3)$$

and k_t is the tangent stiffness. To find the updated displacement, u_b , from the previous displacement, u_a , it is convenient to find the change in displacement, Δu_1 . This Δu_1 corresponds to the force $P_b = f(u_a + \Delta u_1)$. Then, P_b is given by

$$P_b - P_a = (k_t)_a \Delta u_1 \quad (5.2.4-4)$$

$P_b - P_a$ is the difference between the newly applied load, P_b , and the force $P_a = (k_0 + k_{na})u_a$ from the previous

displacement, u_a . The displacement increment Δu_1 is added to the previously converged displacement, u_a , to give the next estimated (but not necessarily converged) displacement. This procedure is repeated until the residual force, $P_b - P_i$, is sufficiently small. Typically, a maximum residual force on the order of $1.0E-8$ times the average nodal force corresponds to a converged state. The procedure is illustrated in Figure 5.2.4b.

It is important to reiterate that this routine is accessed by ABAQUS at every Gauss point in the model for every iteration of every load step throughout the solution phase of the ABAQUS program execution. This allows the user to have complete control over the constitutive material behavior, while allocating the tasks of problem formulation and solution of the finite element equations to the commercial code. The advantages of this type of shared duty are considerable. In the present analysis, for example, there was no advantage to redevelopment of either the quadratic tetrahedron or the nonlinear solver that are used. However, the ability to implement a material model that incorporates the specific features of the one discussed in this Chapter is crucial. The analysis is terminated at the point where the convergence of the solution becomes prohibitively slow and the load increment size becomes very small.

5.3 Verification of the Progressive Failure Model

The final step of the development and implementation of any new constitutive model must include a verification of the algorithm on a simple case whereby the individual branches within the routine can be verified separately. Discussed in this section is the procedure and results of the verification process.

5.3.1 Development of a Verification Procedure

Probably the best method for verifying an algorithm such as this one is to create a simple one element test case and interrogate the results. A single element (ABAQUS CPE8R) model with a constitutive behavior defined by the algorithm (equations 5.2.2.1-2) was developed. The boundary conditions are as shown in Figure 5.3.1a and the loading was a uniform force applied to the $x=1.0$ face. For the specific case discussed here, the material was considered to be isotropic with the load history shown in Figure 5.3.1b. Note that the first segment of the load is of a positive sense and does not quite reach a magnitude corresponding to the failure stress in tension of the material. The second segment of the load is of a negative sense and reaches a

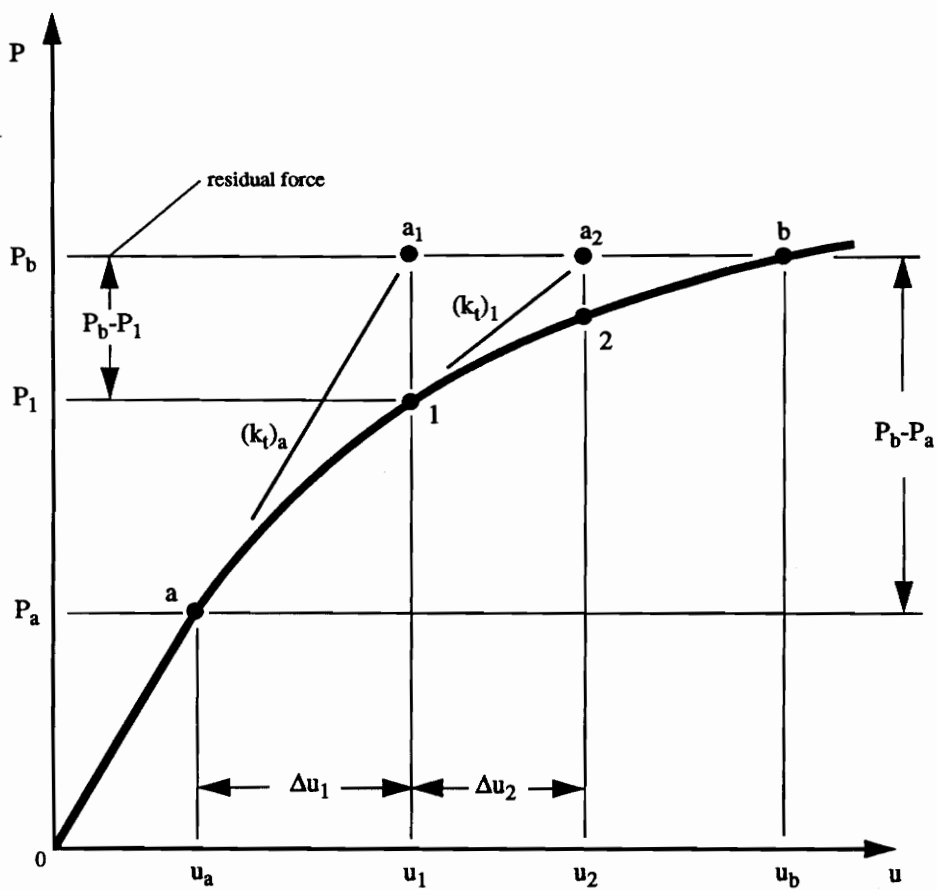


Figure 5.2.4b. Newton-Raphson routine.

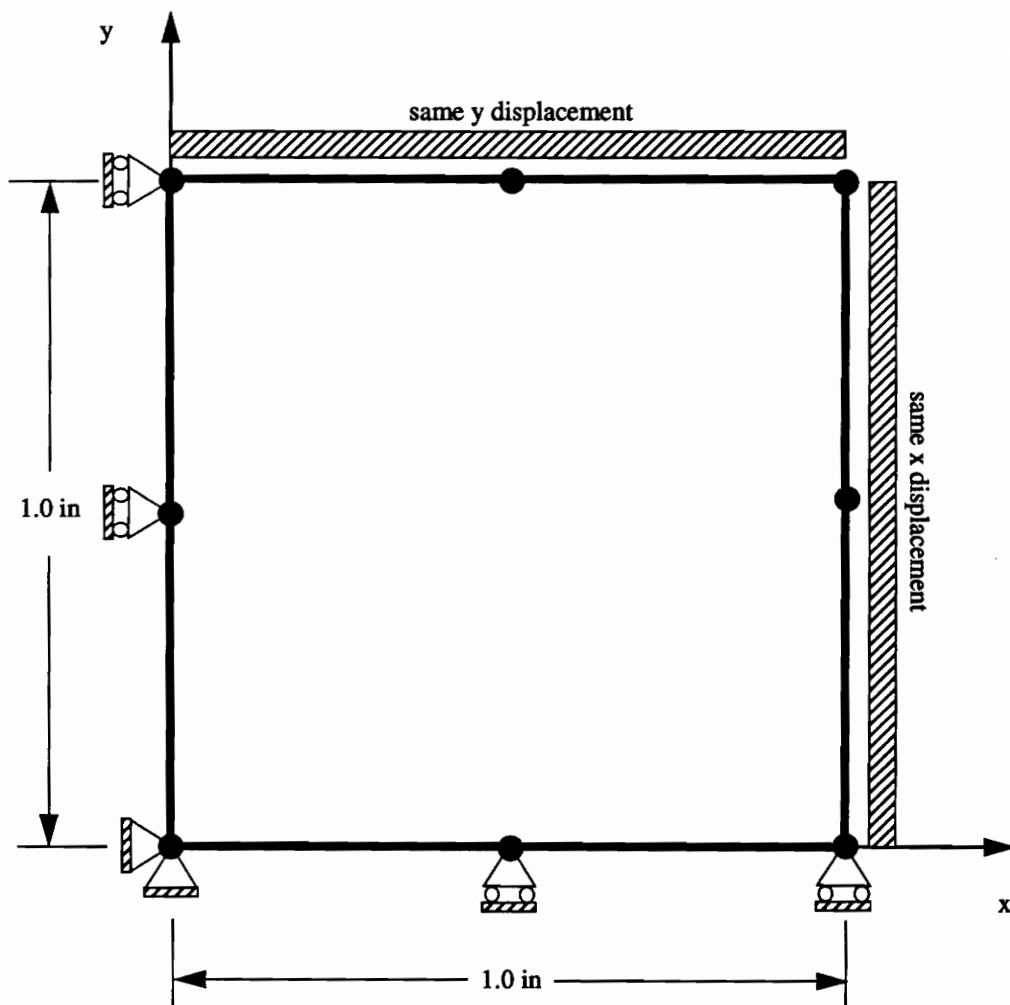


Figure 5.3.1a. Geometry and boundary conditions of verification model.

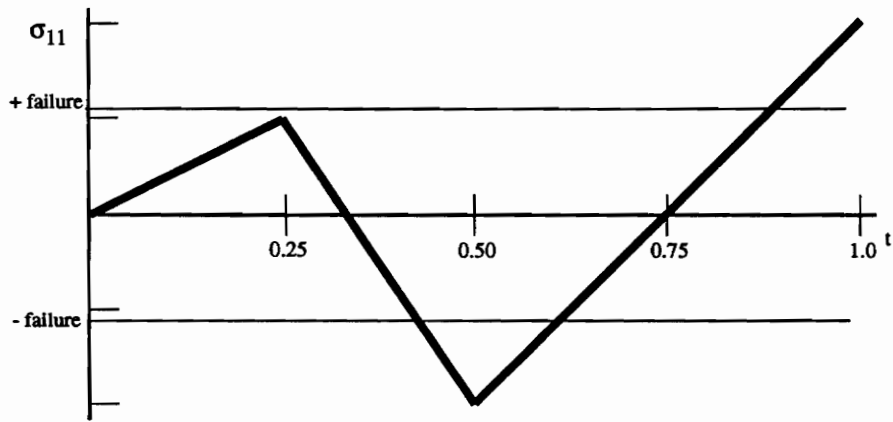


Figure 5.2.3b. Load history for verification model.

magnitude well above the failure stress in compression. The final segment is of a positive sense and continues to the same magnitude as the second segment.

5.3.2 Results of the Verification Procedure

The corresponding stress-strain (σ_{11} - ϵ_{11}) behavior is given as Figure 5.3.2a. and is discussed as follows. Segment 1-2 is the response corresponding to the initial segment of the load and as expected, does not reach the failure stress of the material in tension. Segment 2-3 corresponds to the portion of the load that is required to produce failure in compression. The segment 3-4 is the nonlinear stress-strain step corresponding to the new equilibrium state for the model based on the degraded stiffness. The algorithm within ABAQUS is load controlled, so the new equilibrium state at position 4 corresponds to the next increment of the load and the corresponding displacement. If the load were truly continuous rather than in a discrete form, the new equilibrium position would correspond to point 5.

Once the iterative process of determining the new equilibrium position has completed, the load is again incremented and a linear behavior based on the new constitutive relationship is determined as position 6. Position 6 corresponds to the minimum compressive load applied to the model. Finally, since no new failures have occurred, the material is governed by the constitutive behavior of segment 5-6, and the model is loaded through segment 6-7.

The large increase in strain (or displacement) at (ideally) constant load seen in steps 3-4 (or 3-5) is very similar to the phenomenon of pop-in seen during meta-stable crack growth during load controlled fracture [120.]. This is a consequence of the property degradation algorithm whereby the change in material properties is discrete rather than the gradual change implemented in plasticity algorithms. In a larger model such as the one described in Chapters 4 and 6, where the domain of the initial damage is small compared with the domain of the model, rather than the entire model as in this test case, this effect should be less prominent. Additional test cases have shown similar behavior.

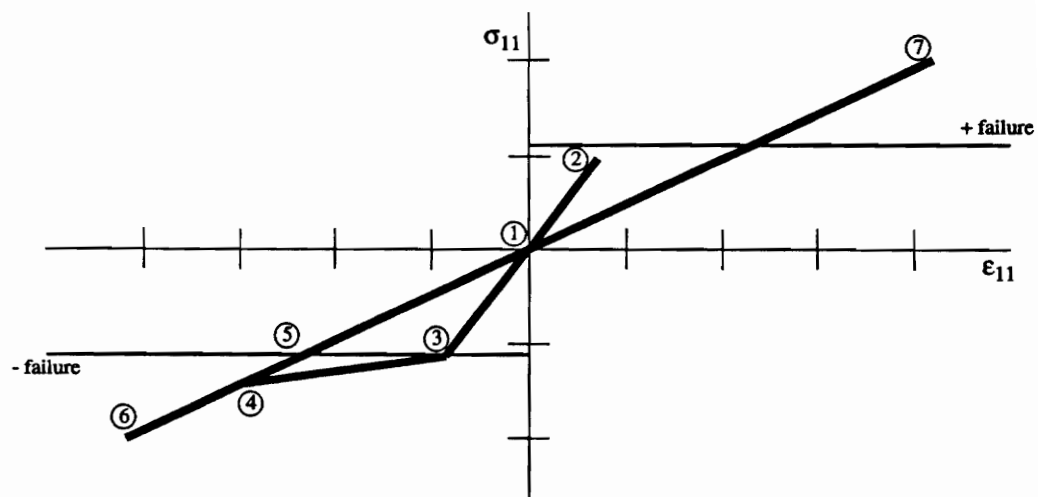


Figure 5.3.2a. Loading direction stress-strain behavior for verification model.

6.0 Failure Model Results for a Plain Weave

Included in this chapter is a discussion of the results obtained from the models discussed in Chapter 3 using the progressive failure algorithm that was developed in Chapter 5. Specifically, the results of a progressive failure analysis of the plain weave under mechanical loading are discussed. The difficulty of presenting the components of strain and stress within the material was noted in Chapter 4. As a result, only failure surfaces are presented and discussed. These failure surfaces represent the extent of the damaged material for a given applied load from the linear elastic response through the point at which the analysis is terminated.

6.1 Cases Considered: Material Properties, Loading, and Boundary Conditions

6.1.1 Material Properties

The material properties for the elastic behavior of the material were first given in Table 3.2.3b and are restated here for convenience. The progressive failure algorithm that was developed in Chapter 5 is based on the Hashin failure criterion for yarn failures and a maximum stress failure criterion for bulk matrix failures. Included in Table 6.1.1a are the assumed ultimate stresses for both the yarn and matrix materials. As with the values for the elastic constants, these values are considered representative of typical glass/epoxy material systems, but may not necessarily correspond to any one system. Only the glass/epoxy system is considered in this chapter, though the analysis should lend itself to virtually any material system.

Table 3.2.3b. Elastic properties of the materials considered.

Material Properties	Epoxy Matrix	Glass / Epoxy Yarn	Carbon / Epoxy Yarn
E_x (E6 psi)	0.5	5.5	23.0
E_y (E6 psi)	0.5	1.43	1.58
E_z (E6 psi)	0.5	1.43	1.58
G_{xy} (E6 psi)	0.1875	0.59	1.00
G_{xz} (E6 psi)	0.1875	0.59	1.00
G_{yz} (E6 psi)	0.1875	0.55	0.60
ν_{xy}	0.33	0.27	0.27
ν_{xz}	0.33	0.27	0.27
ν_{yz}	0.33	0.30	0.30
α_x (E-6 in/in °F)	25.0	4.83	0.010
α_y (E-6 in/in °F)	25.0	19.6	11.50
α_z (E-6 in/in °F)	25.0	19.6	11.50

Table 6.1.1a. Failure stresses of the idealized materials considered.

Material Allowables	Epoxy Matrix	Glass / Epoxy Yarn	Carbon / Epoxy Yarn
σ_A^+ (E3 psi)	x	126.5	270.0
σ_A^- (E3 psi)	x	87.7	215.0
σ_T^+ (E3 psi)	x	4.87	7.50
σ_T^- (E3 psi)	x	18.7	30.0
τ_T (E3 psi)	x	9.70	8.50
τ_A (E3 psi)	x	20.0	20.0
σ^+ (E3 psi)	12.0	x	x
σ^- (E3 psi)	17.0	x	x
τ (E3 psi)	8.50	x	x

Hashin [66.] notes that the ultimate transverse shear stress, τ_T , that appears in his failure criterion is difficult to measure, but that any general failure criterion must include this quantity. The value that is given in Table 6.1.1a corresponds to what is assumed to be the lower bound on this value for the general material system considered, that is the value of the ultimate shear stress for the bulk matrix material.

Once a failure has been computed at a given Gauss point, the material is degraded in accordance with the work of Tan [77.] as discussed in Chapter 5. The values of the internal state variables that represent the damaged state of the material, D_{ij} , may be assigned for each constituent material and each component of stiffness. To reiterate, the D_{ij} can be thought of as the fraction of the original stiffness that is retained after damage has occurred. $D_{ij}=1$ represent an undamaged material, while $D_{ij}=0$ represent a completely degraded material. The values that have been chosen for the D_{ij} were originally given by Tan for standard carbon/epoxy systems (AS4/3502 and T300/1034-C).

Specifically, the procedure discussed by Tan for determining the values of D_{ij} for the carbon/epoxy systems is to set D_{ij} $i,j \neq 1$ equal to 0.20 and vary D_{11} from 0.00 to 0.10. Tan tested a $[0/90/\pm 45]_s$ laminate containing a circular hole to failure and compared to a model of an equivalent material. The value of D_{11} that produced an analytical stress-strain curve most closely matching the experimentally determined curve was chosen. These D_{ij} were then assumed to be representative of all laminates composed of the material system.

Although Tan showed that the prediction of the ultimate strength of the material is sensitive to the choice of stiffness degradation factors, the process for determining the values requires considerable experimental effort and expense. This was not possible in the present study, thus the values developed by Tan are used here as an estimate of the actual parameters for the glass/epoxy materials and are given in Table 6.1.1b. As will be discussed in later sections of this chapter, the results are quite reasonable.

6.1.2 Loading

The loading that has been chosen for the progressive failure cases discussed herein is a simple monotonically increasing axial force applied uniformly to the positive x -face of the representative volume element. In

Table 6.1.1b. Elastic properties of the materials.

D_{ij}	Epoxy Matrix	Glass / Epoxy Yarn	Carbon / Epoxy Yarn
D_{11}	0.20	0.07	0.07
D_{22}	0.20	0.20	0.20
D_{33}	0.20	0.20	0.20
D_{12}	0.20	0.20	0.20
D_{13}	0.20	0.20	0.20
D_{23}	0.20	0.20	0.20

the cases shown here, the convergence of the analysis became prohibitively slow and the resulting load increments became prohibitively small before the load carrying capability of the material was entirely exhausted. Thus, the analysis was terminated at the state of the material response corresponding to the first load increment of less than 1% of the load amplitude. The load is applied as a function of a fictitious “time,” t , where a time of $t=0$ corresponds to zero load and a time of $t=1$ corresponds to the full amplitude of the load.

6.1.3 Boundary Conditions

The boundary conditions considered herein are representative of the simplest case, that of a representative volume element that is located far from any geometric boundary, i.e., periodic boundary conditions.

6.2 Analysis of a Fiberglass/Epoxy Material with Periodic Boundary Conditions and a Monotonically Increasing Axial Load

The case of glass/epoxy yarns in an epoxy matrix is considered since the progression to failure is more quantifiable than the corresponding results for the carbon/epoxy systems. The load history for this model is given in Table 6.2.1a. Note that the first three load steps are linear, and that first failure occurs between the third and fourth load step. Three attempts are made to reach the sixth load step, that is, the original load increment was reduced twice to obtain a load increment that was small enough to allow force equilibrium convergence. The analysis was terminated after this load step since it appeared that the rate of convergence of the next load step was prohibitively slow.

Figure 6.2.1a¹ is used to represent the gross stress strain behavior of the RVE. The most prominent feature of this figure is that damage events illustrated in Figures 6.2.1c-6.2.1e are captured at the “knees” of the stress-strain curve. Although the actual damage progression is continuous from onset through final failure, capturing the actual stress-strain curve would require essentially infinitely small load increments. Thus, the load history shown in Table 6.2.1a is used for reasons of practicality. Similarly, the stress-strain curve shown

1. See Appendix C: Figures from Chapter 6

Table 6.2.1a. Load history for a glass/epoxy material with periodic boundary conditions.

Load Step	Attempts	Iterations in Final Attempt	Load Increment (lb)	Total Load (lb)
1	1	1	10.00	10.00
2	1	1	10.00	20.00
3	1	1	15.00	35.00
4	1	7	22.50	57.50
5	1	7	22.50	80.00
6	3	1	2.812	82.81

as Figure 6.2.1a is characterized by discrete increments in damage and resulting decrease in axial modulus. Note that E_x^0 , E_x^{d1} , E_x^{d2} and E_x^{d3} correspond to the undamaged state, and the states shown in Figures 6.2.1c through 6.2.1e, respectively. Note that there is only an insignificant decrease in axial modulus from load step 5 to load step 6.

The decrease in axial modulus corresponding to the damage of Figure 6.2.1b has not been plotted on the curve of Figure 6.2.1a since the decrease in the axial stiffness of the RVE due to this damage is very small. This damage corresponds to the damage state just after the onset of tensile matrix mode (TMM) failure within the transverse yarns. As discussed in Chapter 5, the tensile matrix mode failure is dependent on the transverse, through thickness, and shear properties and states of stress within the yarns. Note that the isosurfaces at (1) in Figure 6.2.1b are centered about the x -axis and do not extend to the edges of the RVE. Since this model is idealization of a manufactured material, it is reasonable to assume that the actual location of the initiation of failure will be a function of variations in the manufacturing process, though for a plain weave far from any boundary and subjected to a uniform state of axial tension, it is likely that failure will initiate near (2).

The damage that was shown in Figure 6.2.1b is considered to be continuous and to uniformly effect the behavior of the yarns. This assumption of a continuum damage state comes from the assumption that the yarns are homogeneous, rather than being composed of thousands of individual filaments each having a local stress state. However, it must be acknowledged that experimentation has shown that a manufactured material will exhibit discrete crack growth along the fibers within the transverse yarns [108.]. For reasons of computational practicality, it is not feasible to attempt to predict the location of the discrete failure events within the yarn. This has lead to the present continuum approach for damage assessment.

Shown in Figure 6.2.1c is the state of damage progression in the RVE at a load of 57.50 lb. Note that the tensile matrix mode damage has progressed along the entire length of the transverse yarns and now involves more than one-third of the volume of the transverse yarns. This load corresponds to the fourth load step in the analysis as shown in Table 6.2.1a. The damaged volume is sufficiently large to cause a noticeable decrease in stiffness of the RVE, corresponding to (1) in Figure 6.2.1a.

At a load of approximately 80.00 lb, most of the yarn has failed in the tensile matrix mode. This stage of damage progression is shown as (1) in Figure 6.2.1d and (2) of Figure 6.2.1a. The axial modulus has decreased from 1.411E6 psi before damage to 1.196E6 psi at the state shown in Figure 6.2.1d. The locations shown as (2) are locations within the transverse yarns that have not met the criterion for failure.

The final state of damage that was computed for this model is shown in Figure 6.2.1e. Note that the load increase corresponding to this damaged state is only 2.812 lb, thus this damaged state is insignificantly larger than the state shown in Figure 6.2.1d. The damage (1) corresponds to the final location (3) that is shown on the stress-strain curve of Figure 6.2.1a. It is important to note that this state does not correspond to any standard definition of final failure, since the load carrying capability of the material has not been exhausted. The actual state corresponding to final failure must certainly involve the failure of the load bearing capability of the axial yarns in what Hashin [66.] refers to as tensile fiber mode (TFM) failure. Rather, this is the state at which the ABAQUS internal solver was unable to proceed with sufficiently large load steps to warrant further computation expenditures.

7.0 Contributions, Conclusions and Recommendations

This chapter includes a discussion of the significance of the contributions to the field of textile mechanics that have been made during the course of this work, several conclusions that can be made about the work, and several recommendations for the continuation of this research.

7.1 Contributions

The work that has been presented herein was executed as a part of NASA Langley Research Center's Mechanics of Textile Composites Work Group. This portion of the overall undertaking was focused on the study of the details of the response of a plain weave textile composite material through the linear elastic regime and well beyond initial failure. To that end, an analysis of the representative volume element (RVE) of the textile proceeded wherein a textile geometry model was integrated with a finite element based approach to interrogate the internal details of the elastic response of the material. Further, a progressive failure routine was developed that allows for the interrogation of the response of the textiles well beyond initial failure.

The specific contributions of this work to the field of textile mechanics are as follows:

The development of an integrated approach for model development, including:

- Assessment and refinement of Pastore's textile geometry model as applied to the structural modeling of textile based composite materials, and
- Development of a flexible procedure for creating finite element models directly from a geometrically thorough textile geometry model, and

- Verification of the models through comparison with other models and experimental results.

The assessment of the linear elastic response of a representative volume element of a plain weave textile composite, including:

- Consideration of the effects of material properties, boundary conditions, and axial and thermal loadings, and
- Assessment of the internal response quantities including displacement and strain energy density within the RVE, and
- Study of the effects of RVE placement and free edge effects on the response of woven textiles.

The development of a progressive failure algorithm for the interrogation of the behavior of textile based composites beyond their linear elastic response, including:

- Consideration and assessment of several failure criteria for both yarn and matrix material, and
- Development of a progressive failure and material discount routine, and
- Classification of the materials as stable progressively fracturing solids, and
- Integration of the routine with the commercial finite element code, ABAQUS.

The assessment of the progressive failure response of a representative volume element of a glass/epoxy plain weave textile composite, including:

- Prediction of the nonlinear load-deflection response of the RVE, and
- Prediction of the location, mode, and load of the initiation of failure within the RVE, and
- Study of the progression of failure throughout the transverse yarns.

The presentation of the results of these analyses in a format suitable for assessment of the behavior of the materials.

7.2 Conclusions

The following conclusions can be made regarding the use of the current models for interrogation of the response of the elastic and progressive failure of composites fabricated from woven preforms:

- Finite element models that incorporate many geometric details not found in other analyses can be taken directly from the textile geometry model, and
- Although the models are computationally expensive to analyze, they provide considerable insight into details of the internal response of textile based composites (Section 4.3), and
- The location of a given representative volume element within the overall material has significant influence on the details of the elastic response of the RVE, and
- The extension to more complicated architectures, loadings and boundary conditions is straightforward, and
- Consideration of the yarns and matrix as separate materials, each having several potential failure modes that are dependent on the local state of stress allows selective degradation of the local material properties, and
- Failure of a representative volume element of a glass/epoxy plain weave that is subjected to an

axial force initiates as a tensile matrix mode failure near the major elliptic axis of the transverse yarns and proceeds until the entire domain of the transverse yarns is involved, and

- Final failure of the material cannot be assessed until the load bearing capability of the axial yarns is exhausted.

7.3 Recommendations

There are almost endless possibilities for improving and extending the current models for different material systems, architectures, boundary conditions, loadings, etc. Some specific recommendations include:

- Application of the analysis to the study of braided textile composites - this requires the solution of several problems with the textile geometry model, and
- Development of material degradation factors for a variety of materials, and
- Solution of the anomalous behavior of the progressive failure routine for carbon/epoxy material systems.

References

1. Glaessgen, E.H., Pastore, C.M., Griffin, Jr., O.H., and Birger, A., "Geometrical and Finite Element Modeling of Textile Composites," **Composites Part B**, Vol. 27B, No. 1, 1996, pp. 43-50.
2. Glaessgen, E.H., Pastore, C.M., Griffin, Jr., O.H., and Birger, A., "Modeling of Textile Composites," **Proceedings of the First International Conference on Composites Engineering**, 1994, New Orleans, LA, pp. 183-184.
3. Kaufmann, J.R., "Industrial Applications of Multiaxial Warp Knit Composites," **Proceedings of Fiber-Tex 1991**, NASA CP3176, pp.77-86.
4. Scardino, F., "Chapter 1: An Introduction to Textile Structures and their Behavior," **Composite Materials Series, Volume 3: Textile Structural Composites**, Elsevier, 1989, pp. 1-26.
5. Ko, F.K., Pastore, C.M., and Head, A.A., **Atkins and Pearce Handbook of Industrial Braiding**, to be published.
6. Hearle, J.W.S., "Chapter2: Mechanics of Yarns and Nonwoven Fabrics," **Composite Materials Series, Volume 3: Textile Structural Composites**, Elsevier, 1989, pp. 27-65.
7. Kawabata, S., "Chapter 3: Nonlinear Mechanics of Woven and Knitted Materials," **Composite Materials Series, Volume 3: Textile Structural Composites**, Elsevier, 1989, pp. 67-116.
8. Ko, F.K., "Preform Fiber Architecture for Ceramic-Matrix Composites," **Ceramic Bulletin**, Vol. 68, No. 2, 1989, pp. 401-413.
9. Dominguez, F.S., "Woven Fabric Prepregs," **Composites: Engineered Materials Handbook**, Vol. 1, ASM International, 1987, pp. 148-150.
10. Ko, F.K., "Braiding," **Composites: Engineered Materials Handbook**, Vol. 1, ASM International, 1987, pp. 519-528.
11. Skelton, J., "Chapter 4: Triaxially Braided Materials for Composites," **Composite Materials Series, Volume 3: Textile Structural Composites**, Elsevier, 1989, pp. 117-128.
12. Yurgartis, S.W., and Maurer, J.P., "Modelling weave and stacking configuration effects on interlaminar shear stresses in fabric laminates," **Composites**, Vol. 24, No. 8, 1993, pp. 651-658.

13. Ko, F.K. and Hartman, D., "Impact Behavior of 2-D and 3-D Glass/Epoxy Composites," **SAMPE Journal**, July/Aug. 1986, pp.26-29.
14. Crane, R.M. and Camponeschi, E.T., "Experimental and Analytical Characterization of Multidimensionally Braided Graphite/Epoxy Composites," **Experimental Mechanics**, Vol. 26, No. 3, Sept. 1986, pp. 259-266.
15. Camponeschi, E.T., Wall, L.L., and Crane, R.M., "Theoretical and Experimental Analysis of Multidirectionally-Braided Composites," **SME-86-75**, Sept. 1986.
16. Brookstein, D. and Tsiang, T., "Load Deformation Behavior of Composite Cylinders with Integrally Formed Braided and Machined Holes," **Journal of Composite Materials**, Vol. 19, 1985, pp. 476-487.
17. Hearle, J.W.S. and Du, G.W., "Forming Rigid Fiber Assemblies: The Interaction of Textile Technology and Composites Engineering," **Journal of the Textile Institute**, Vol. 81, No. 4, 1990, pp. 360-383.
18. Jones, R.M., **Mechanics of Composite Materials**, Hemisphere Publishing Company, New York, 1975.
19. Poe, Jr., C.C., and Harris, C.E., **Mechanics of Textile Composites Conference**, NASA CP-3311, 1995.
20. Masters, J.E., Foye, R.L., Pastore, C.M., and Gawayed, Y.A., "Mechanical Properties of Triaxially Braided Composites: Experimental and Analytical Results," **Journal of Composites Technology and Research**, Vol. 15, No. 2, 1993, pp. 112-122.
21. Pastore, C.M., **A Processing Science Base for Three Dimensional Braids**, Ph.D. Thesis, Drexel University, Philadelphia, PA, March 1988.
22. Pastore, C.M., and Ko, F.K., "Modelling of Textile Structural Composites, Part I: Processing-Science Model for Three-Dimensional Braiding," **Journal of the Textile Institute**, Vol. 81, No. 4, 1990, pp. 480-490.
23. Du, G.-W., Chou, T.-W., and Popper, P., "Analysis of Three-Dimensional Textile Preforms for Multidirectional Reinforcement of Composites," **Journal of Materials Science**, Vol. 26, 1991, pp. 3438-3448.
24. Li, W., Hammad, M., and El-Shiekh, A., "Structural Analysis of 3-D Braided Preforms for Composites, Part I: The Four-Step Preforms," **Journal of the Textile Institute**, Vol. 81, No. 4, 1990, pp. 491-514.
25. Li, W., Hammad, M., and El-Shiekh, A., "Structural Analysis of 3-D Braided Preforms for Composites, Part II: The Two-Step Preforms," **Journal of the Textile Institute**, Vol. 81, No. 4, 1990, pp. 515-537.
26. Du, G.-W., and Ko, F.K., "Unit Cell Geometry of 3-D Braided Structures," **J. Reinforced Plastics and Composites**, Vol. 12, July 1993, pp. 752-768.
27. Armstrong-Carroll, E., Pastore, C.M., and Ko, F.K., "Modeling of Euclidean Braided Fiber Architectures to Optimize Composite Properties," **FiberTex '91**, Buckley, J.D., ed., NASA CP3176, NASA, 1992, pp.153-156.
28. Naik, N.K. and Ganesh, V.K., "Prediction of On-Axes Elastic Properties of Plain Weave Fabric Composites," **Composites Science and Technology**, Vol. 45, 1992, pp. 135-152.
29. Naik, N.K. and Ganesh, V.K., "Failure Behavior of Plain Weave Fabric Laminates Under In-Plane Shear Loading," **Journal of Composites Technology and Research**, Vol. 16, No. 1, Jan. 1994, pp. 3-20.
30. Raju, I.S. and Wang, J.T., "Classical Laminate Theory Models for Woven Fabric Composites," **NASA TM 109087**, NASA, Feb. 1994, Hampton, VA.

31. Ishikawa, T., and Chou, T.-W., "Elastic Behavior of Woven Hybrid Composites," **Journal of Composite Materials**, Vol. 16, Jan 1982, pp. 2-19.
32. Ishikawa, T., and Chou, T.-W., "Nonlinear Behavior of Woven Composites," **Journal of Composite Materials**, Vol. 17, Sept 1993, pp. 399-413.
33. Chou, T.-W. and Ishikawa, T., "Analysis and Modeling of Two-Dimensional Fabric Composites," in **Textile Structural Composites**, T.-W. Chou and F.K. Ko, Eds., Elsevier, 1989, pp. 210-263.
34. Ishikawa, T., and Chou, T.-W., "One-Dimensional Micromechanical Analysis of Woven Fabric Composites," **AIAA Journal**, Vol. 21, No. 12, 1983, pp. 1714-1721.
35. Ishikawa, T., and Chou, T.-W., "In-Plane Thermal Expansion and Thermal Bending Coefficients of Fabric Composites," **Journal of Composite Materials**, Vol. 17, March 1983, pp. 92-104.
36. Yang, J.-M. and Chou, T.-W., "Thermo-Elastic Analysis of Triaxially Woven Fabric Composites," in **Textile Structural Composites**, T.-W. Chou and F.K. Ko, Eds., Elsevier, 1989, pp. 265-277.
37. Yang, J.-M., Ma, C.-L., and Chou, T.-W., "Fiber Inclination Model of Three-Dimensional Textile Structural Composites," **Journal of Composite Materials**, Vol. 20, Sept. 1986, pp. 472-484.
38. Ko, F.K., Pastore, C.M., Lei, C., and Whyte, D.W., "A Fabric Geometry Model for 3-D Braid Reinforced FP/Al-Li Composites," **International SAMPE Metals Conference: Competitive Advances in Metals/Metal Processing**, Cherry Hill, NJ, August 1987.
39. Ma, C.-L., Yang, J.-M., and Chou, T.-W., "Elastic Stiffness of Three-Dimensional Braided Textile Structural Composites," in **Composite Materials: Testing and Design (Seventh Conference)**, ASTM STP 893, J.M. Whitney, Ed., American Society for Testing and Materials, Philadelphia, 1986, pp. 404-421.
40. Gowayed, Y.A., **An Integrated Approach to the Prediction of Mechanical and Geometric Properties of Textile Reinforced Composites**, Ph.D. Thesis, North Carolina State University, Feb. 1992.
41. Pastore, C.M. and Gowayed, Y.A., "A Self-Consistent Fabric Geometry Model: Modification and Application of a Fabric Geometry Model to Predict the Elastic Properties of Textile Composites," **Journal of Composites Technology and Research**, Vol. 16, No. 1, Jan. 1994, pp. 32-36.
42. Foye, R.L., "The Mechanics of Fabric Reinforced Composites," **FiberTex 1988**, NASA CP3038, 1989.
43. Kriz, R.D., and Muster, W.J., "Mechanical-Damage Effects in Woven Laminates at Low Temperatures," Unpublished work.
44. Kriz, R.D., "Influence of Damage on Mechanical Properties of Woven Composites at Low Temperatures," **Journal of Composites Technology and Research**, Vol. 7, No. 2, 1985, pp. 55-58.
45. Lei, C. Y.-J. Cai, and Ko, F.K., "Finite Element Analysis of 3-D Braided Composites," **Fibrous Materials Research Center**, 1990.
46. Pastore, C.M. and Cai, Y.J., "Application of Computer Aided Geometric Modeling for Textile Structural Composites," 1990.
47. Carter, W.C., Cox, B.N., Dadkah, M.S., and Morris, W.L., "An Engineering Model of Composites Based on Micromechanics," **Acta Metallurgica**, accepted, 1995.
48. Naik, R.A., "Analysis of Woven and Braided Fabric Reinforced Composites," **NASA CR-194930**, NASA, June 1994.
49. Naik, R., Ifju, P.G., and Masters, J.E., "Effect of Fiber Architecture Parameters on Mechanical Perfor-

mance of Braided Composites," Proceedings of the 4th NASA/DoD Advanced Composites Technology Conference, June 7-11, 1993, Salt Lake City, Utah, NASA CP3229, Vol. 1, Part 1, pp. 525-554.

50. Dasgupta, A., Bhandarkar, S., Pecht, M., and Barker, D., "Thermoelastic Properties of Woven-Fabric Composites Using Homogenization Techniques," **Proceedings of the American Society for Composites, Fifth Technical Conference**, June 12-14, 1990, East Lansing, Michigan, pp. 1001-1010.

51. Dasgupta, A., and Bhandarkar, S.M., "Effective Thermomechanical Behavior of Plain-Weave Fabric-Reinforced Composites Using Homogenization Theory," **Journal of Engineering Materials and Technology**, Vol. 116, Jan 1994, pp. 99-105.

52. Dasgupta, A., and Agarwal, R.K., "Orthotropic Thermal Conductivity of Plain-Weave Fabric Composites Using a Homogenization Theory," **Journal of Composite Materials**, Vol. 26, No. 18, 1992, pp. 2736-2758.

53. Woo, K. and Whitcomb, J.D., "Global/Local Finite Element Analysis for Textile Composites," **34th AIAA/ASME/ASCE/AHS/ACS Structures, Structural Dynamics, and Materials Conference**, La Jolla, CA, 1993, pp.1721-1731.

54. Whitcomb, J.D., "Three-Dimensional Stress Analysis of Plain Weave Composites," NASA TM-101672, Nov. 1989.

55. Whitcomb, J.D., "Three-Dimensional Stress Analysis of Plain Weave Composites," **Composite Materials: Fatigue and Fracture**, ASTM STP 1110, T.K. O'Brien, Ed., ASTM, 1991, pp. 417-438.

56. Lene, F. and Paumelle, P., "Micromechanics of Damage in Woven Composites," **Composite Material Technology**, PD-Vol.45, 1992, pp.97-105.

57. Blacketter, D.M., Walrath, D.E., and Hansen, A.C., "Modelling Damage in Plain Weave Fabric Reinforced Composite Materials," **Journal of Composites Technology and Research**, Vol. 15, No. 2, 1993, pp.136-142.

58. Foye, R.L., "Improved Inhomogeneous Finite Elements for Fabric Reinforced Composite Mechanics Analysis," in **Fiber-Tex '91**, NASA CP3176, NASA, 1992.

59. Dellinger, G. and Foye, R.L., "An Approximate Method of Stress Analysis for Fabric Reinforced Composites," in **Fiber-Tex '89**, NASA CP3082, NASA, 1990.

60. Glaessgen, E.H. and Griffin, Jr., O.H., "Micromechanical Analysis of Thermal Response in Textile-Based Composites," **Aerospace Thermal Structures and Materials for a New Era**, E.A. Thornton, Ed., AIAA, 1995, pp. 204-217.

61. Glaessgen, E.H. and Griffin, Jr., O.H., "Effect of Applied Boundary Condition on the Analysis of Composites Based on Woven Preforms," **36th AIAA/ASME/ASCE/AHS/ACS Structures, Structural Dynamics, and Materials Conference**, New Orleans, LA, 1995.

62. Glaessgen, E.H. Griffin, Jr., O.H., "Finite Element Based Micro-Mechanics Modeling of Textile Composites," **Mechanics of Textile Composites Conference**, C.C. Poe, Jr. and C.E. Harris, Eds., NASA CP-3311, 1995, pp.555-586.

63. Raju, I.S., Foye, R.L., and Avva, V.S., "A Review of Analytical Methods for Fabric and Textile Composites," **Proceedings of Indo-US Workshop on Composite Materials for Aerospace Applications**, Bangalore, India, July 23-27, 1990, available as **Composite Structures, Testing, Analysis, and Design**, J.N. Reddy and A.V. Krishna Murty, Eds., 1992, pp.274-293, Narosa Publishing House, New Delhi, India.

64. Batdorf, S.B., "Tensile Strength of Unidirectionally Reinforced Composites - I," **Journal of Reinforced Plastics and Composites**, Vol. 1, April, 1982, pp. 153-164.
65. Batdorf, S.B., "Tensile Strength of Unidirectionally Reinforced Composites - II," **Journal of Reinforced Plastics and Composites**, Vol. 1, April 1982, pp. 165-176.
66. Hashin, Z., "Failure Criteria for Unidirectional Fiber Composites," **Journal of Applied Mechanics**, Vol.47, June 1980, pp.329-334.
67. Fujii, T., Amijima, S., and Lin. F., "Study on Strength and Nonlinear Stress-Strain Response of Plain Woven Glass Fiber Laminates under Biaxial Loading," **Journal of Composite Materials**, Vol. 26, No.17, 1992, pp. 2493-2510.
68. Yamada, S.E. and Sun, C.T., "Analysis of Laminate Strength and Its Distribution," **Journal of Composite Materials**, Vol. 12, April 1978, pp. 275-284.
69. Zang, W. and Gudmundson, P., "Damage Evolution and Thermoelastic Properties of Composite Laminates," **International Journal of Damage Mechanics**, Vol. 2, July 1993, pp.290-308.
70. Valliappan, S., Murti, V., and Wohua, Z., "Finite Element Analysis of Anisotropic Damage Mechanics Problems," **Engineering Fracture Mechanics**, Vol. 35, No. 6, 1990, pp. 1061-1071.
71. Shen, W., Peng, L.-H., and Yue, Y.-G., "Elastic Damage and Energy Dissipation in Anisotropic Solid Material," **Engineering Fracture Mechanics**, Vol. 33, No. 2, 1989, pp. 273-281.
72. Petit, P.H. and Waddoups, M.E., "Method of Predicting the Nonlinear Behavior of Laminated Composites," **Journal of Composite Materials**, Vol. 3, 1969, pp. 2-19.
73. Lagoudas, D.C. and Saleh, A.M., "Compressive Failure Due to Kinking of Fibrous Composites," **Journal of Composite Materials**, Vol. 27, No. 1, 1993, pp. 83-106.
74. Kim, Y.W., and Hong, C.S., "Progressive Failure Model for the Analysis of Laminated Composites Based on Finite Element Approach," **Journal of Reinforced Plastics and Composites**, Vol. 11, Oct. 1992, pp. 1078-1092.
75. Hwang, W.C., and Sun, C.T., "Failure Analysis of Laminated Composites By Using Iterative Three-Dimensional Finite Element Method," **Computers and Structures**, Vol. 33, No. 1, 1989, pp. 41-47.
76. Tolson, S. and Zabaraz, N., "Finite Element Analysis of Progressive Failure in Laminated Composite Plates," **Computers and Structures**, Vol. 38, No. 3, 1991, pp. 361-376.
77. Tan, S.C., "A Progressive Failure Model for Composite Laminates Containing Openings," **Journal of Composite Materials**, Vol. 25, May 1991, pp. 556-577.
78. Tan, S.-C. and Perez, J., "Progressive Failure of Laminated Composites with a Hole Under Compressive Loading," **Journal of Reinforced Plastics and Composites**, Vol. 12, Oct. 1993, pp. 1043-1057.
79. Swanson, S.R., and Christoforou, A.P., "Progressive Failure in Carbon/Epoxy Laminates Under Biaxial Stress," **Journal of Engineering Materials and Technology**, Vol. 109, Jan 1987, pp. 12-16.
80. Singh, U.K., and Digby, P.J., "A Continuum Damage Model for Simulation of the Progressive Failure of Brittle Rocks," **International Journal of Solids and Structures**, Vol. 25, No. 6, 1989, pp. 647-663.
81. Singh, U.K. and Digby, P.J., "The Application of a Continuum Damage Model in the Finite Element Simulation of the Progressive Failure and Localization of Deformation in Brittle Rock Structures," **International Journal of Solids Structures**, Vol. 25, No. 9, 1989, pp. 1023-1038.

82. Bakuckas, J.G., Tan, T.M., Lau, A.C.W., and Awerbuch, J., "A Numerical Model for Predicting Crack Path and Models of Damage in Unidirectional Metal Matrix Composites," **Journal of Reinforced Plastics and Composites**, Vol. 12, March 1993, pp. 341-358.
83. Vaziri, R., Olson, M.D., and Anderson, D.L., "A Plasticity-Based Constitutive Model for Fiber-Reinforced Composite Laminates," **Journal of Composite Materials**, Vol. 25, May 1991, pp. 512-535.
84. Fujita, A., Maekawa, Z., Hamada, H., and Yokoyama, A., "Mechanical Behavior and Fracture Mechanism in Flat Braided Composites. Part I: Braided Flat Bar," **Journal of Reinforced Plastics and Composites**, Vol. 11, June 1992, pp. 600-617.
85. Fujita, A., Maekawa, Z., Hamada, H., and Yokoyama, A., "Mechanical Behavior and Fracture Mechanism in Flat Braided Composites. Part II: Braided Flat Bar with a Circular Hole," **Journal of Reinforced Plastics and Composites**, Vol. 11, June 1992, pp. 618-632.
86. Jones, R.M. and Nelson, Jr., D.A.R., "A New Material Model for the Nonlinear Biaxial Behavior of ATJ-S Graphite," **Journal of Composite Materials**, January 1975, pp. 10-27.
87. Jones, R.M. and Nelson, Jr., D.A.R., "Further Characteristics of a Nonlinear Material Model for ATJ-S Graphite," **Journal of Composite Materials**, July 1975, pp. 251-265.
88. Jones, R.M. and Nelson, Jr., D.A.R., "Material Modes for Nonlinear Deformation of Graphite," **AIAA Journal**, June 1976, pp. 709-717.
89. Jones, R.M. and Nelson, Jr., D.A.R., "Theoretical-Experimental Correlation of Material Models for Nonlinear Deformation of Graphite," **AIAA Journal**, December 1976, pp. 1427-1435.
90. Jones, R.M. and Morgan, H.S., "Analysis of Nonlinear Stress-Strain Behavior of Fiber-Reinforced Composite Materials," **AIAA Journal**, December 1977, pp. 1669-1676.
91. Abu-Farsakh, G., "New Material Models for Nonlinear Stress - Strain Behavior of Composite Materials," **Composites**, July 1989, pp. 349-360.
92. Fritzson, D., "A Three-Dimensional Finite Strain Constitutive Theory for Elastomer Composites," **Computers and Structures**, Vol. 33, No. 5, 1989, pp. 1267-1287.
93. Hwang, W.C. and Sun, C.T., "Failure Analysis of Laminated Composites by Using Iterative Three-Dimensional Finite Element Method," **Computers and Structures**, Vol. 33, No. 1, 1989, pp. 41-47.
94. Gajer, G. and Dux, P., "A Damage-Sensitive Loading Algorithm for the Analysis of Reinforced Concrete Structures," **Computers and Structures**, Vol. 32, No. 2, 1989, pp. 493-496.
95. Kukreti, A.R., Khan, A.S., and Kumar, A., "A Three-Dimensional Finite Element Program to Predict Ultimate Fracture Failure Load," **Computers and Structures**, Vol. 32, No. 6, 1989, pp. 1325-1345.
96. Chang, F.-K., and Chang, K.-Y., "Post-Failure Analysis of Bolted Composite Joints in Tension or Shear-Out Mode Failure," **Journal of Composite Materials**, Vol. 21, September 1987, pp. 809-833.
97. Chang, F.-K. and Chang, K.-Y., "A Progressive Damage Model for Laminated Composites Containing Stress Concentrations," **Journal of Composite Materials**, Vol. 21, September 1987, pp. 834-855.
98. Chang, F.-K. and Kutlu, Z., "Strength and Response of Cylindrical Composite Shells Subjected to Out-of-Plane Loadings," **Journal of Composite Materials**, Vol. 23, January 1989, pp. 11-31.
99. Lee, J.D., "Three Dimensional Finite Element Analysis of Damage Accumulation in Composite Laminate," **Computers and Structures**, Vol. 15, No. 3, 1982, pp. 335-350.

100. Tsai, S.W., **Composites Design**, 3rd Ed., Think Composites, Dayton, OH, pp. 12.1-12.25.
101. Averill, R.C., **Nonlinear Analysis of Laminated Composite Shells Using a Micromechanics-Based Progressive Damage Model**, Ph.D. Thesis, Virginia Polytechnic Institute and State University, Blacksburg, VA, June 1992.
102. Averill, R.C., "A Micromechanics-Based Progressive Failure Model for Laminated Composite Structures," **33rd AIAA/ASME/ASCE/AHS/ACS Structures, Structural Dynamics, and Materials Conference**, 1992, pp. 2898-2904.
103. Pandey, A.J., **A Nonlinear Computational Model for the Strength and Failure of Composite Plates and Shells**, Ph.D. Thesis, Virginia Polytechnic Institute and State University, Blacksburg, VA, June 1987.
104. Reddy, Y.S.N. and Reddy, J.N., "Linear and Nonlinear Failure Analysis of Composite Laminates with Transverse Shear," **Composites Science and Technology**, Vol. 44, 1991, pp. 227-255.
105. Pierce, F.T., "The Geometry of Cloth Structures," **Journal of the Textile Institute**, Vol. 28, pp. T45-T96.
106. Tiller, A.W., "Rational B-Splines for Curve and Surface Representation," **IEEE Computer Graphics and Applications**, Vol. 3, No. 6, 1983, pp. 61-69.
107. Cook, R.D., Malkus, D.S., and Plesha, M.E., **Concepts and Applications of Finite Element Analysis**, 3rd Ed., John Wiley and Sons, New York, 1989.
108. Burr, S.T., Master of Science Thesis, Michigan Technological University, 1991.
109. Kriz, R.D., Glaessgen, E.H., and MacRae, J.D., "Visualizing Gradients in Composite Design and Fabrication," **IEEE Computer Graphics and Applications**, Vol. 15, No. 6, pp. 10-13, 1995.
110. Timoshenko, S.P., **History of Strength of Materials**, Dover Publications, New York, 1983.
111. Faupel, J.H. and Fisher, F.E., **Engineering Design**, Wiley-Interscience, New York, 1981.
112. Mendelson, A., **Plasticity: Theory and Application**, R.E. Krieger Publishing Company, Malabar, FL, 1968.
113. Lempriere, B.M., "Poisson's Ratio in Orthotropic Materials", **AIAA Journal**, November 1968, pp. 2226-2227.
114. Dougill, J.W., "On Stable Progressively Fracturing Solids," **Journal of Applied Mathematics and Physics**, Vol. 27, pp. 423-436.
115. Authors unknown, **ABAQUS/Standard User's Manual**, Hibbit, Karlsson and Sorenson, Pawtucket, RI, 1994.
116. Authors unknown, **ABAQUS/Theory Manual**, Hibbit, Karlsson and Sorenson, Pawtucket, RI, 1994.
117. Authors unknown, Writing a (V)UMAT, presentation at the **1993 ABAQUS Users' Conference**, Aachen, Germany, June 23-25, 1993.
118. Zienkiewicz, O.C. and Taylor, R.L., **The Finite Element Method**, 4th Ed., McGraw-Hill, London, 1991.
119. Reddy, J.N., **An Introduction to the Finite Element Method**, McGraw-Hill, New York, 1984.
120. Broek, D., **Elementary Engineering Fracture Mechanics**, 4th Ed., Martinus Nijhoff Publishers, 1987.

Appendix A: Glossary of Terms for Textiles

12-HS[†]. 12-harness satin weave characterized by long yarn floats.

12-HSTS[†]. 12-harness satin weave with through-thickness stitching.

Angle Interlock[†]. Three-dimensional woven fabric manufactured using the multiwarp weaving method having a 0°/90° planar fiber orientation and angular through-thickness orientation.

Bias Yarns. Yarns aligned in any direction other than the warp or weft directions.

Biaxial Woven Fabrics[†]. Fabrics with interlaced yarns oriented along 0°/90° axes.

Braiding[†]. A fabric-formation process that intertwines three or more yarns in the bias direction.

Bundle Efficiency[†]. The fractional translation of a given fiber's properties to the yarn bundle.

Discrete Fibers[†]. Short, discontinuous fiber, staple fibers, and fibers of discontinuous length.

Fabric[†]. Any nonwoven, woven, knitted, or braided fibrous structure or three-dimensional fibrous assembly.

Fiber-to-Fabric Structure[†]. A fibrous structure manufactured directly from fibers into a fabric.

Fill (Weft) Yarns^{*}. Yarns that are shuttled transversely across the loom.

Folded^{*}. Cloth laminae that are laminated with normals in the opposite direction.

Harness^{*}. The number of warp yarns per fill wavelength.

Jamming Point. The state whereby yarns in a braided material are packed as tightly as possible.

Multiaxial Warp Knit (MWK)[†]. Warp-knitted fabric with 0°/90°/±θ oriented yarns assembled with stitching yarns oriented in the through-thickness direction.

Orthogonal Woven Fabric[†]. A three-directional fabric manufactured by mutual fiber placement in three or more orthogonal directions with no interlacing.

Plain Weave[†]. Woven fabric characterized by the repeating interlacing of two warp (0°) and two filling (90°)

pick yarns. Has the highest density of interlacing of all woven fabrics.

Preform[†]. The fibrous structure of a composite before matrix introduction.

Quadraxial Fabric[†]. Fabric with yarn orientation along the $0^\circ/90^\circ/\pm\theta$ axes.

Representative Volume Element. Smallest repeating unit of a textile composite.

Satin Weave[†]. Woven fabric characterized by long yarn floats between interlacings.

Stacked^{*}. Cloth laminae that are laminated with both normals in the same direction.

Textile[†]. Pertaining to the manufacture of yarns, cloth, and cloth products.

Three-Dimensional Braiding[†]. Yarn-position displacement method for creating a net-shape structure with a three-dimensional network of fibers capable of four or more directions of yarn orientation (also called track and column, Through-Thickness®, and Euclidean braiding).

Translation Efficiency[†]. The fraction of fiber properties translated into the fibrous structure.

Twill Weave[†]. Woven fabric characterized by yarn interlacing in a staggered fashion; yarn interlacing density lies between plain and satin weave.

Two-Step Braiding[†]. A three-dimensional braiding method characterized by substantial amounts of 0° fiber orientation integrated into a network of through-thickness fibers.

Uniaxial Fabric[†]. Fabric with yarn orientation primarily along the 0° axis.

Unit Cell. see representative volume element.

Warp Knit[†]. Knitted structure in which the loops are formed by the multiple introduction of yarns along the machine (0°) direction.

Warp Yarns^{*}. Yarns that are laid out longitudinally on the loom.

Weaving[†]. A fabric-formation process using the interlacing of yarns.

Weft Knit[†]. Knitted structure in which the loops are formed by introducing yarns in the horizontal (90°) direction.

Weft Yarns. Yarns that are laid out transversely on the loom.

Yarn Linear Density[†]. A measure of fineness of fiber and yarns. Measured in denier (g/900 m) or tex (g/1000 m).

Yarn[†]. Linear fibrous assembly consisting of multiple filaments.

* Yurgartis, S.W., and J.P. Maurer, "Modelling weave and stacking configuration effects on interlaminar shear stresses in fabric laminates," *Composites*, Vol. 24, No. 8, 1993, pp. 651-658.

† Ko, F.K., "Preform Fiber Architecture for Ceramic-Matrix Composites," *Ceramic Bulletin*, Vol. 68, No. 2, 1989, pp. 401-413.

Appendix B: Figures from Chapter 4

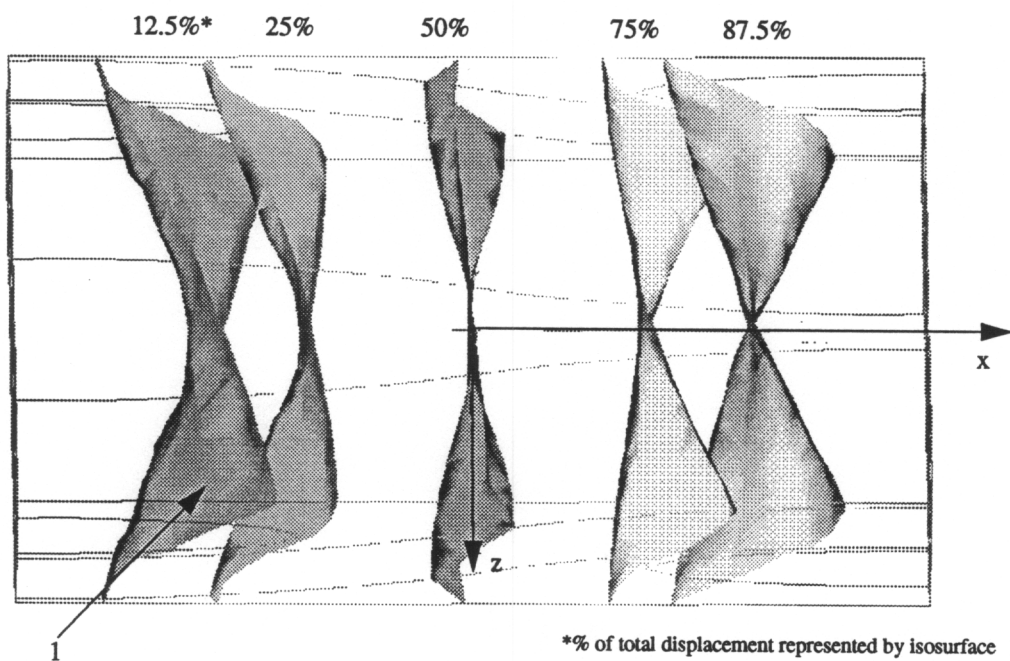


Figure 4.1.1.1a. Axial displacement, U_x . Periodic boundary conditions. $U_{x, \max} = 8.89\text{E-}7$ in/F.

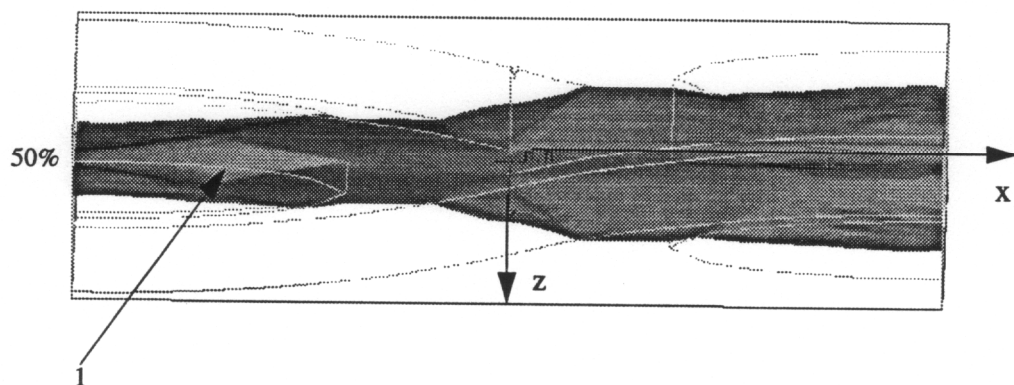


Figure 4.1.1.1b. Out-of-plane displacement, U_y . Periodic boundary conditions. $U_{y, \max} = 1.63E-6$ in/F.

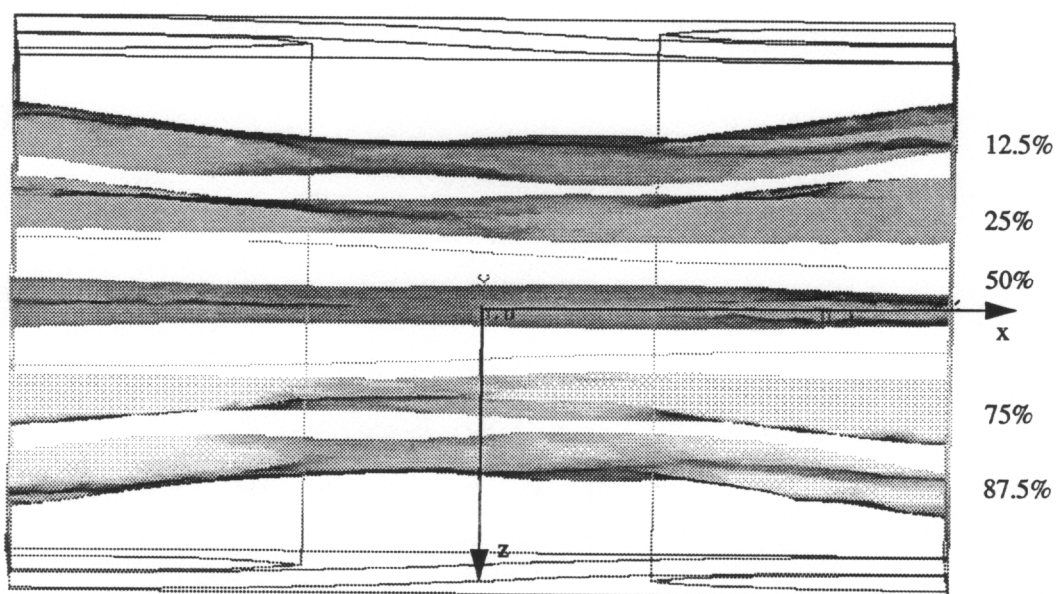


Figure 4.1.1.1c. Transverse displacement, U_z . Periodic boundary conditions. $U_{z, \max} = 9.19\text{E-}7$ in/F.

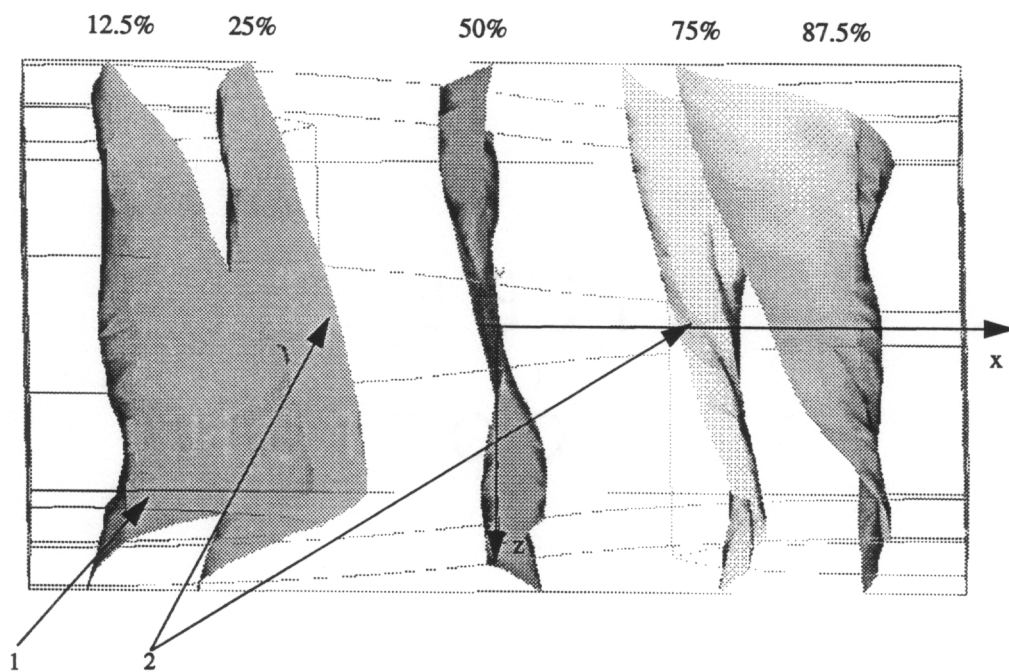


Figure 4.1.1.2a. Axial displacement, U_x . Free top surface. $U_{x, \max} = 9.08\text{E-}7$ in/F.

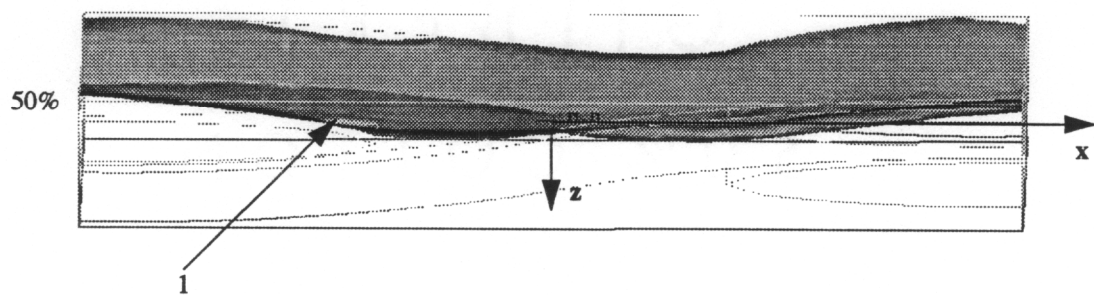


Figure 4.1.1.2b. Out-of-plane displacement, U_y . Free top surface. $U_{y, \max} = 2.12\text{E-}6 \text{ in/F}$.

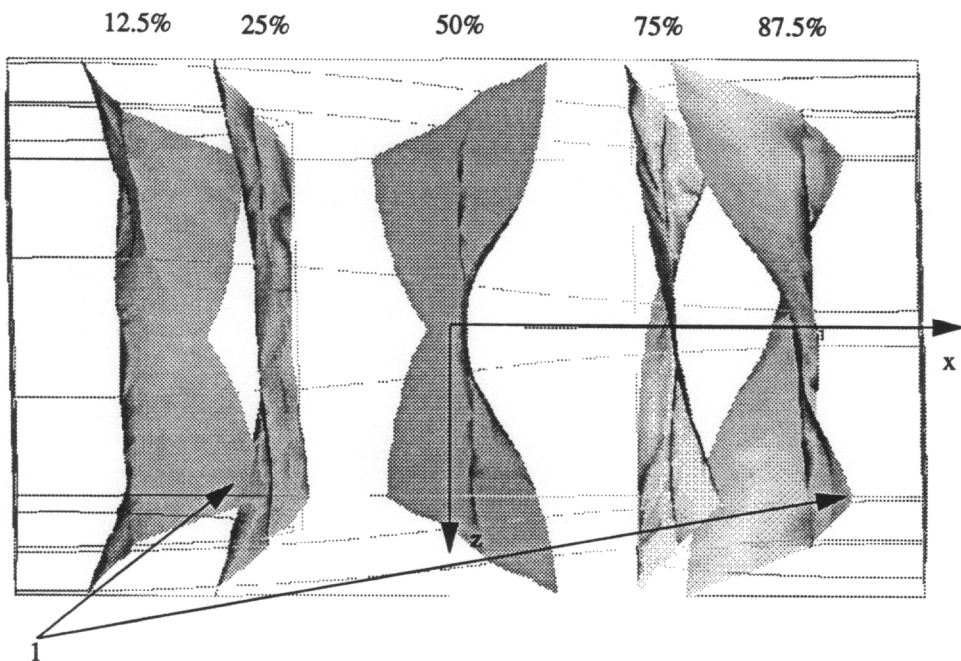


Figure 4.1.1.2c. Axial displacement, U_x . Free top/bottom surface. $U_{x,max} = 9.92E-7$ in/F.

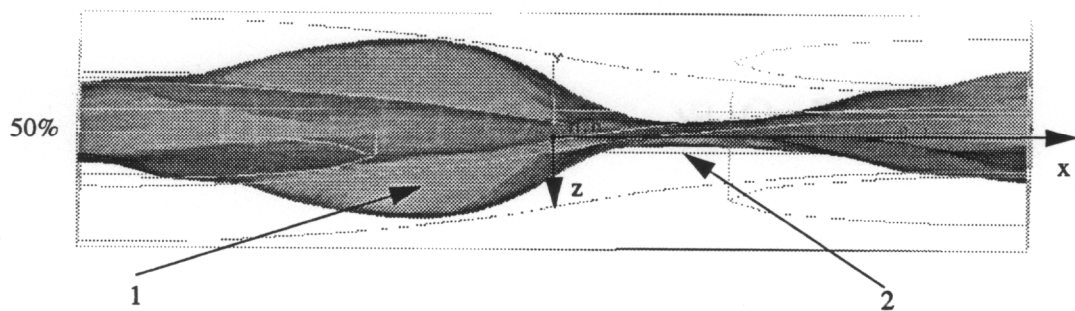


Figure 4.1.1.2d. Out-of-plane displacement, U_y . Free top/bottom surface. $U_{y, \max} = 2.39\text{E-}6$ in/F.

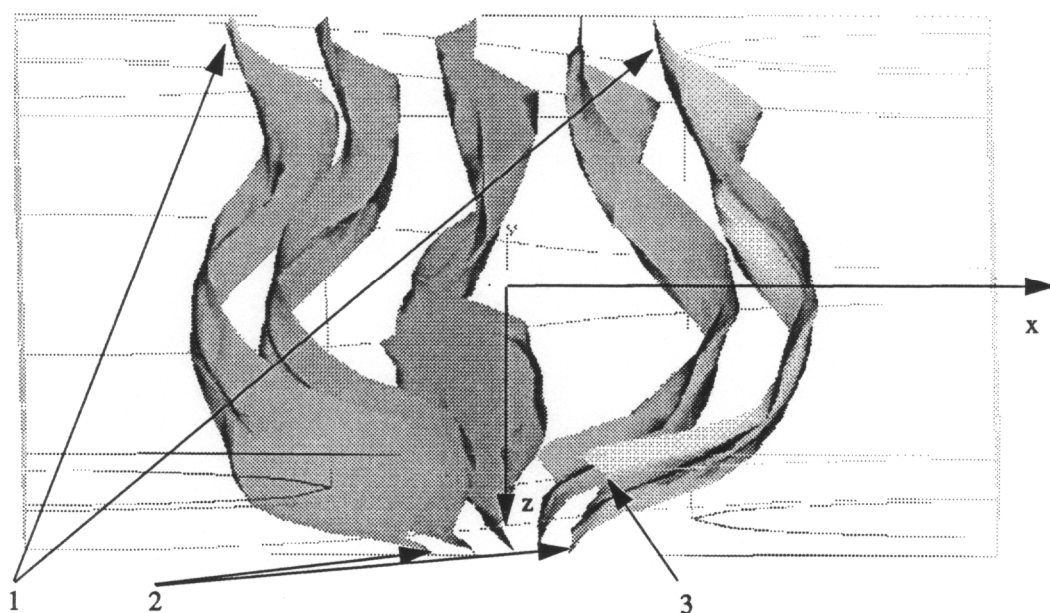


Figure 4.1.1.3a. Axial displacement, U_x . Free front surface. $U_{x, \max} = 1.15E-6$ in/F.

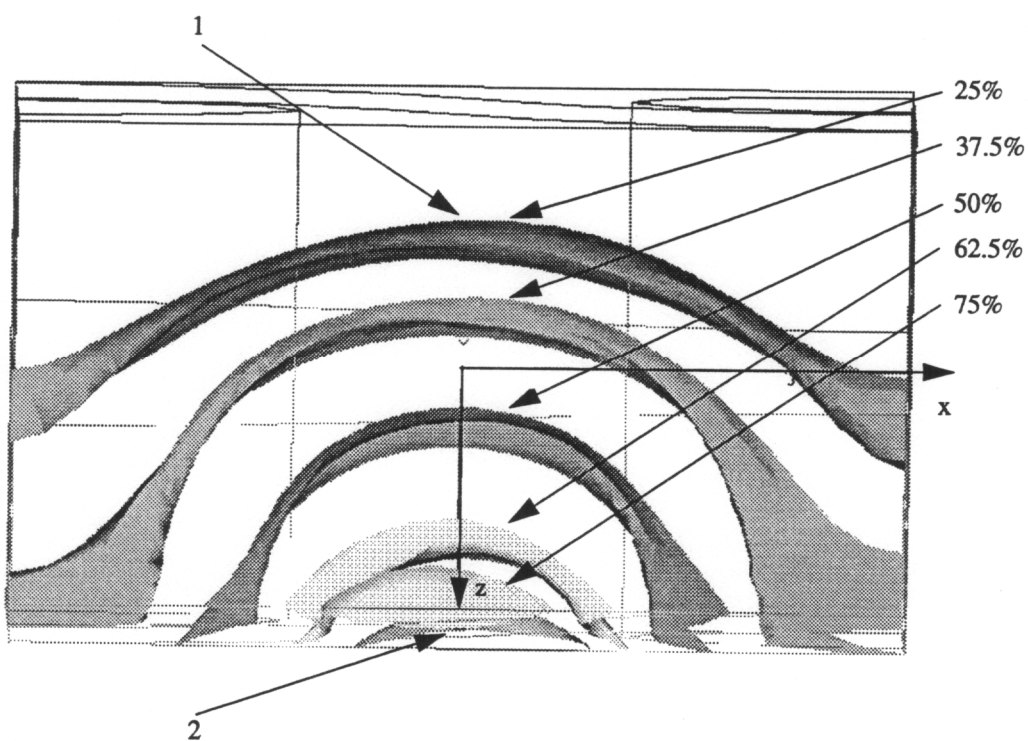


Figure 4.1.1.3b. Transverse displacement, U_z . Free front surface. $U_{z, \max} = 3.16\text{E-}6$ in/F.

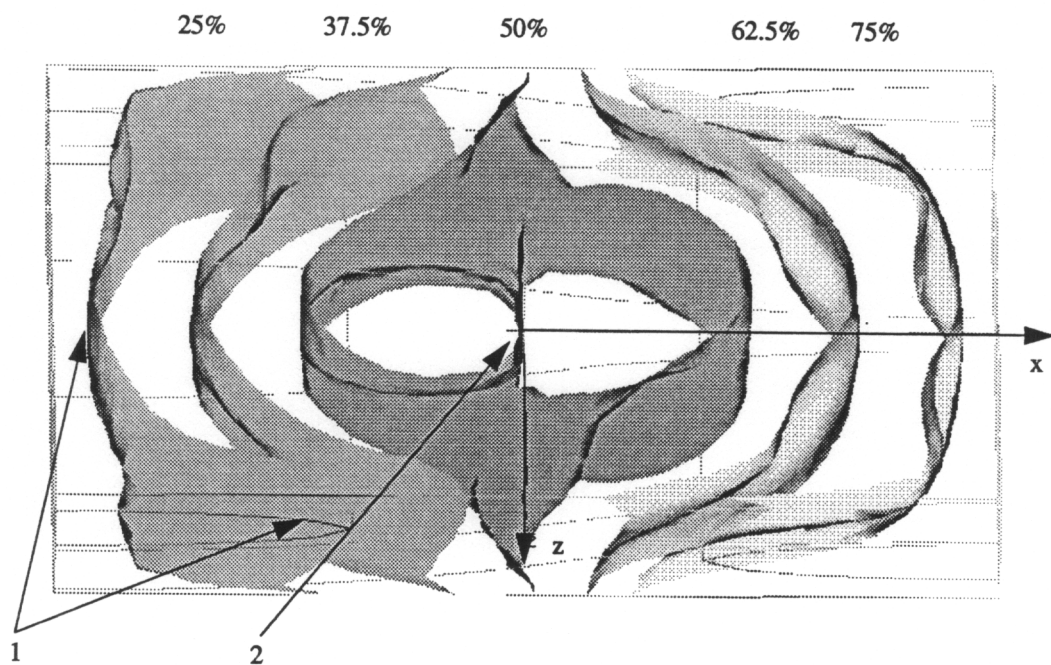


Figure 4.1.1.3c. Axial displacement, U_x . Free front/back surface. $U_{x, \max} = 1.02E-6$ in/F.

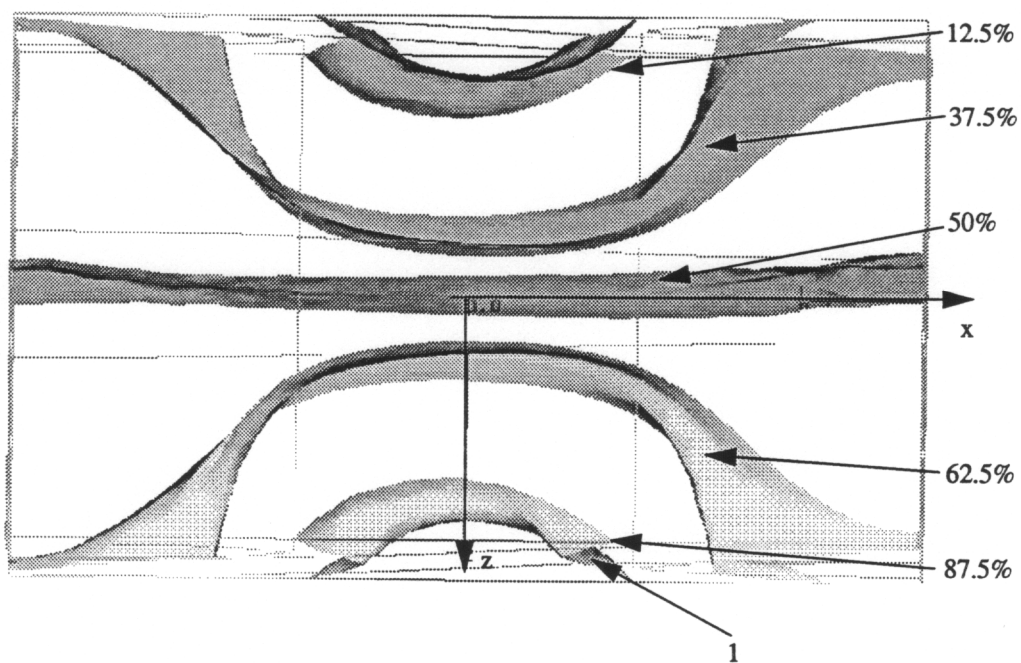


Figure 4.1.1.3d. Transverse displacement, U_z . Free front/back surface. $U_{z, \max} = 4.73\text{E-}6 \text{ in/F}$.

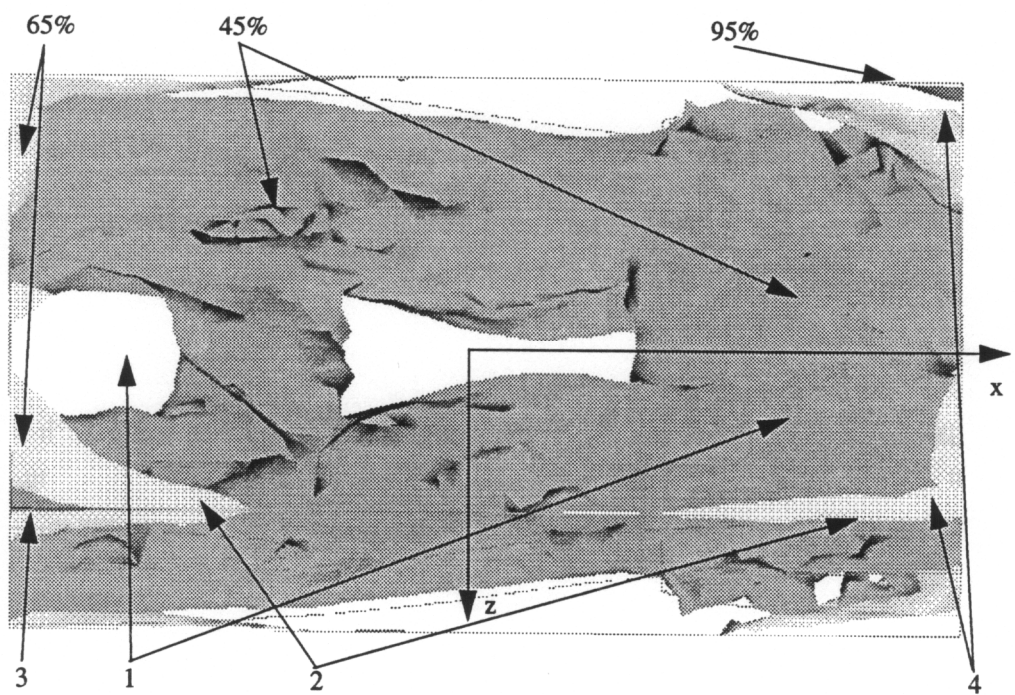


Figure 4.1.2a. Strain energy density, SED. Periodic boundary conditions. $0.546\text{E-}4 < \text{SED} < 6.68\text{E-}4$ (in-lb/in³)/F.

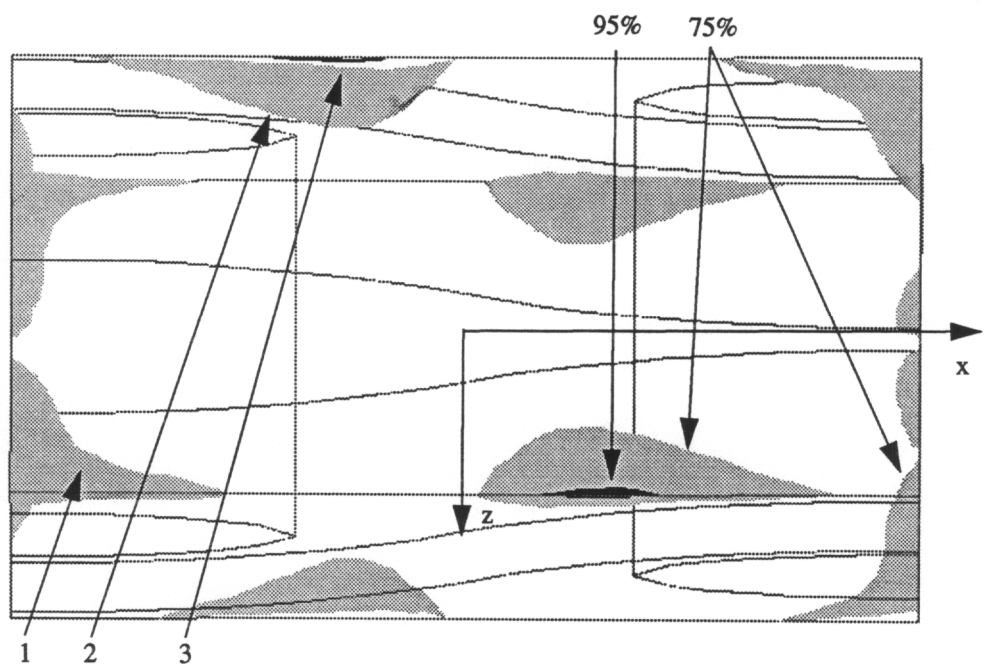


Figure 4.1.2b. Strain energy density, SED. Free top/bottom surface. $0.532\text{E-}4 < \text{SED} < 5.06\text{E-}4$ (in-lb/in³)/F.

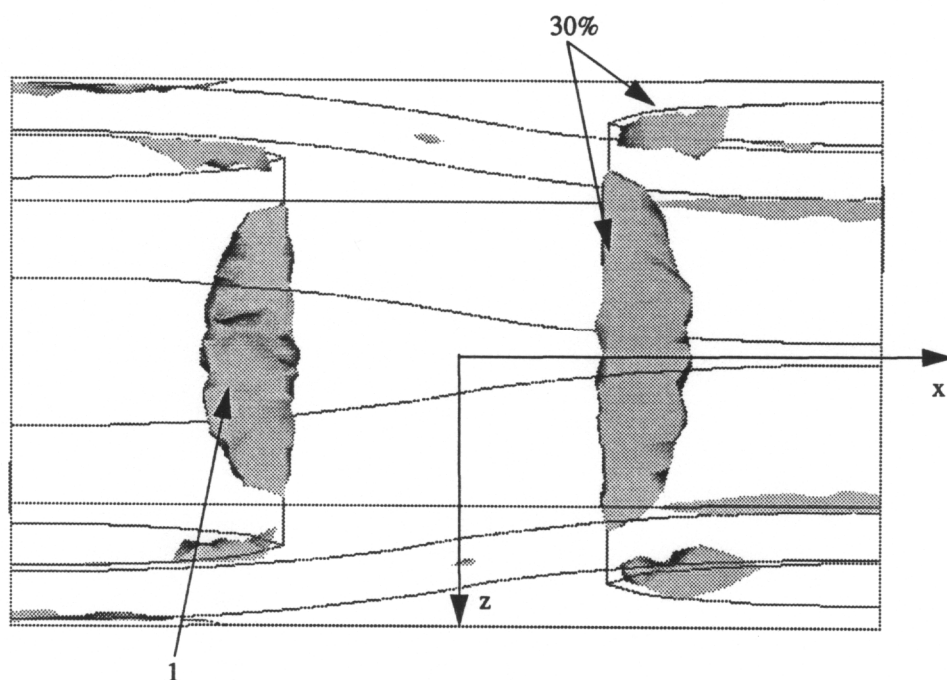


Figure 4.1.2c. Strain energy density, SED. Free front/back surface. $0.248E-4 < SED < 17.90E-4$ (in-lb/in³)/F.

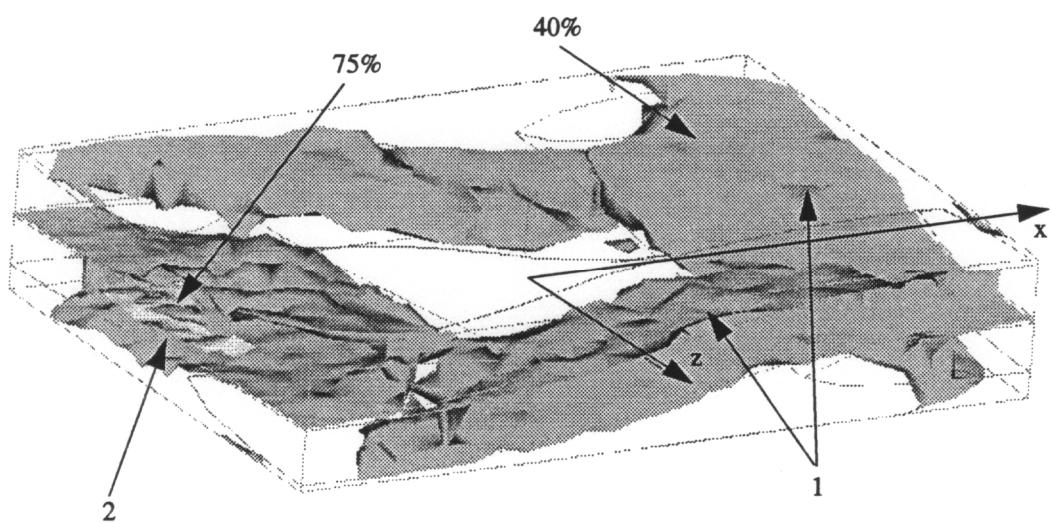


Figure 4.1.2d. Strain energy density, SED. Periodic boundary conditions. Glass/epoxy yarns.
 $0.281\text{E-}4 < \text{SED} < 4.08\text{E-}4$ (in-lb/in³)/F.

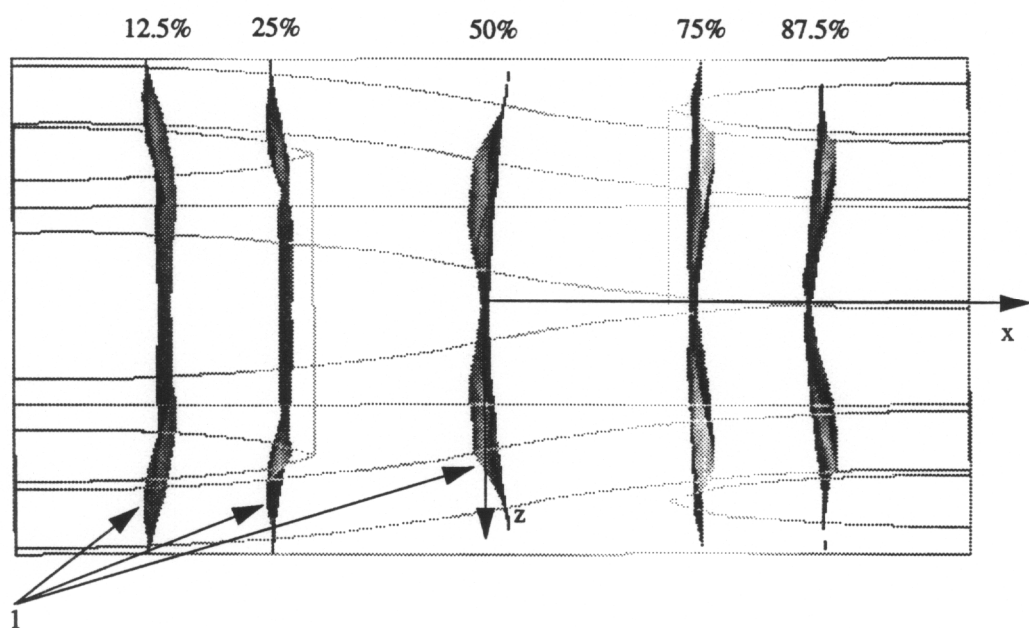


Figure 4.2.1.1a. Axial displacement, U_x . Periodic boundary conditions. $U_{x, \max} = 0.00275$ in.

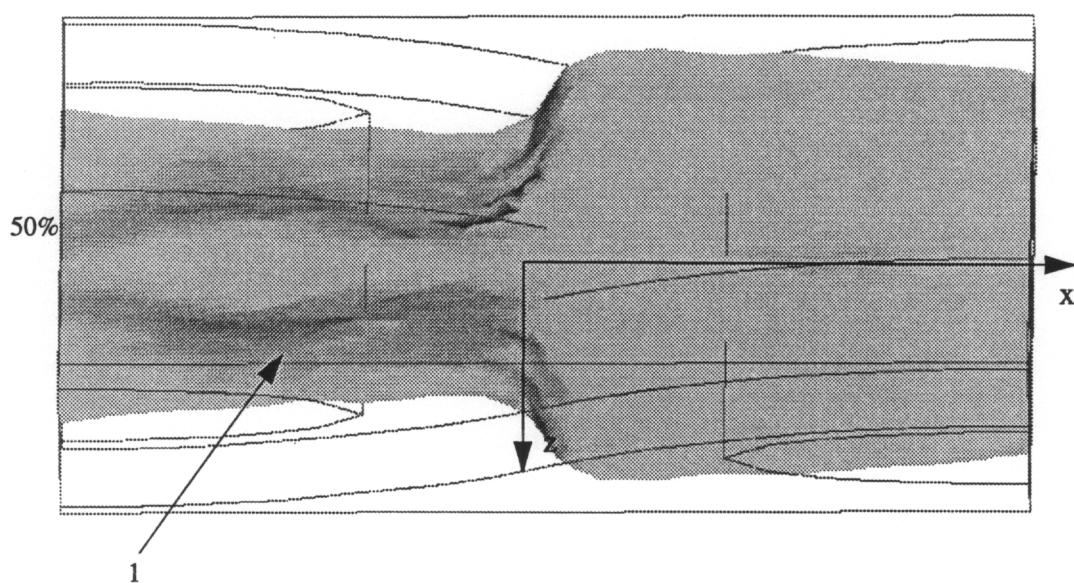


Figure 4.2.1.1b. Out-of-plane displacement, U_y . Periodic boundary conditions. $U_{y, \max} = -2.56E-5$ in.

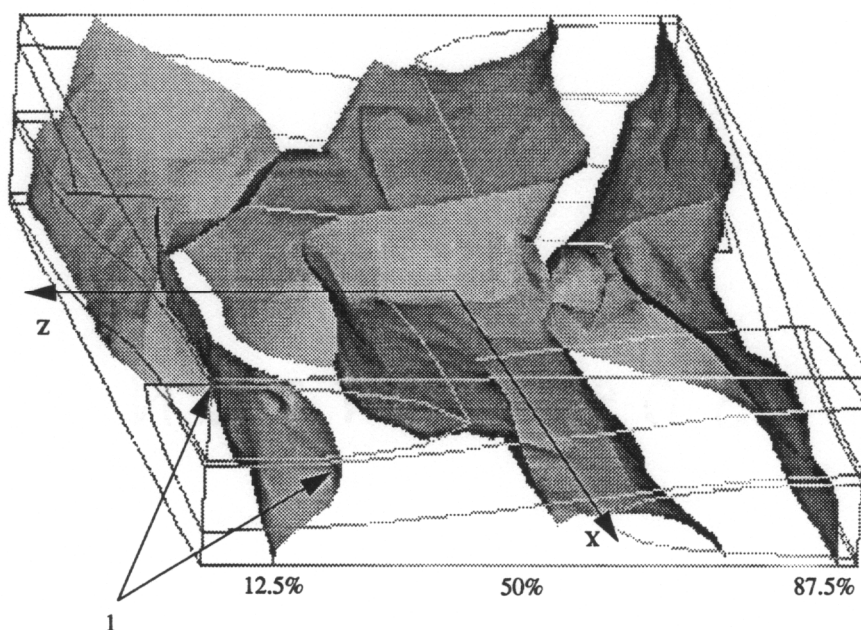


Figure 4.2.1.1c. Transverse displacement, U_z . Periodic boundary conditions. $U_{z, \max} = -1.31\text{E-}5$ in.

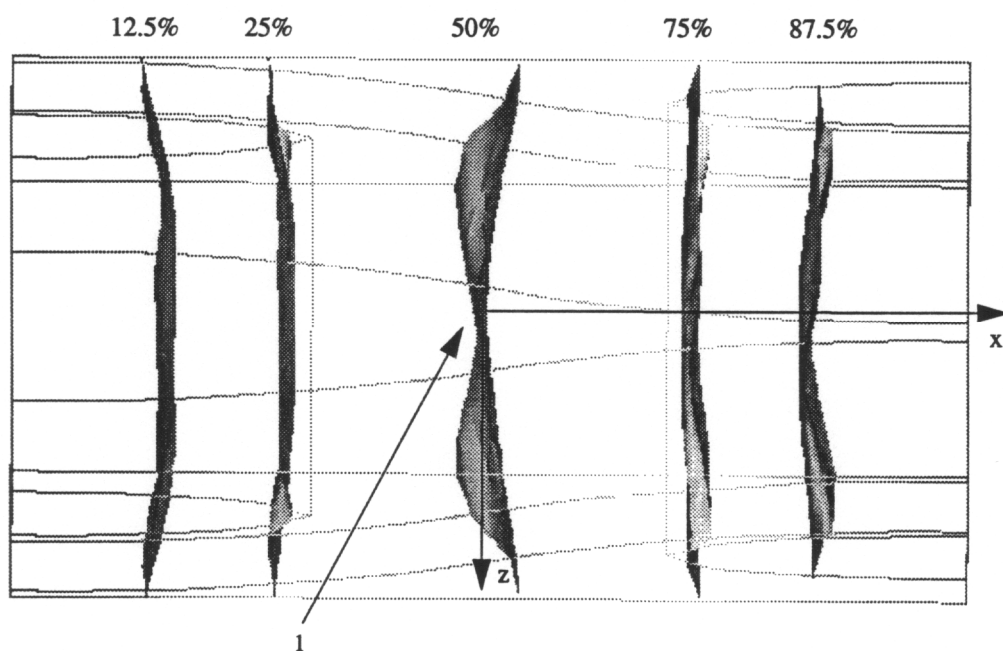


Figure 4.2.1.2a. Axial displacement, U_x . Free top surface. $U_{x, \max} = 0.00275$.

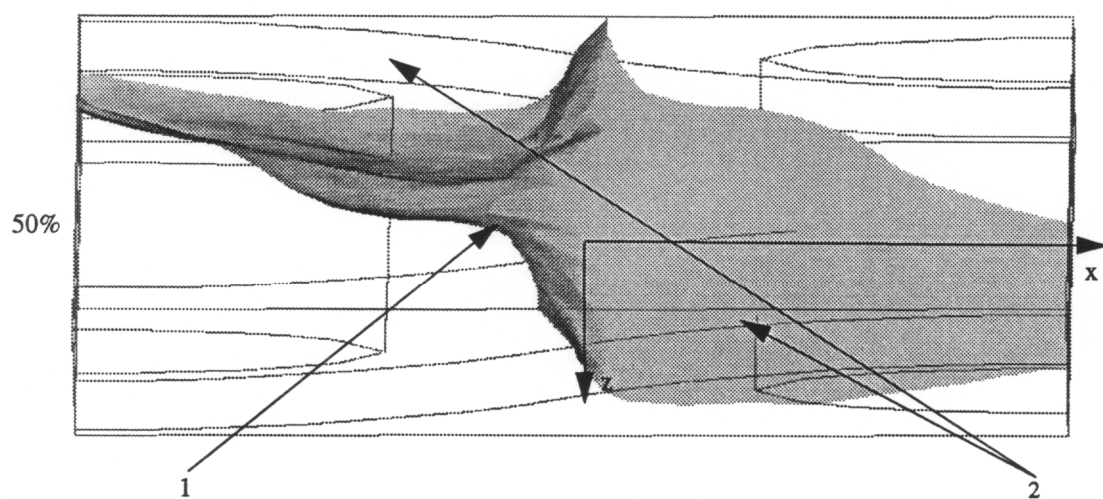


Figure 4.2.1.2b. Out-of-plane displacement, U_y . Free top surface. $U_{y, \max} = -4.33\text{E-}5$ in.

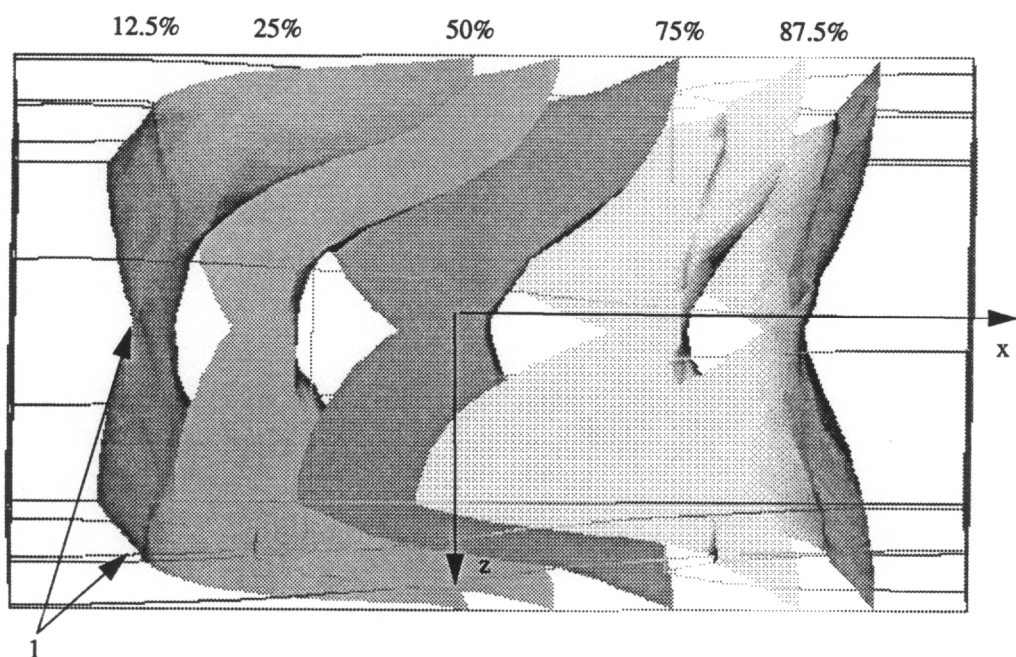


Figure 4.2.1.2c. Axial displacement, U_x . Free top/bottom surface. $U_{x, \max} = 0.00275$ in.

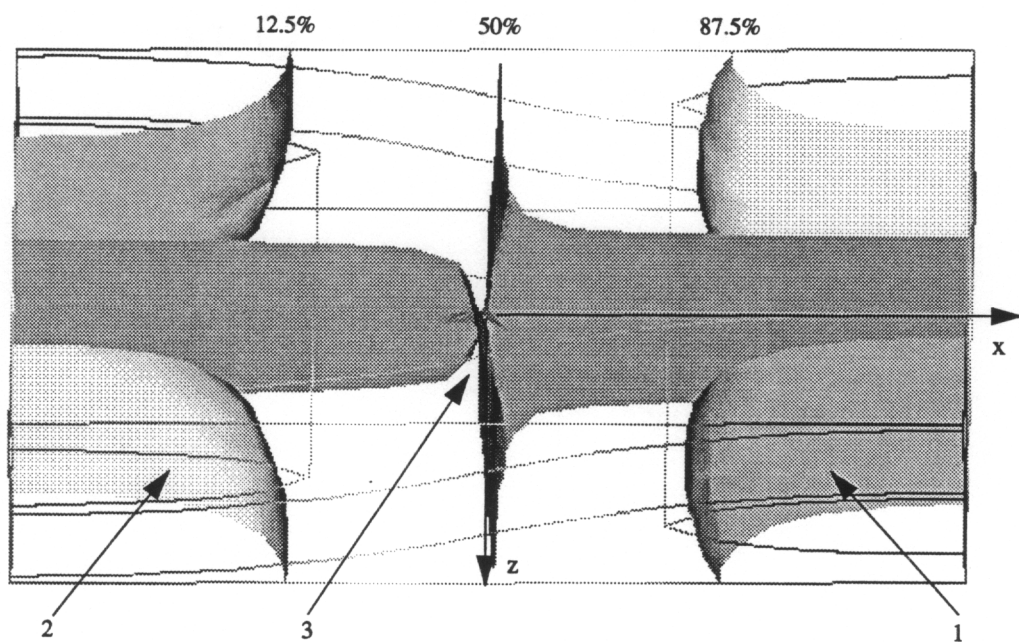


Figure 4.2.1.2d. Out-of-plane displacement, U_y . Free top/bottom surface. $U_{y, \max} = -61.2\text{E-}5$ in.

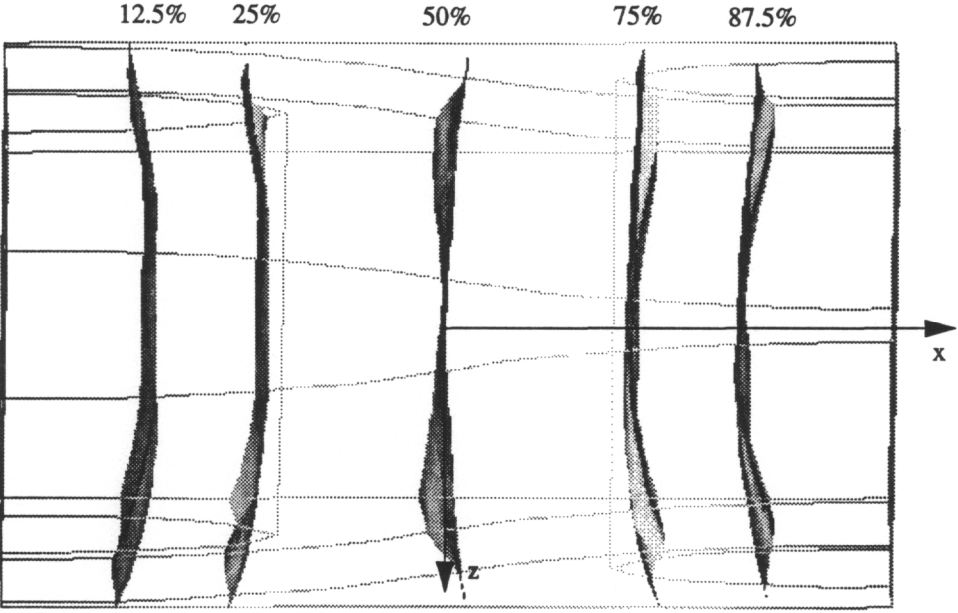


Figure 4.2.1.3a. Axial displacement, U_x . Free front surface. $U_{x, \max} = 0.00275$ in.

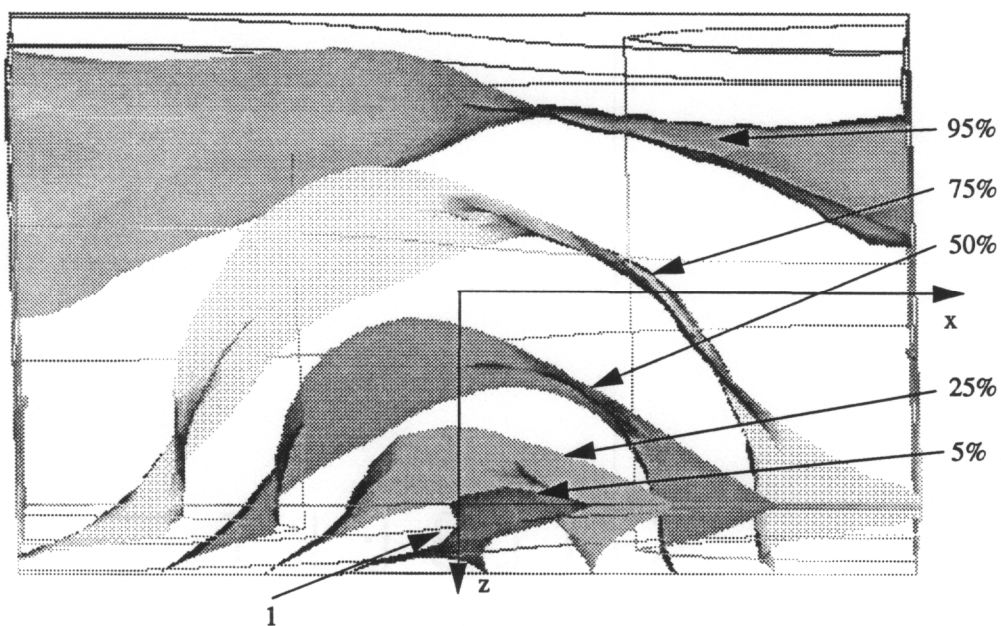


Figure 4.2.1.3b. Transverse displacement, U_z . Free front surface. $U_{z, \max} = -4.40\text{E-}5$ in.

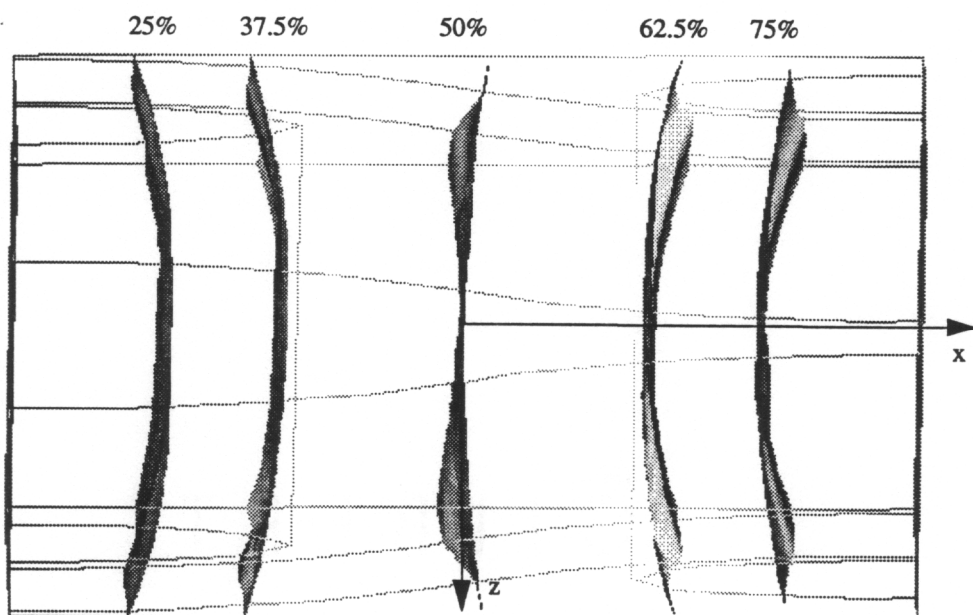


Figure 4.2.1.3c. Axial displacement, U_x . Free front/back surface. $U_{x, \max} = 0.00275$ in.

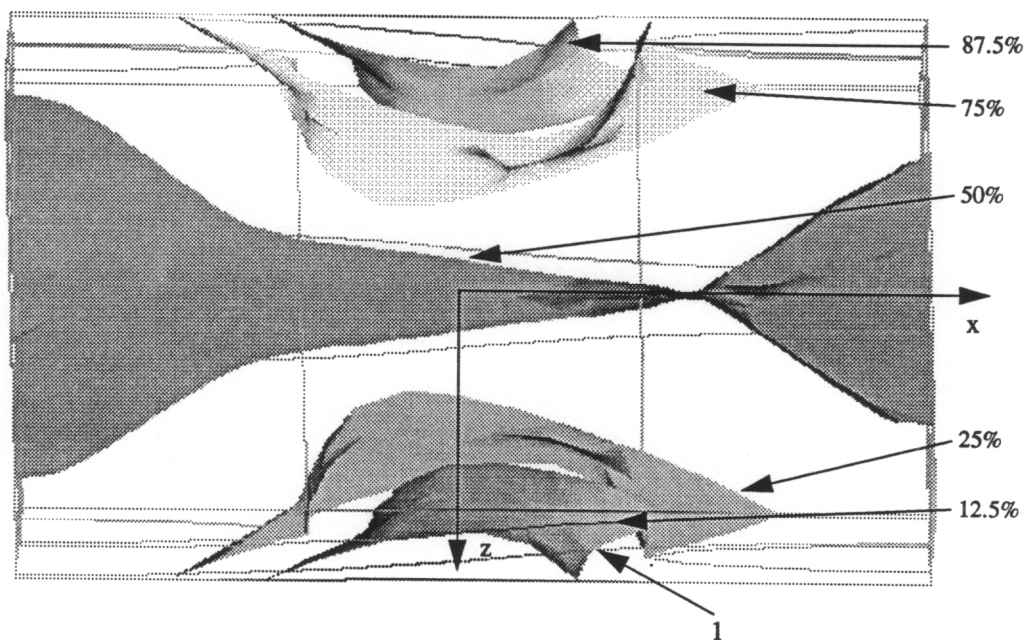


Figure 4.2.1.3d. Transverse displacement, U_z . Free front/back surface. $U_{z, \max} = -6.60E-5$ in.

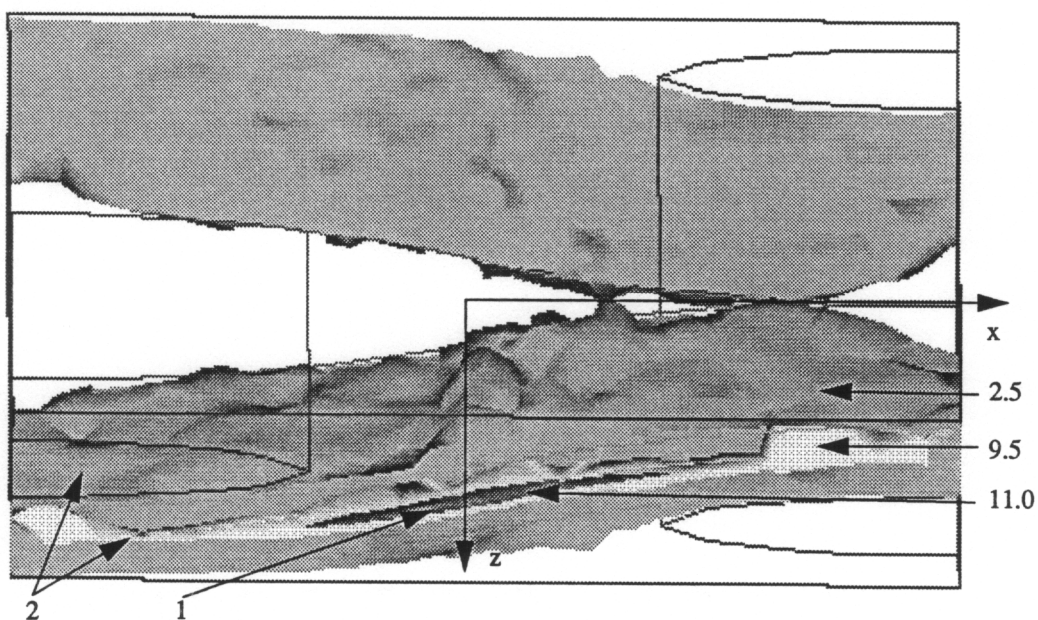


Figure 4.2.2a. Strain energy density, SED. Periodic boundary conditions. $0.0035 < \text{SED} < 11.2 \text{ in-lb/in}^3$.

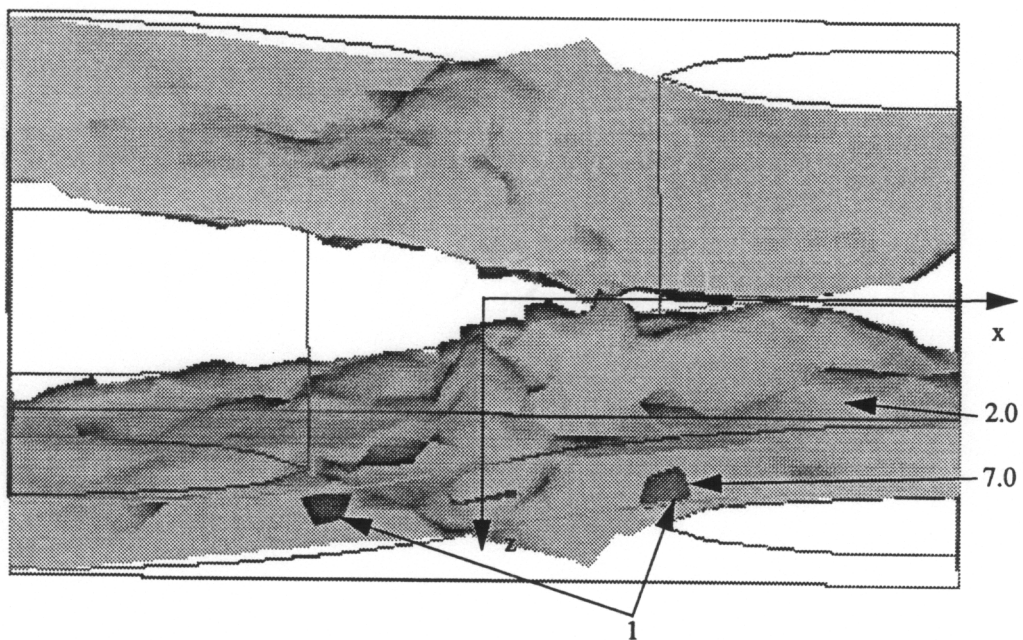


Figure 4.2.2b. Strain energy density, SED. Free top/bottom surface. $0.0545 < SED < 7.2$ in-lb/in³.

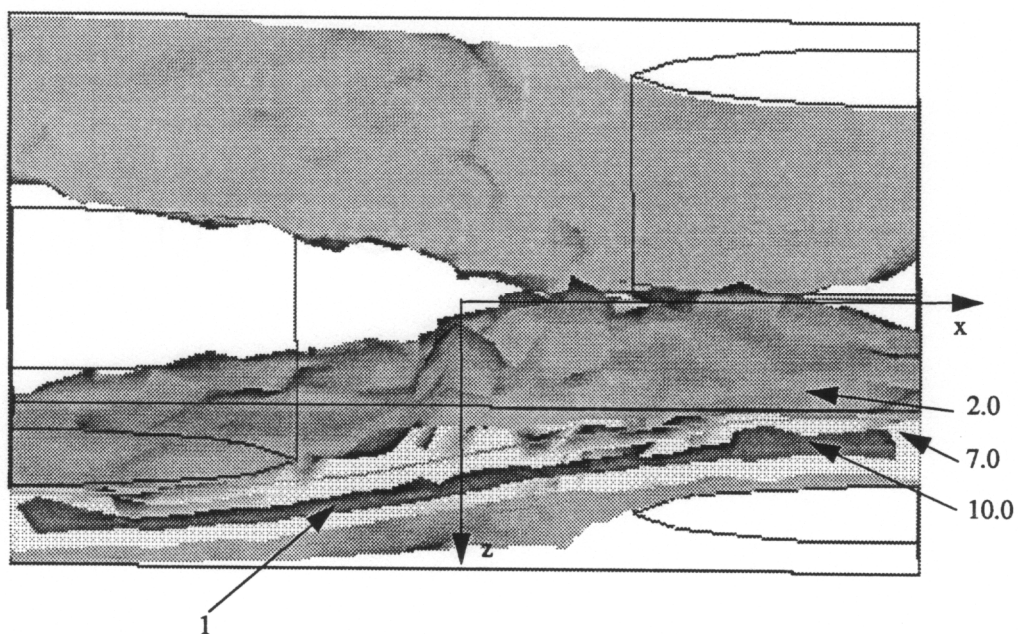


Figure 4.2.2c. Strain energy density, SED. Free front/back surface. $0.0638 < SED < 10.6 \text{ in-lb/in}^3$.

Appendix C: Figures from Chapter 6

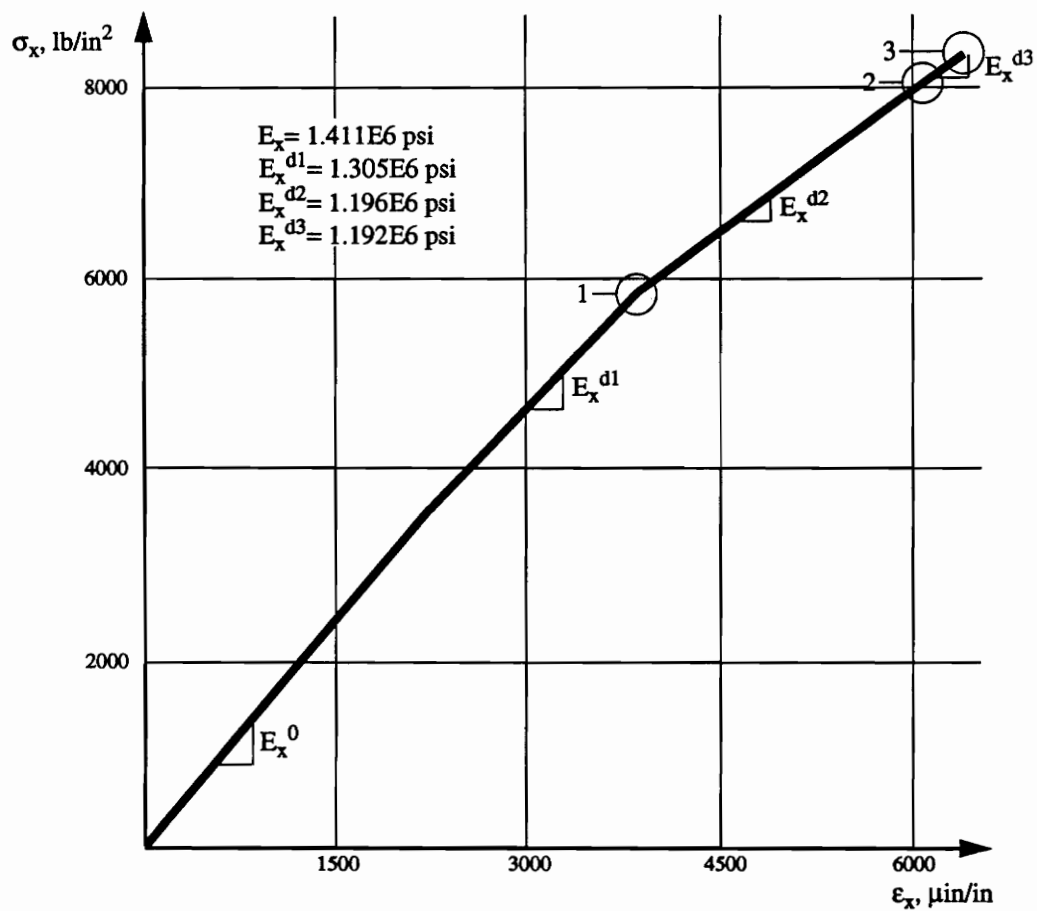


Figure 6.2.1a. Axial response of a glass/epoxy material with periodic boundary conditions.

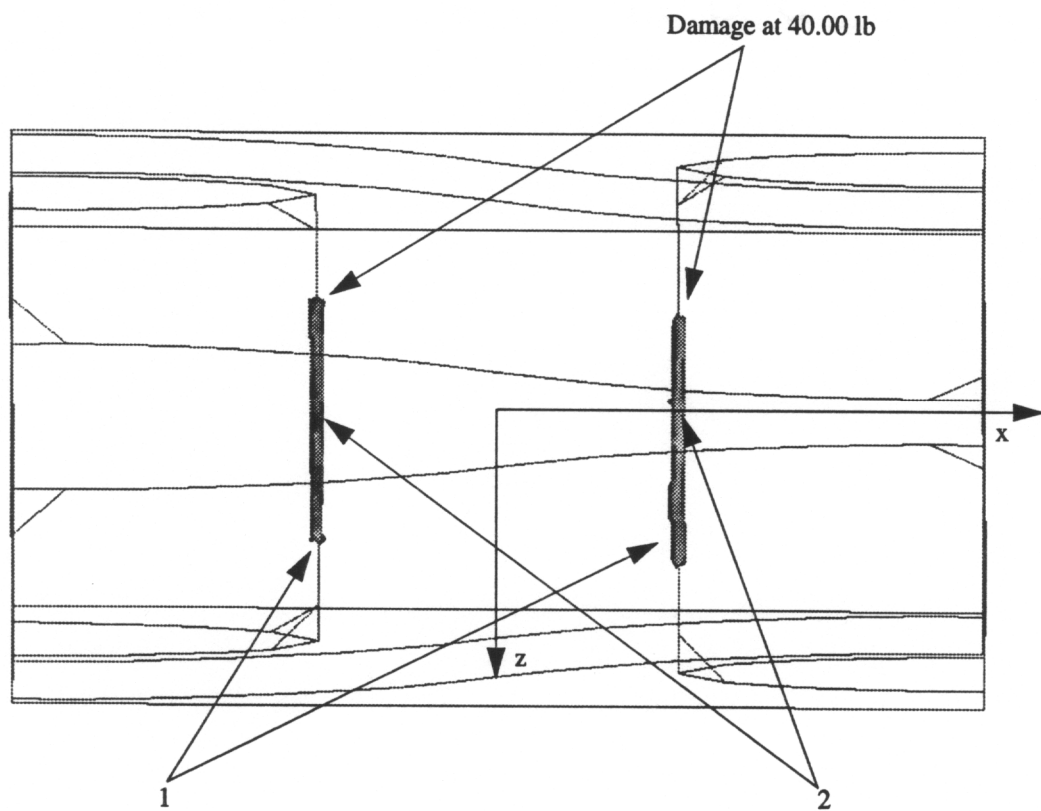


Figure 6.2.1b. Onset of tensile matrix mode damage in a glass/epoxy material with periodic boundary conditions.

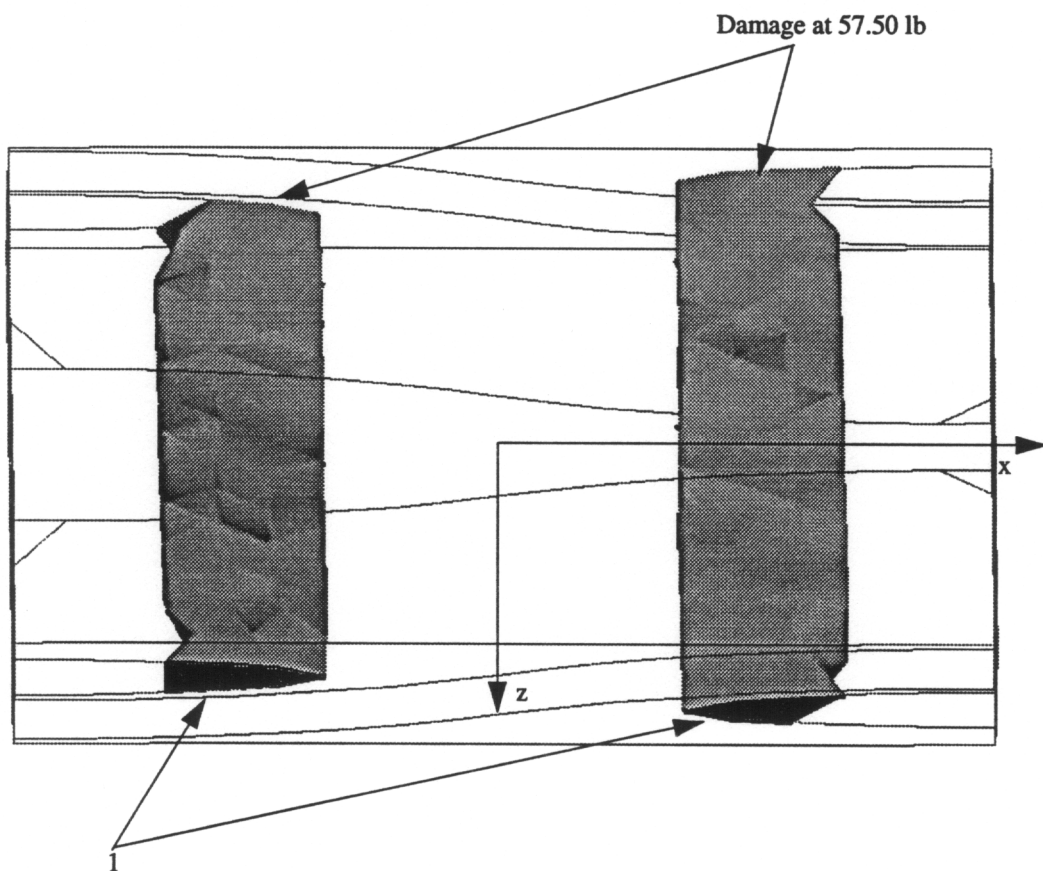


Figure 6.2.1c. Progression-1 of tensile matrix mode damage in a glass/epoxy material with periodic boundary conditions.

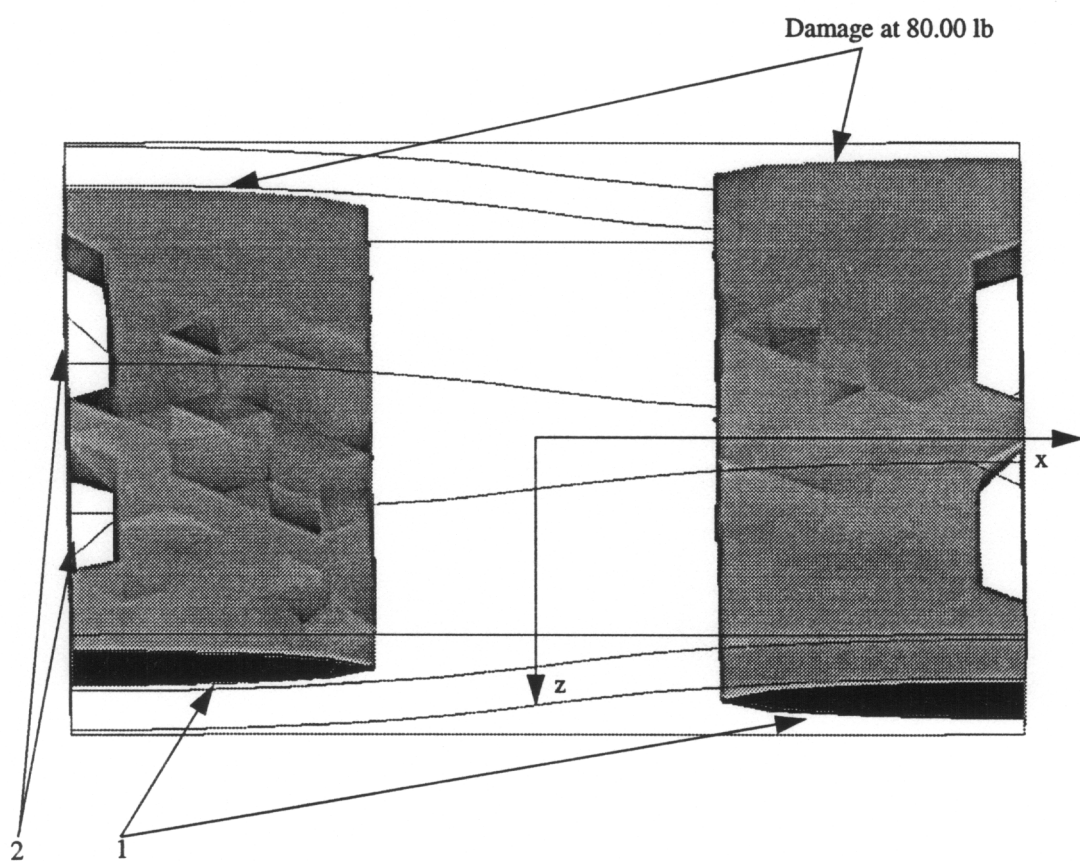


Figure 6.2.1d. Progression-2 of tensile matrix mode damage in a glass/epoxy material with periodic boundary conditions.

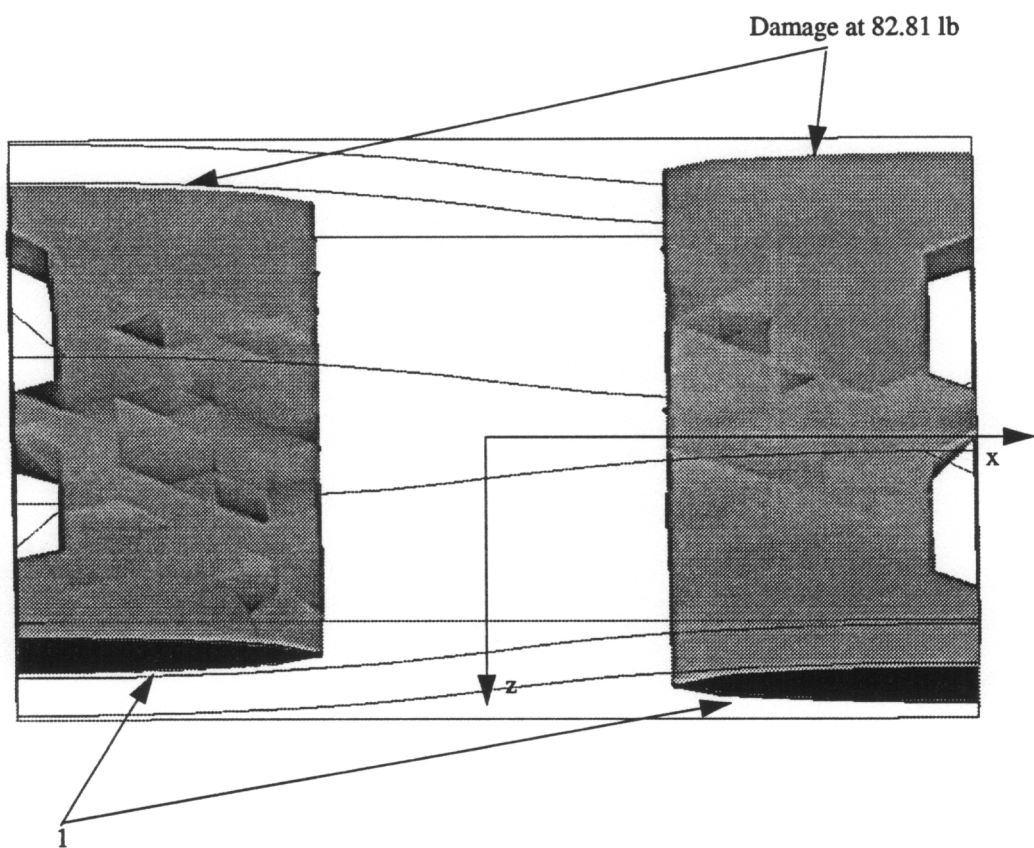
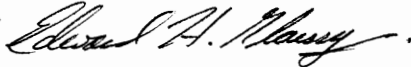


Figure 6.2.1c. Progression-3 of tensile matrix mode damage in a glass/epoxy material with periodic boundary conditions.

Vita

Edward H. Glaessgen was born 15 November 1967 in Brooklyn, New York to Edward J. and Judith L. Glaessgen and was raised in Brooklyn, New York; Dallas, Texas; and Tulsa, Oklahoma. He received his Bachelor of Science and Master of Science degrees in Mechanical Engineering from the University of Tulsa in May 1989 and August 1991, respectively. During his tenure as a Master of Science candidate he was employed as a Member of Technical Staff for Rockwell International's North American Aircraft Operations Division in Tulsa. After completion of his Ph.D. degree in June 1996, he will take a position as a National Research Council Post Doctoral Fellow in the Mechanics of Materials Branch of the NASA-Langley Research Center.

A handwritten signature in black ink, appearing to read "Edward H. Glaessgen", followed by a period.